Annual Report for the LIBRA Light Ion Beam Fusion Reactor Project for the Period January – December 1983

B. Badger, T. Bartel, J. Billen, M.L. Corradini, R. Engelstad, D. Henderson, G.L. Kulcinski, G.A. Moses, K. O'Brien, R.R. Peterson, L. Pong, M.E. Sawan, I.N. Sviatoslavsky, D.K. Sze, W.F. Vogelsang, J.J. Watrous

December 1983

FPA-83-8

FUSION POWER ASSOCIATES

2 Professional Drive, Suite 248
Gaithersburg, Maryland 20879
(301) 258-0545

1500 Engineering Drive
Madison, Wisconsin 53706
(608) 263-2308

ANNUAL REPORT FOR THE
LIBRA LIGHT ION BEAM FUSION REACTOR PROJECT
FOR THE PERIOD JANUARY - DECEMBER 1983

B. Badger
J. Billen
T. Bartel
M.L. Corradini
R. Engelstad
D. Henderson
G.L. Kulcinski
E.G. Lovell
G.A. Moses
K. O'Brien
R.R. Peterson
L. Pong
M.E. Sawan
I.N. Sviatoslavsky
D.K. Sze
W.F. Vogelsang
J.J. Watrous

December 1983

FPA-83-8

TABLE OF CONTENTS

		Page
1.	INTRODUCTION	1-1
2.	INPORT UNIT STRUCTURAL ANALYSIS	2.2-1
	2.1 Introduction	2.2-1
	2.2 Progress in Fatigue Testing of Silicon Carbide Fiber	2.2-1
	2.3 Dynamic Response of First Wall INPORT Units	2.3-1
3.	CAVITY GAS DYNAMICS AND HEAT TRANSFER	3.1-1
	3.1 Introduction	3.1-1
	3.2 Fireball Analysis	3.2-1
	3.3 Heat and Mass Transfer in INPORT Tubes	3.3-1
	3.3.1 Phase I	3.3-4
	3.3.2 Phase II	3.3-6
	3.3.2.1 Pulse Shape	3.3-6
	3.3.2.2 Fluid Characteristics	3.3-7
	3.3.2.3 Pulse-Body Interaction	3.3-8
	3.3.2.4 Stagnation Heat Flux	3.3-9
	3.3.2.5 Interference	3.3-9
	3.3.2.6 Model	3.3-10
	3.3.2.7 Model Results	3.3-12
	3.3.3 Phase III	3.3-15
	3.3.4 Future Work	3.3-15
	3.4 Coupled Fireball - INPORT Tube Code Development	3.4-1
4.	PLASMA CHANNEL MHD CODE DEVELOPMENT	4.1-1
	4.1 FIRE and MAGDIF: Design Philosophy	4.1-1
	4.2 Description of MAGDIF	4.2-1
	4.2.1 Formulation of the Problem	4.2-1
	4.2.2 Solution of the Problem	4.2-2
	4.2.2.1 Comparison with an Analytic Solution	4.2-3
	4.2.2.2 The Current Equation	4.2-11
	4.2.2.3 The Conservation Relations	4.2-17
	4.3 Summary	4.3-1
5.	ION PROPAGATION THEORY	5.1-1
	5.1 Introduction	5.1-1
	5.2 Particle-Beam and Pulsed-Power Requirements	5.2-1
	5.3 Beam-Plasma Theory	5.3-1
	5.4 Plasma Stability Constraint Calculations for LIBRA	5.4-1
	5.5 Ion Beam Propagation	5.5-1
	5.6 Repetitive Ion Diode for LIBRA	5.6-1
6.	SUMMARY AND CONCLUSIONS	6-1

1. INTRODUCTION

This is a progress report of work performed between January 1, 1983 and December 31, 1983 by Fusion Power Associates under contract to Kernforschungszentrum Karlsruhe. The purpose of this work was to start a detailed investigation of "critical issues" associated with the conceptual design of the LIBRA Light Ion Beam Fusion Demonstration Reactor. These critical issues all relate to the nuclear island part of the conceptual design. They include:

(1) Modeling of preformed plasma channel creation by a discharge through a cavity gas.

(2) Modeling of ion beam transport through a preformed plasma channel.

(3) Modeling of the cavity gas response to a target explosion.

(4) Modeling of INPORT unit response to an expanding fireball.

Most of the work discussed in this report remains "in progress", however, considerable advances have been made toward the goals of analyzing and clarifying the LIBRA reactor. This progress can be most clearly seen by comparing this report with its counterpart from 1982, FPA-82-7.

The LIBRA reactor is a demonstration facility driven by high current light ion beams transported through preformed plasma channels. A schematic view of the reactor and blanket is shown in Fig. 1.1. Major parameters for the system are given in Table 1.1. A target yield of 320 MJ and a repetition rate of 1.5 Hz have been selected. The first wall is protected by INPORT units similar to those used in the HIBALL design. The target yield and repetition rate combine to produce 480 MW of fusion power. No blanket neutronics studies have been done for LIBRA but we estimate, using the results of previous studies, that the blanket multiplication will provide us with 612 MW of thermal power. At a 40% thermal efficiency, this gives 245 MW of gross

Fig. 1.1

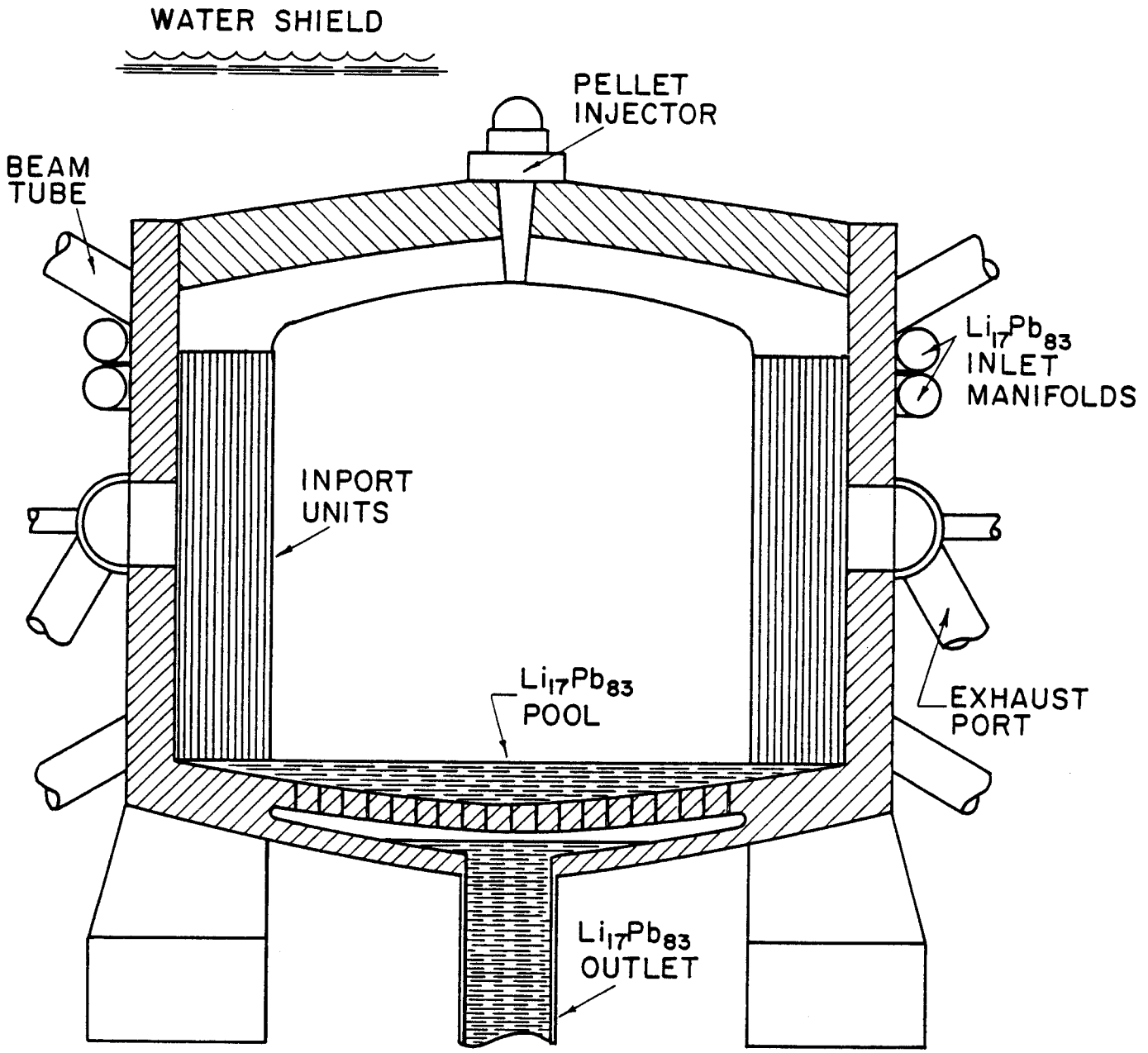

SCHEMATIC OF LIBRA REACTION CHAMBER

Table 1.1. Major LIBRA Parameters

Reactor Type	Demonstration, Electricity Production
Cost Goal	Less than 10^9 $
Ion Accelerator Type	Pulsed Power Diode or Multi-Stage
First Wall Protection	HIBALL-like INPORT Units
Ion Propagation Mode	Preformed Channels or Self-Propagation
Target Yield	320 MJ
Repetition Rate	1.5 Hz
Fusion Power	480 MW
Thermal Power	612 MW
Gross Electric Power	245 MW
Net Electric Power	215 MW

electrical power. With a recirculating power fraction of 12%, the net electrical power is 215 MW. Throughout this analysis the issues of (1) the type of ion accelerator, (2) its efficiency, and (3) its energy output have been left open. Of course, the LIBRA parameters were chosen to fall within the range of conceivable accelerator designs. It is within the context of these design parameters that the detailed work reported here was performed.

The following is a list of publications and presentations over the past year (1983) that relate to the LIBRA design.

1. K.J. O'Brien and G.A. Moses, "Intense Light Ion Beam Induced Charge and Current Densities in a Plasma Channel," Bull. APS 28, 1258 (1983).

2. R.L. Engelstad and E.G. Lovell, "Dynamic Response and Stability of INPORT Tubes in ICF Reactors," presented at the 5th Topical Meeting on the Technology of Fusion Energy, Knoxville, TN, April 1983.

3. R.L. Engelstad and E.G. Lovell, "Strength and Fatigue Analysis of Fibrous Silicon Carbide for ICF Reactor Applications," presented at the 3rd Topical Meeting on Fusion Reactor Materials, Albuquerque, NM, September 1983; to be published in the Journal of Nuclear Materials.

4. R.L. Engelstad and E.G. Lovell, "Mechanical Analysis of First Wall Tubes for the LIBRA Conceptual Reactor," to be published in the Proceedings of the 10th Symposium on Fusion Technology, Philadelphia, PA, December 1983.

5. R.L. Engelstad and E.G. Lovell, "Modal Analysis of First Wall Tube Banks for Light Ion ICF Reactors," to be presented at the 2nd International Modal Analysis Conference, Orlando, FL, February 1984.

In addition to the papers listed above, there were 2 common meetings held in 1983 in the Federal Republic of Germany (January and July). These meetings were very instrumental in guiding the research direction in the LIBRA design.

2. INPORT UNIT STRUCTURAL ANALYSIS

2.1 Introduction

The first part of this section consists of a progress report on the program characterizing strength of silicon carbide for potential ICF applications. This is followed by results for mechanical response of INPORTs previously documented in the mid-year summary. In addition, results are presented for response analysis at lower repetition rates including the effects of assessing the velocity of lithium/lead within INPORT units.

2.2 Progress in Fatigue Testing of Silicon Carbide Fiber

Considerable interest has been shown in silicon carbide fiber for applications in ICF reactor chamber design. Limited tensile test data and the absence of fatigue properties have led to an effort in characterizing static and cyclic mechanical strength. Tension test results were presented in an earlier annual report; the following consists of an update on fatigue analysis.

The fiber used is "NICALON®," manufactured by a polymer pyrolysis process by Nippon Carbon Co., Japan. It is composed of ultrafine β-SiC crystals with excess carbon. The number of filaments per yarn is 500, with an individual average diameter of 12.6 μm. The gauge length for all samples tested was 15 cm and the maximum load frequency was 0.25 Hz. The load state consisted of a tensile mean stress (σ_m) and a cyclic alternating stress (σ_a). The various combinations were such as to produce a maximum value less than the fracture stress (σ_f) and a minimum greater than zero. In Fig. 2.1, alternating stress as a fraction of fracture stress is plotted as a function of the number of cycles to failure. Note that the curve for σ_m/σ_f equal to 40% terminates at a value of σ_a/σ_f equal to 40%. Curves for mean stresses of 50% and 60% have

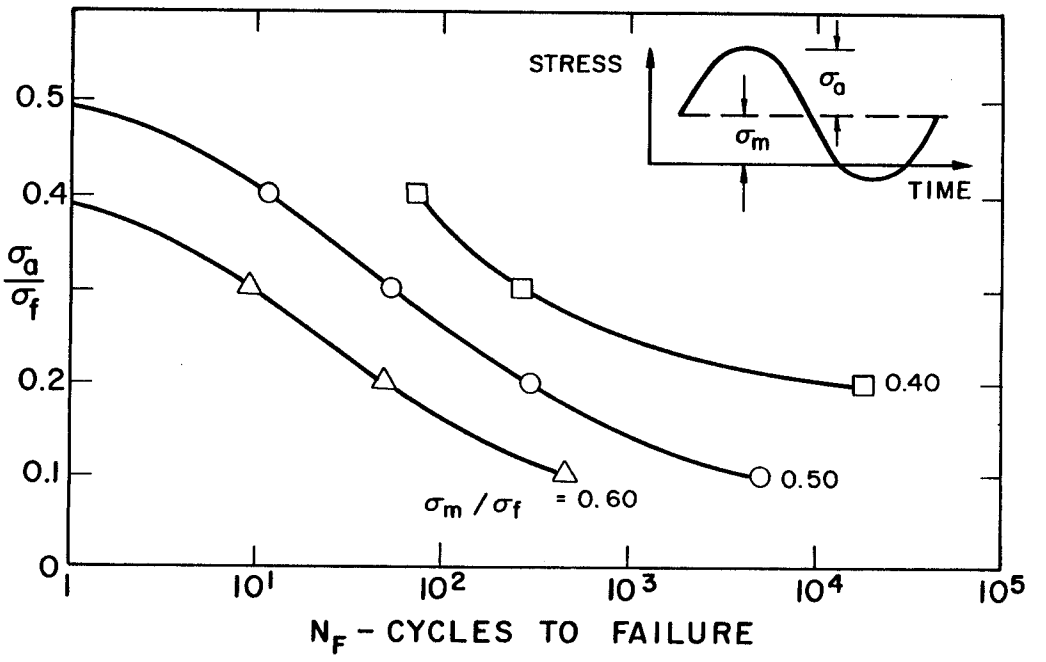

Fig. 2.1. Alternating stress amplitude vs. number of cycles to failure.

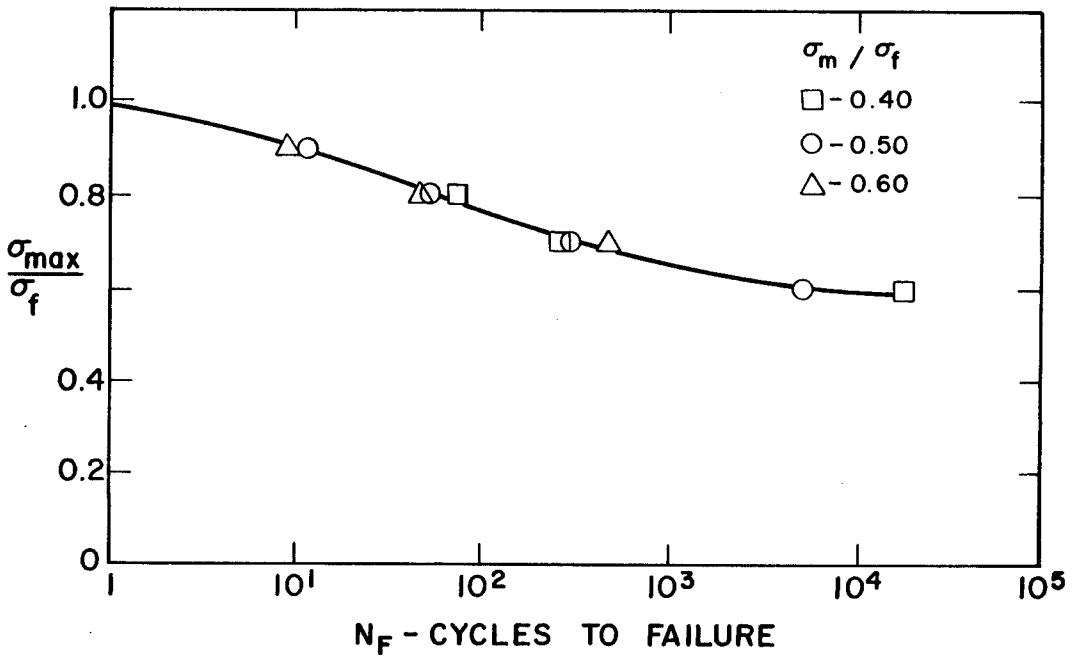

Fig. 2.2. Maximum tensile stress vs. number of cycles to failure.

been extended to the simple tension data corresponding to $N_F = 0.5$. Similarly maximum tensile stress can be plotted as a function of the number of cycles to failure as shown in Fig. 2.2. The results indicate the possibility of an endurance limit but additional high cycle tests are needed. The development of graphs such as Fig. 2.3 can be useful for design purposes. Rays are shown for different ratios for σ_a/σ_m, the largest acceptable value being 1.0. In using such curves, for example, a point stressed to state "A" could sustain 10^2 cycles but not 10^3. SEM micrographs were also taken of fatigued fibers. Figures 2.4 and 2.5 are typical, characterized by a more complex or rougher fracture surface than static tension. A small percentage of fibers failed on inclined surfaces in more complex patterns. Figure 2.6 shows a scalloped curved surface usually associated with progressive cyclic failure.

Future work should include high cycle fatigue of fiber bundles and static strength tests of improved INPORTs.

2.3 Dynamic Response of First Wall INPORT Units

The cylindrical cavity of LIBRA is encircled by an annular tube bank of INPORTs -- tubular components with pliable porous walls of silicon carbide fiber. Liquid $Li_{17}Pb_{83}$ flows axially within the INPORTs and also through the tube wall to develop a thin protective external film as shown in Fig. 2.7. INPORTs can and have been braided as seamless tubes with supplementary axial fibers for extensional strength and stiffening. It is also possible to use an orthogonally woven fabric to manufacture a tube with inherently superior axial strength and stiffness but having the disadvantage of a seam. INPORTs are supported at both the top and bottom of the LIBRA reaction chamber. A schematic design shown in Fig. 2.8 would provide for top assembly and pretension

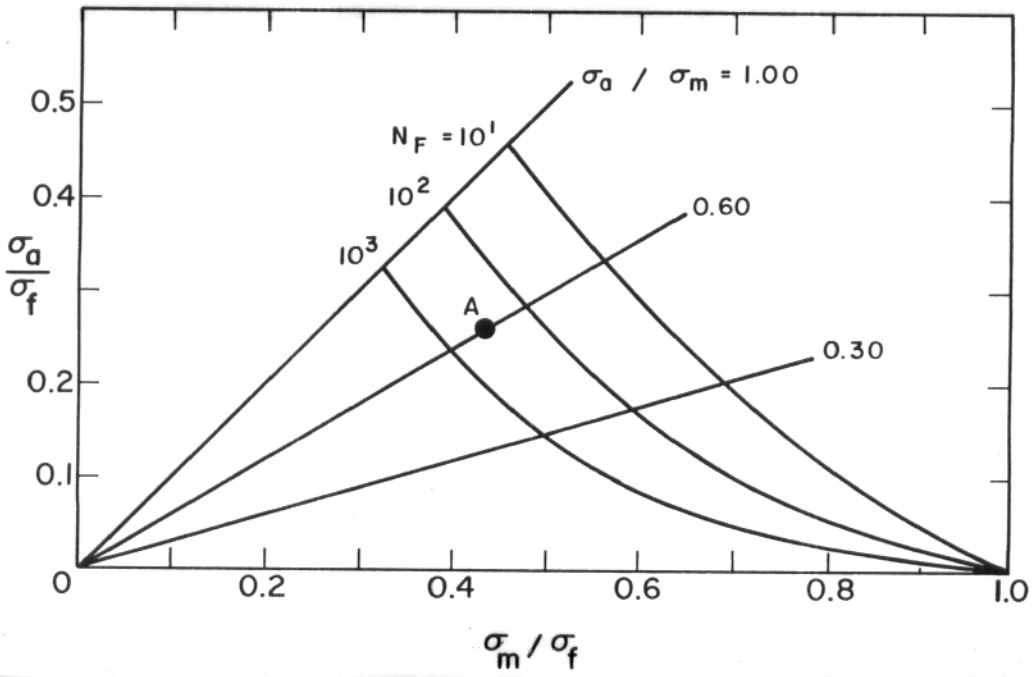

Fig. 2.3. Alternating stress vs. mean stress for various cycles to failure.

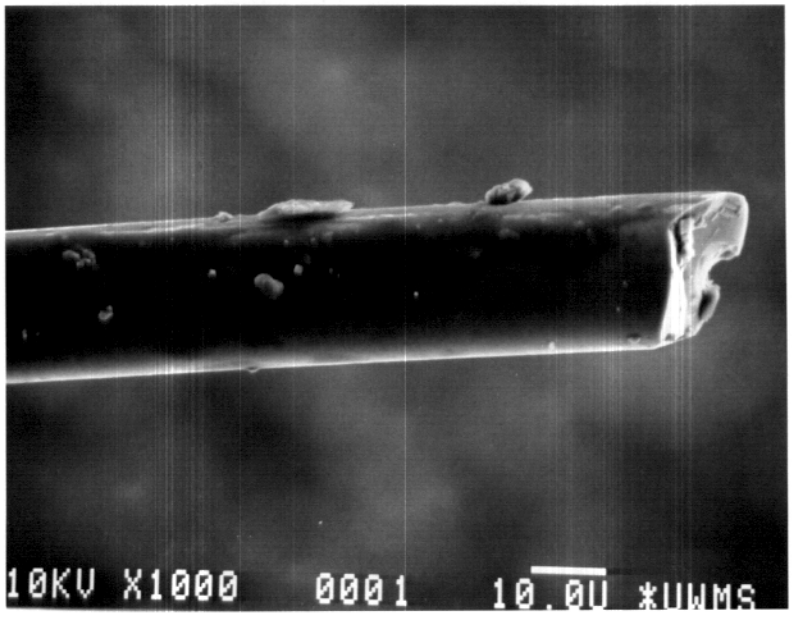

Fig. 2.4. Fatigue fiber fracture at 18,600 cycles for σ_m/σ_f = 40%; σ_a/σ_f = 20%.

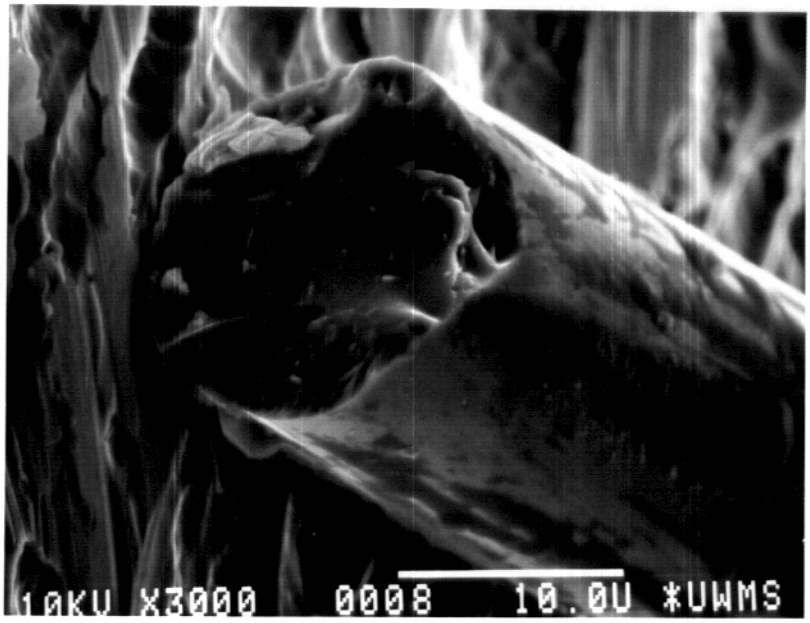

Fig. 2.5. Fatigue fiber fracture at 18,600 cycles for σ_m/σ_f = 40%, σ_a/σ_f = 20%.

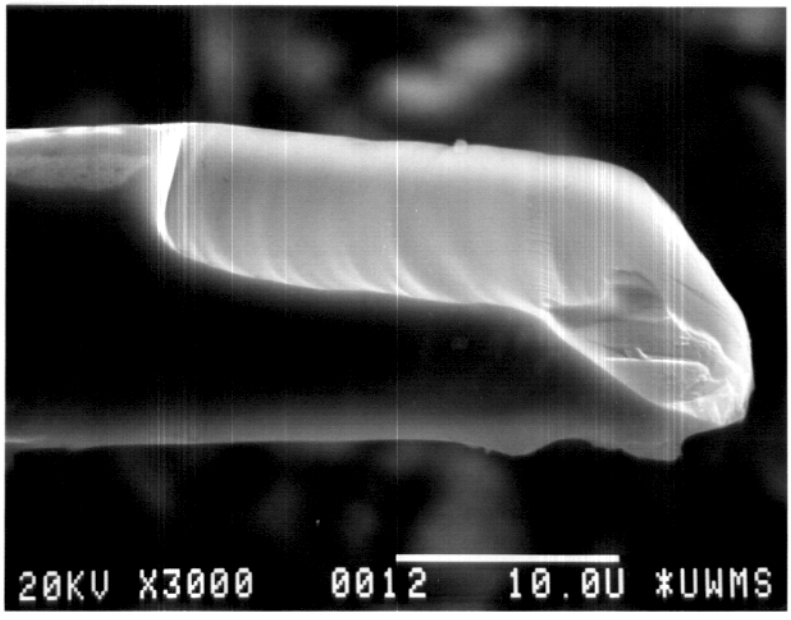

Fig. 2.6. Fatigue fiber fracture at 13,700 cycles for σ_m/σ_f = 40%; σ_a/σ_f = 20%.

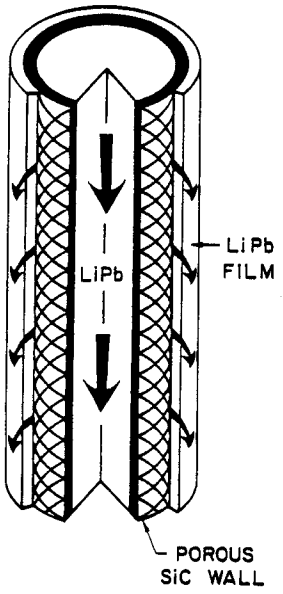

Fig. 2.7 Sectioned INPORT Unit.

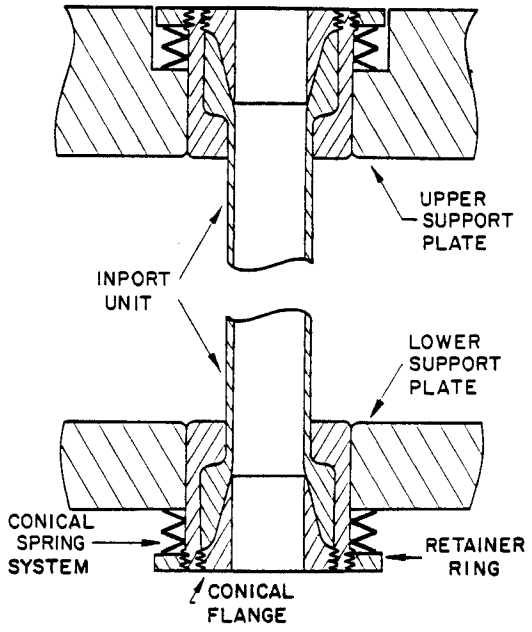

Fig. 2.8 Support Mechanisms for INPORTS.

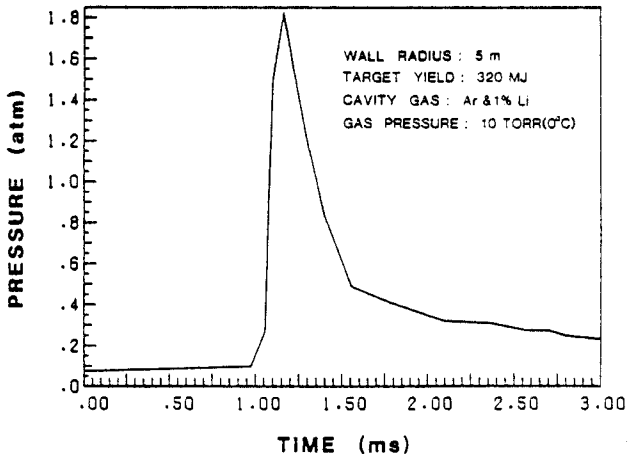

Fig. 2.9. Pressure at First Wall.

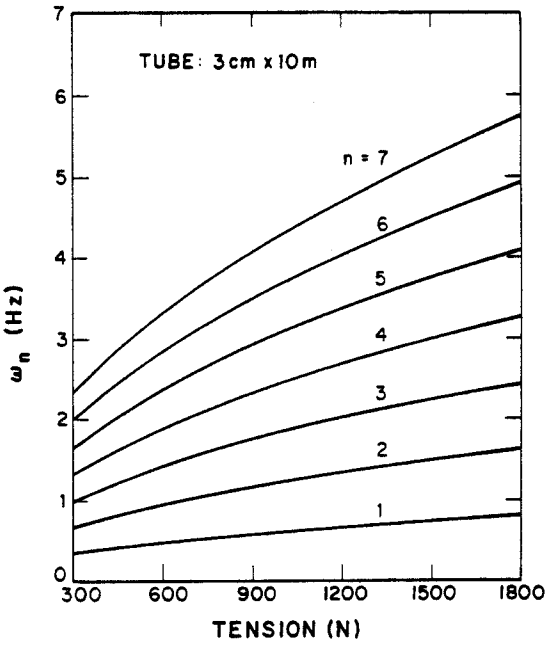

Fig. 2.10. INPORT Vibration Frequency vs. Tension.

with compression spring systems. Flanged ends of INPORTs can be rigidized and strengthened by chemical vapor deposition of additional SiC.

INPORTs are subjected to a repetitive mechanical shock transmitted through the cavity gas. Such a pulse, as determined by the FIRE code, is shown in Fig. 2.9. A computer code has been developed for calculating the response of INPORTs to dynamic sequential overpressures for tubes of various lengths, levels of damping and pretension. The response depends upon a number of characteristics including the natural vibration frequencies. From Fig. 2.10 it can be seen that tension variations have a modest influence on frequencies for lower modes and a stronger effect on higher modes. For a nearly uniform dynamic pressure, the largest contribution to the total motion will be from the fundamental mode which has a natural frequency less than 1 Hz. Thus, resonance does not appear to be a potential problem for the repetition rates anticipated in the LIBRA design. It should also be noted that INPORT displacements will be essentially symmetric about the midplane and consequently modes with an even number of half-waves (2, 4, etc.) will not be influential. In addition, vibration periods of INPORTs are substantially greater than the pulse width of the shock and thus its effect will be practically the same as an impulsive pressure.

The results presented are based upon a tube diameter of 3 cm and the loading of Fig. 2.9 which corresponds to an impulse of 87 N sec/m^2. The first series of calculations were carried out at a repetition rate of 5 Hz. In Fig. 2.11 it can be seen that small increases in tension significantly reduce displacements but larger increases are not relatively as effective. Length reductions substantially reduce maximum INPORT displacements as shown in Fig. 2.12. However, for such cases, the design problems for the required inter-

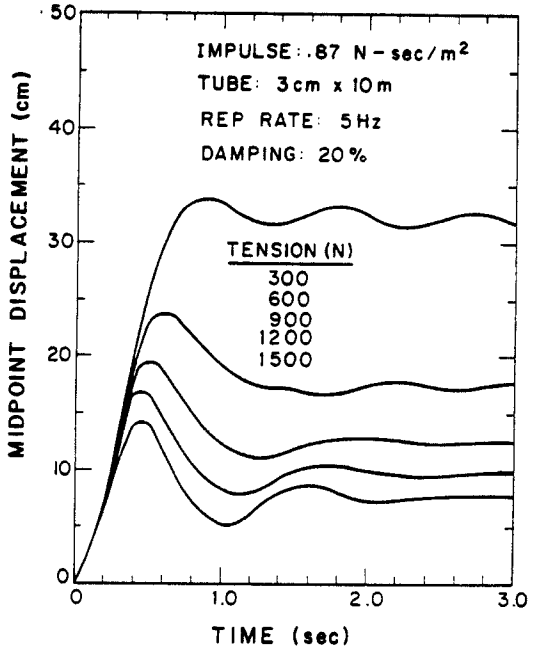

Fig. 2.11. INPORT Mechanical Response at Startup.

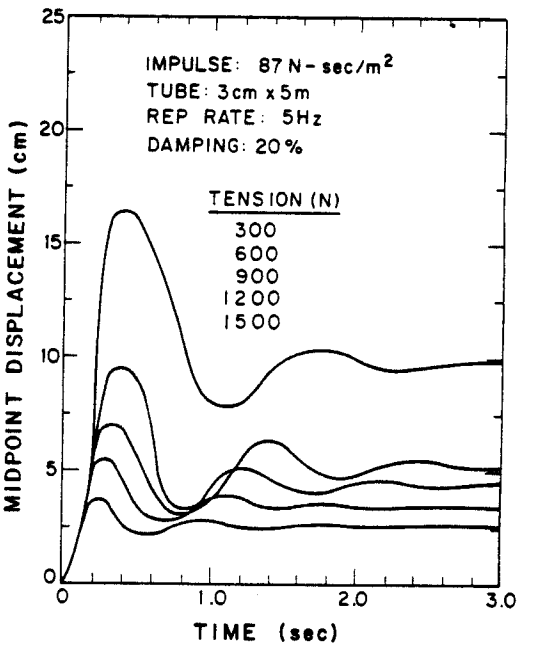

Fig. 2.12. INPORT Mechanical Response at Startup.

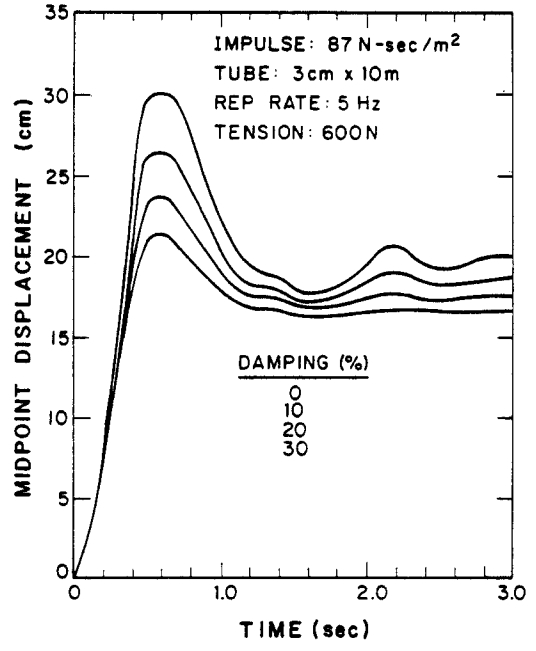

Fig. 2.13. INPORT Mechanical Response at Startup.

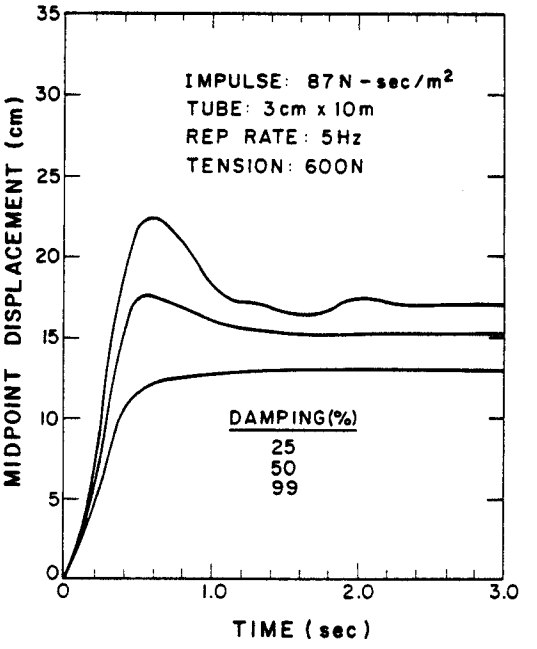

Fig. 2.14. INPORT Mechanical Response at Startup.

mediate supports are unresolved. The results of Fig. 2.13 indicate that changes in damping levels do not produce dramatic changes in response, particularly for the steady state amplitude. This is also shown in Fig. 2.14 which includes the academic case of 99% critical damping. Maximum transient displacement and steady state amplitudes are plotted in Figs. 2.15 and 2.16 for different tensions and damping. Finally for this repetition rate, Fig. 2.17 shows a typical transient and steady state response for sequential impulses applied for 3 seconds followed by shutdown. The free vibration of INPORTs after load cessation does not appear to have unusual characteristics requiring special design considerations.

A second series of mechanical response calculations was also done at lower repetition rates. In addition, the code was improved to account for the effects of the velocity of the liquid metal. The INPORT length and diameter are 10 m and 3 cm respectively; the damping level was a constant value of 20%. The first effect of the liquid metal velocity can be seen in Fig. 2.18. As the fluid velocity increases, the natural frequencies of the INPORTs drop, with the value producing a frequency of zero identified as the critical velocity. The frequencies shown correspond to the first and third harmonics (one and three half waves, respectively). Midpoint displacement histories are shown in Figs. 2.19 and 2.20 for a repetition rate of 1.5 Hz. A change in the fluid velocity from zero to 6 m/s (63% of the critical velocity) results in a steady state mean displacement which is larger but with a reduced alternating amplitude after motion has stabilized. Similar effects can be seen in Figs. 2.21 and 2.22 for a reduced repetition rate of 1.0 Hz. However, the alternating amplitudes for fully developed motion in these two cases are large and would degrade the fatigue life of the components. In Figs. 2.23 and 2.24, the

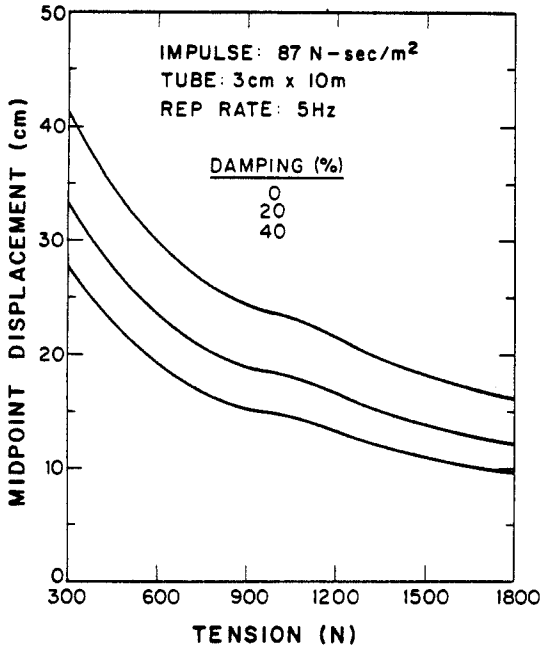

Fig. 2.15. Maximum Transient Response of INPORTS.

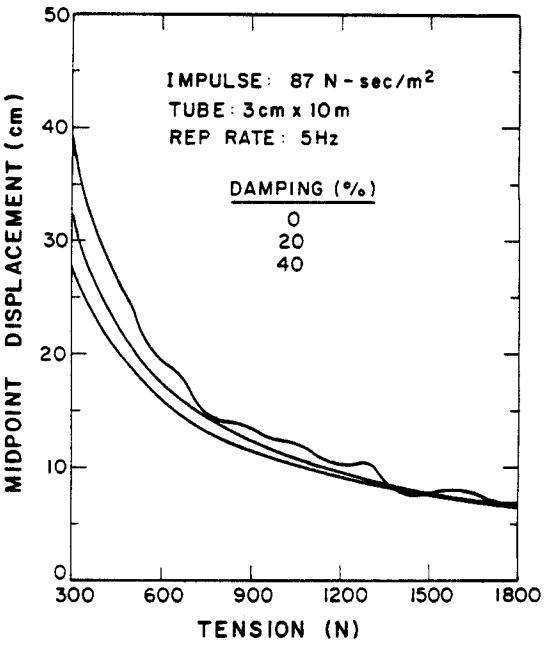

Fig. 2.16 Steady State Response of INPORTS.

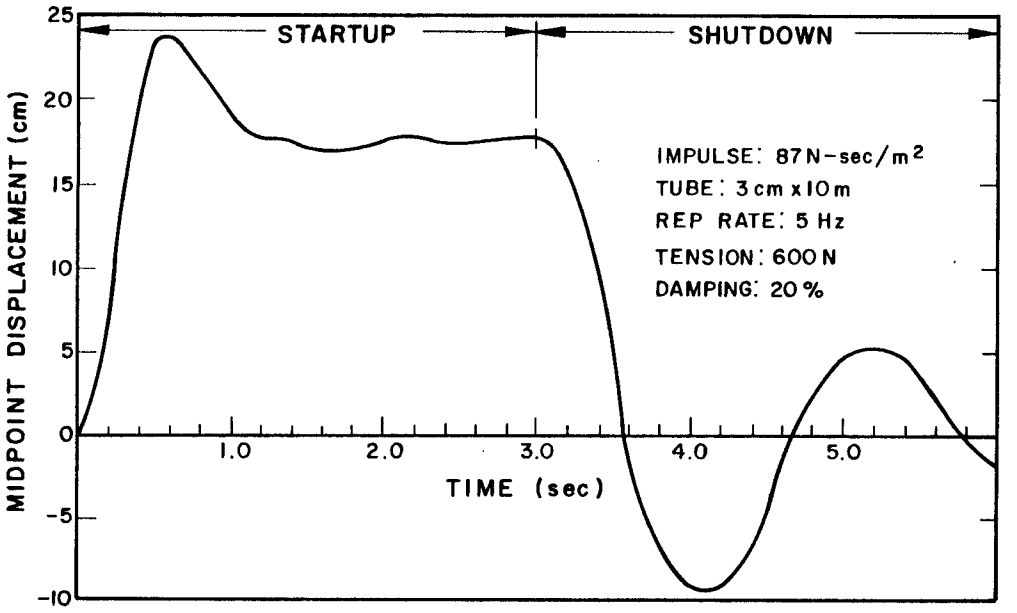

Fig. 2.17. INPORT Mechanical Response -- Startup and Shutdown.

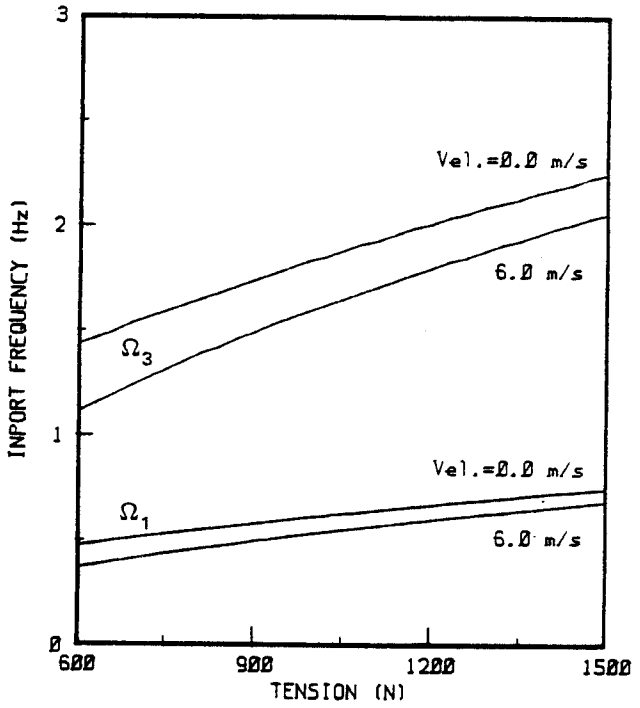

Fig. 2.18. INPORT natural frequencies vs. preload tension.

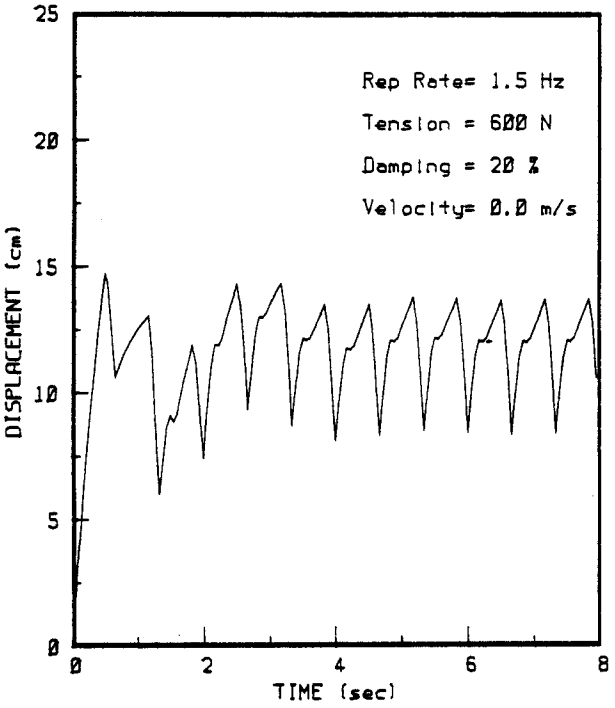

Fig. 2.19. INPORT Midpoint Displacement vs. Time.

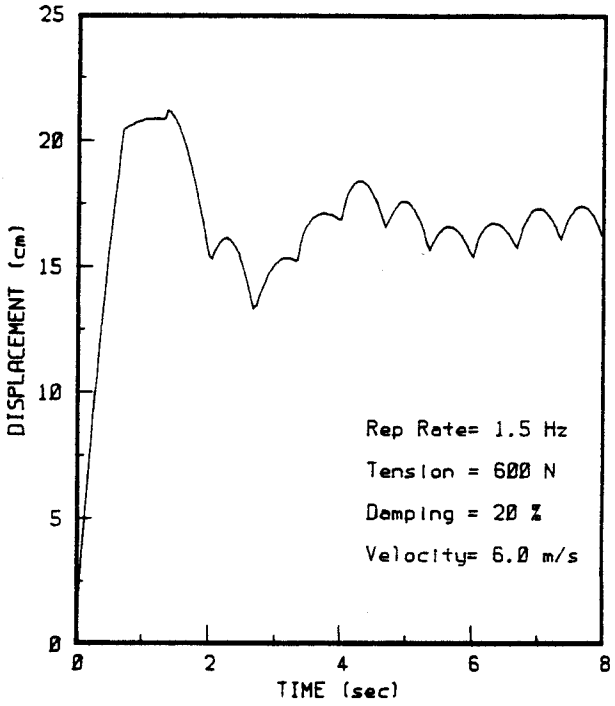

Fig. 2.20. INPORT Midpoint Displacement vs. Time.

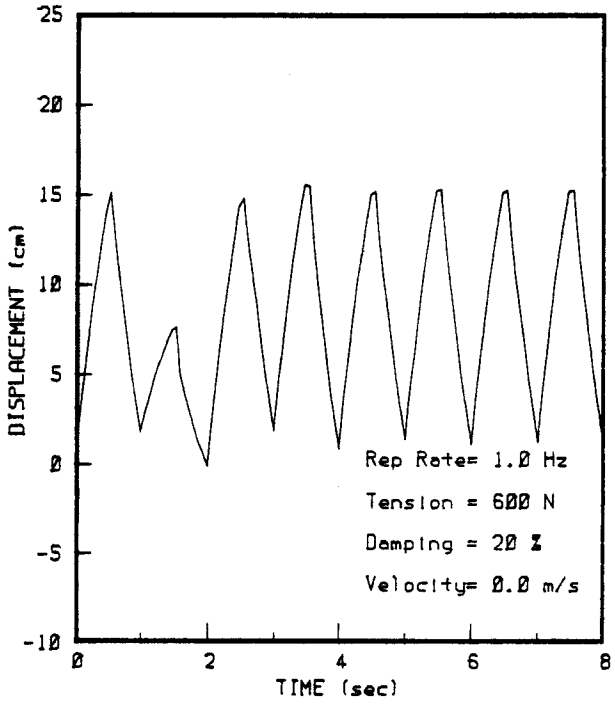

Fig. 2.21. INPORT Midpoint Displacement vs. Time.

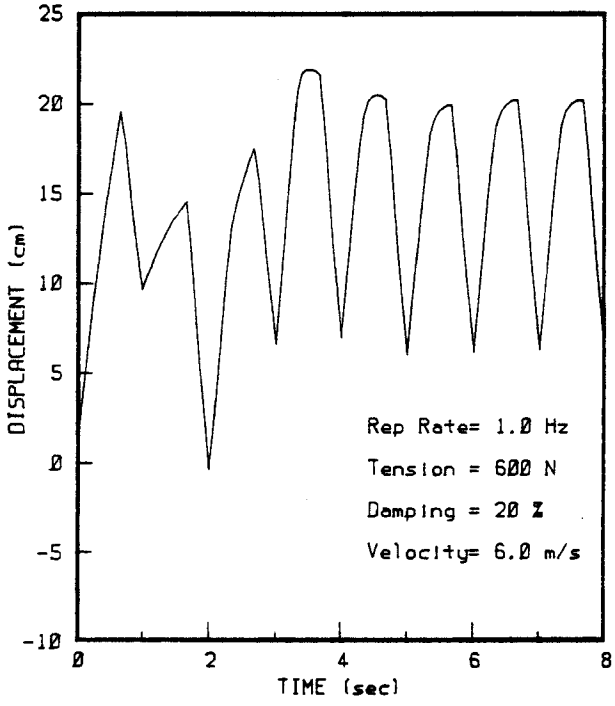

Fig. 2.22. INPORT Midpoint Displacement vs. Time.

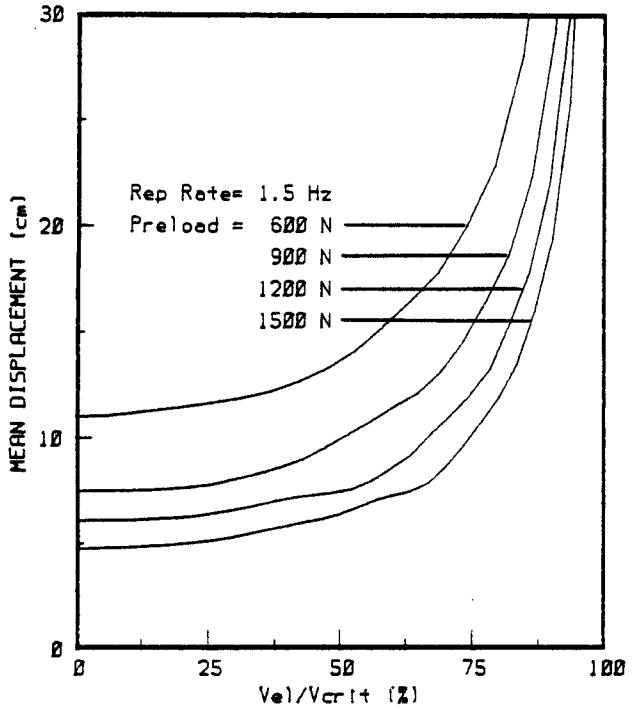

Fig. 2.23. Steady State Mean Displacement vs. Fluid Velocity Ratio.

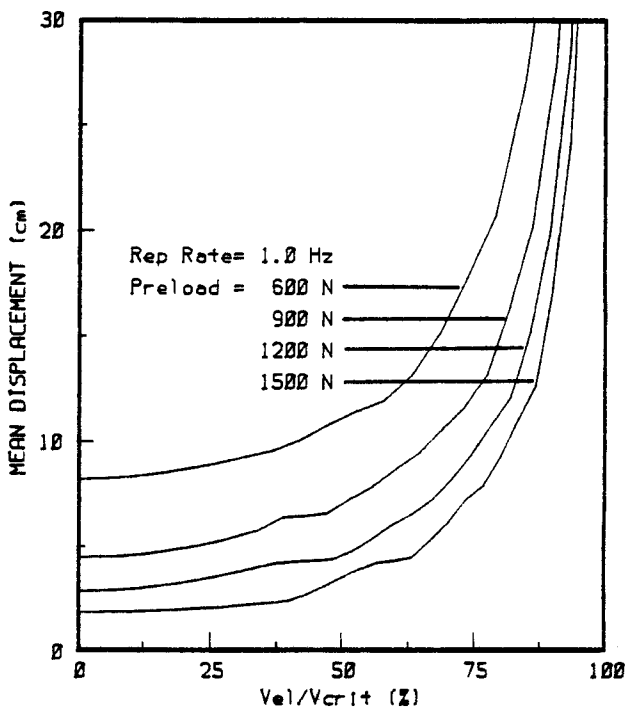

Fig. 2.24. Steady State Mean Displacement vs. Fluid Velocity Ratio.

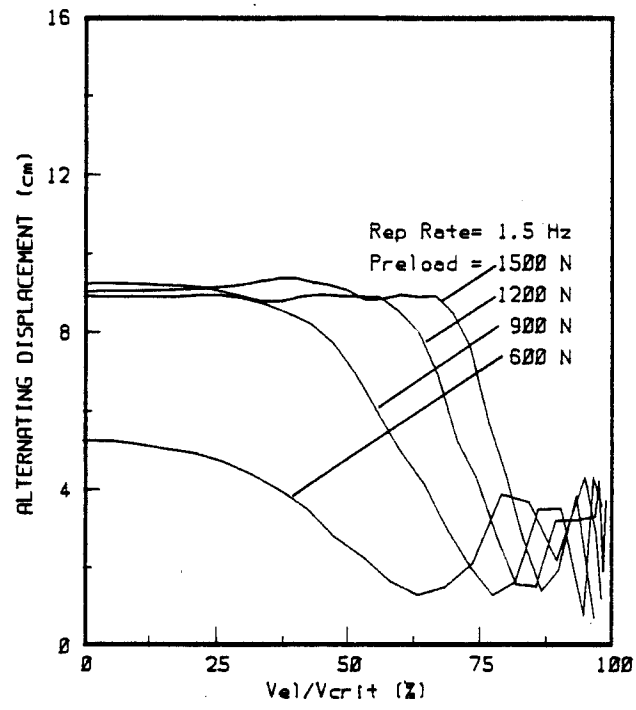

Fig. 2.25. Steady State Alternating Displacement vs. Fluid Velocity Ratio.

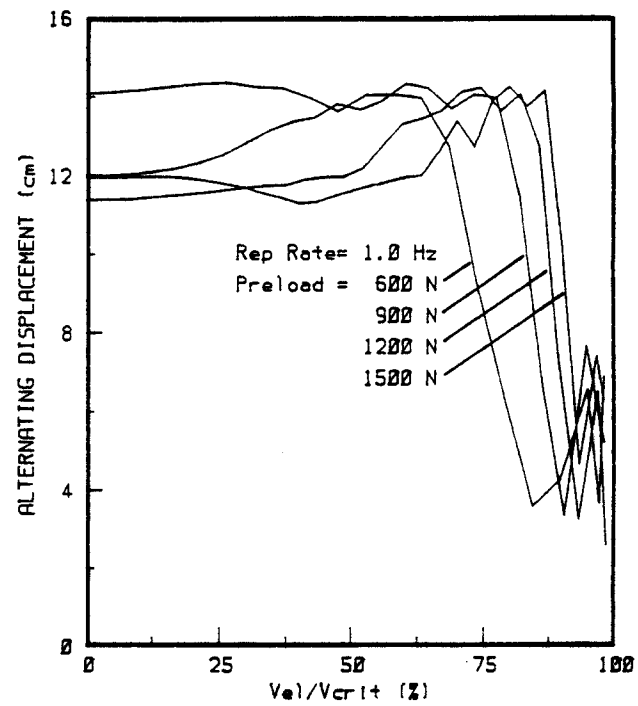

Fig. 2.26. Steady State Alternating Displacement vs. Fluid Velocity Ratio.

steady state mean displacement amplitude at 1.5 and 1.0 Hz is shown as a function of the critical velocity ratio for various tensile preloads. Clearly, the mean displacement increases with increasing fluid velocity but can be controlled at lower velocities with larger preload forces. More pronounced response is shown in Figs. 2.25 and 2.26 for the alternating displacement. Generally the amplitude of this component is rather insensitive to initial increases in the liquid velocity but decreases quickly for larger velocities and subsequently oscillates moderately as the upper limit is approached. The amplitude of the alternating displacement is typically lower for a repetition rate of 1.5 Hz as compared with 1.0 Hz.

The results obtained for dynamic mechanical response of INPORTs are encouraging and appear compatible with the overall design of LIBRA at this time.

3. CAVITY GAS DYNAMICS AND HEAT TRANSFER

3.1 Introduction

A critical problem following the explosion of a light ion beam fusion target in the LIBRA reactor is the behavior of the cavity gas that is present for the establishment of preformed plasma channels for beam propagation. This cavity gas must have a density which produces a pressure of 5-50 Torr at 0°C. This high density results in phenomena that are significantly different from those in the near vacuum that was present in the HIBALL design.[1]

One such effect is that much of the non-neutronic target yield is absorbed by the gas in a small volume around the target and this forms a fireball. This absorption protects the first wall from damage due to direct target x-ray and ion fluxes but the resulting fireball can put a thermal heat flux and a shock pressure pulse on the wall. The nature of this fireball for LIBRA is discussed in Section 3.2.

Another effect of high gas density is the difficulty in extracting all of the energy out of the gas between target explosions. If the gas cools only through radiation to the walls, the gas temperature will not drop below ~ 3000-8000 K in one second. This may have a detrimental effect on the target injection and on the formation of plasma channels. In LIBRA, the idea has been to flow the gas through an array of INPORT[1] tubes, which greatly increases the surface area for conduction and radiation of heat from the gas. The shock motion of the fireball forces much of the gas through the array and stimulates convective heat transfer. Heat transfer from the gas to these tubes is discussed in Section 3.3. These tubes may be coated with a liquid metal film to protect the structure of the tubes from high heat fluxes. The

heat transfer to the tubes warms the film and may vaporize some of it. The details of this process are also discussed in Section 3.3.

To most accurately test this problem, the behavior of the fireball must be coupled to the vaporization and condensation of liquid metal on the tube surfaces. One needs a self-consistent treatment of the tube and gas behavior to model the process properly. The combination and modification of two existing codes has been done to attempt this modeling. This is discussed in Section 3.4.

3.2 Fireball Analysis

This past year has seen additional fireball dynamics calculations through a cooperation between scientists at FPA and KfK. Calculations at 5 m and 7 m from the target, corresponding to the first row of INPORT tubes and both the wall in back of the tubes and the roof of the reactor chamber, have provided needed information for tube and roof mechanical designs and for consideration of heat transfer to and in the tubes. A version of FIRE, the computer code used for these calculations, is now operating at KfK and has been used in conjunction with their two-dimensional hydrodynamics calculations. All of the calculations have assumed an argon + 0.2% lithium cavity gas at a density corresponding to a pressure of 10 Torr at 0°C and a target yield of 320 MJ.

The MFFIRE[2] code has been used to perform multigroup radiative heat transfer Lagrangian hydrodynamic simulations of fireball behavior. The term "fireball" refers to the ball of hot gas, which is created through the absorption in the cavity gas of the target x-rays and debris ions. This fireball eventually releases much of the energy to the wall in the form of a heat flux and a shock wave. The simulations presented in this section ignore the

effects on fireball behavior of vaporization. Code development for CONRAD, a code which does include these effects, is discussed in Section 3.4.

The heat and shock loads on the first row of tubes have been calculated and are shown in Fig. 3.1, plotted against the log of time. It can be seen here that the width of the heat pulse is a few tenths of a μsec but that it has a very high maximum at 0.9 MW/cm^2. The pressure pulse occurs much later at about 1 msec and is about 0.5 msec long. The high heat flux can cause ablation of the liquid metal on the surfaces of the INPORT tubes, an effect which is discussed in a later section.

A calculation done with the wall at 7 meters from the target explosion is relevant to the situation on the roof of the reactor chamber and the side wall behind the tubes. The conditions on the side wall are different from the prediction of this simulation because the effects on the gas flow through the tubes and the heat transfer to the tubes have been neglected. However, the simulation provides the velocity, temperature and density of the gas as it enters the array of tubes, parameters which are useful when considering the heat transfer to the tubes and mass flow of material from the tube surfaces.

The pressure and heat flux on a wall 7 m from the target explosion are shown in Fig. 3.2. Just as in the 5 m case, there is an early, very short but very intense, burst of radiation followed by the shock. The plasma temperature is shown in Fig. 3.3, plotted against position for several times. This shows that significant amounts of hot gas flow into the array of tubes at 5 m, meaning that there may be cooling and damping of the fireball by the first few rows of tubes. A plot of the mass density, Fig. 3.4, shows the increased mass density of the gas in the tube array. The velocity of the gas in the array is 6-9 x 10^4 cm/sec.

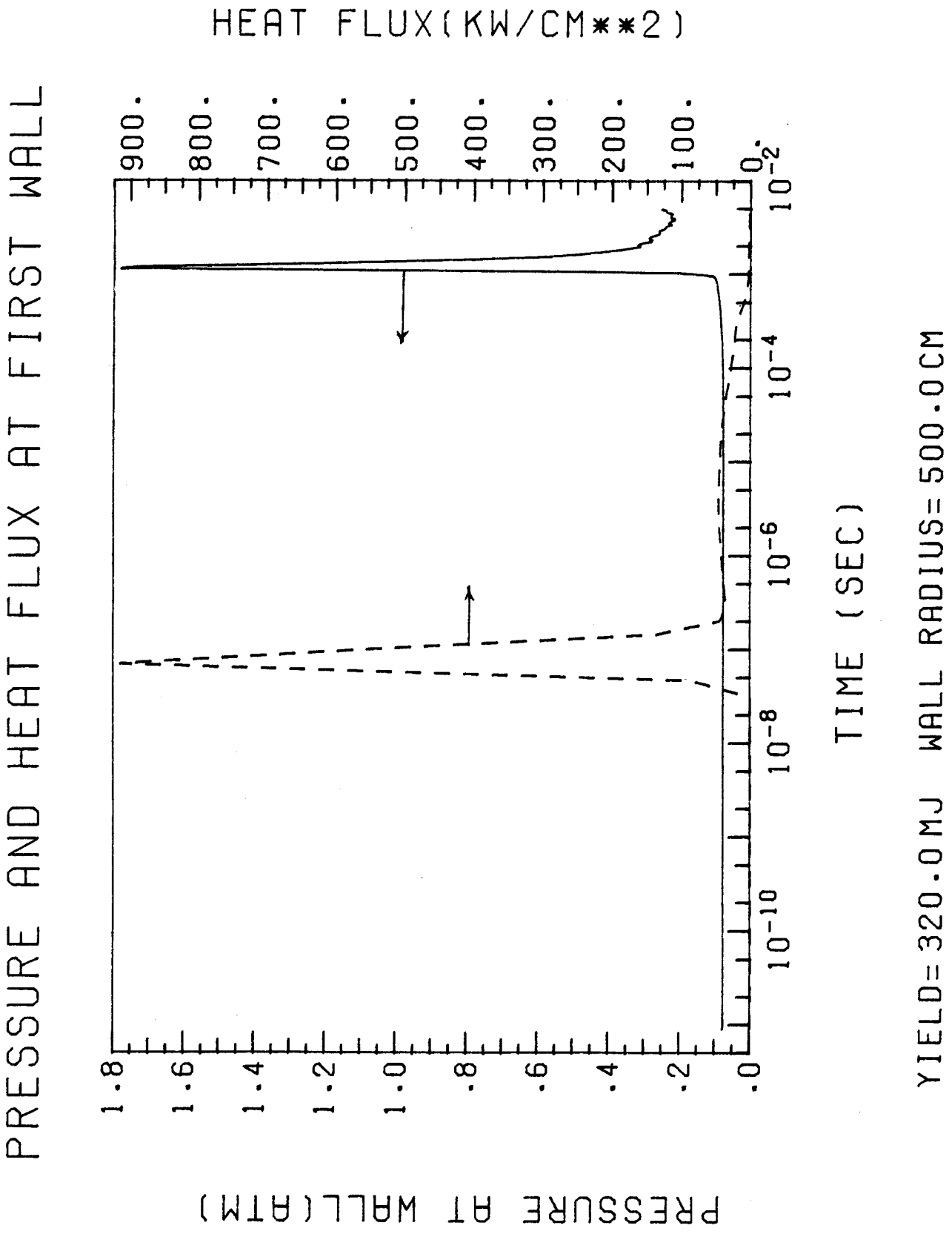

Fig. 3.1. Pressure and heat flux on first row of INPORT tubes in LIBRA reactor cavity.

Fig. 3.2. Pressure and heat flux at 7 meters from target explosion in LIBRA reactor cavity.

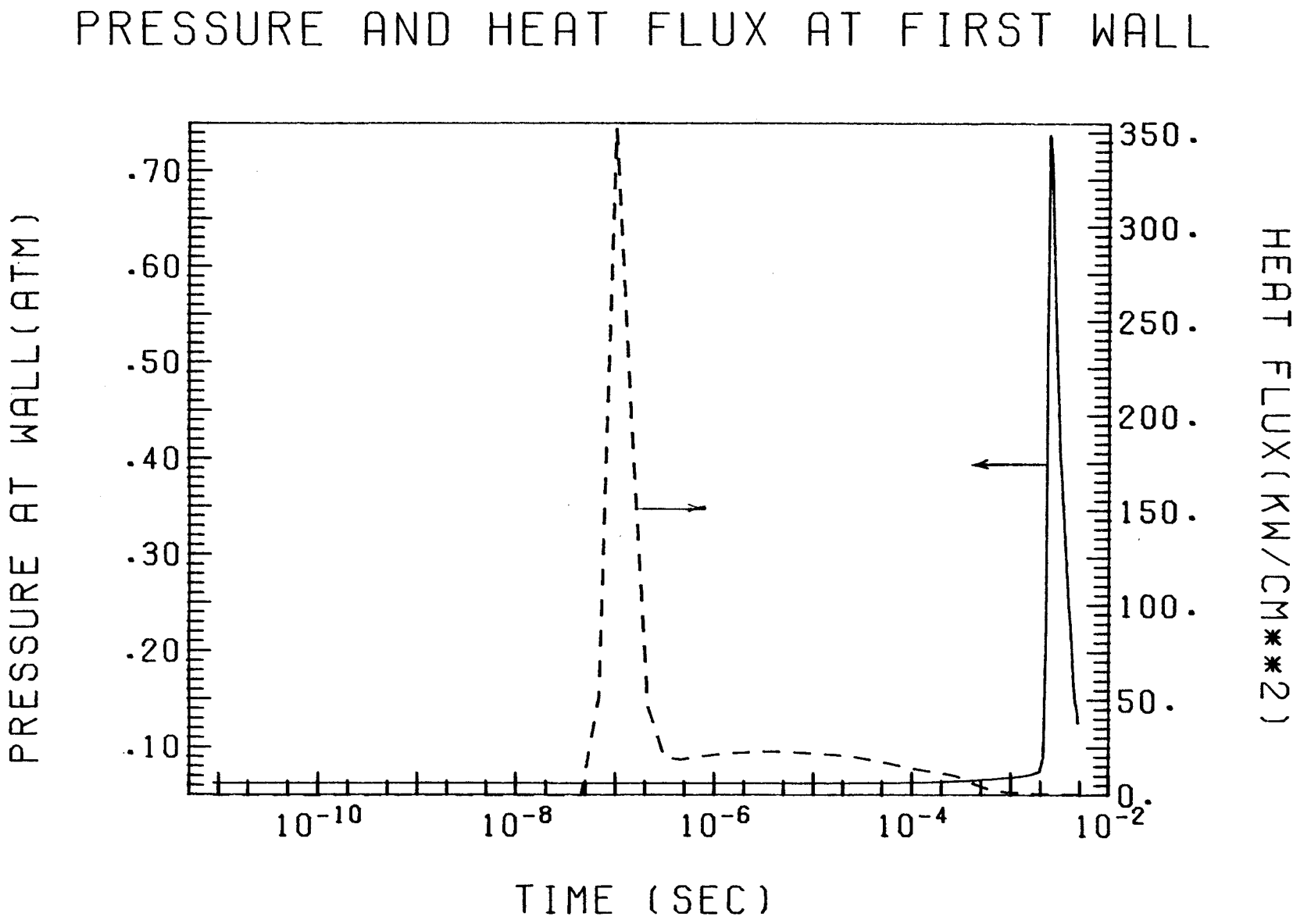

Fig. 3.3. Gas temperature versus radius at various times for LIBRA target explosion with 7 meter radius wall.

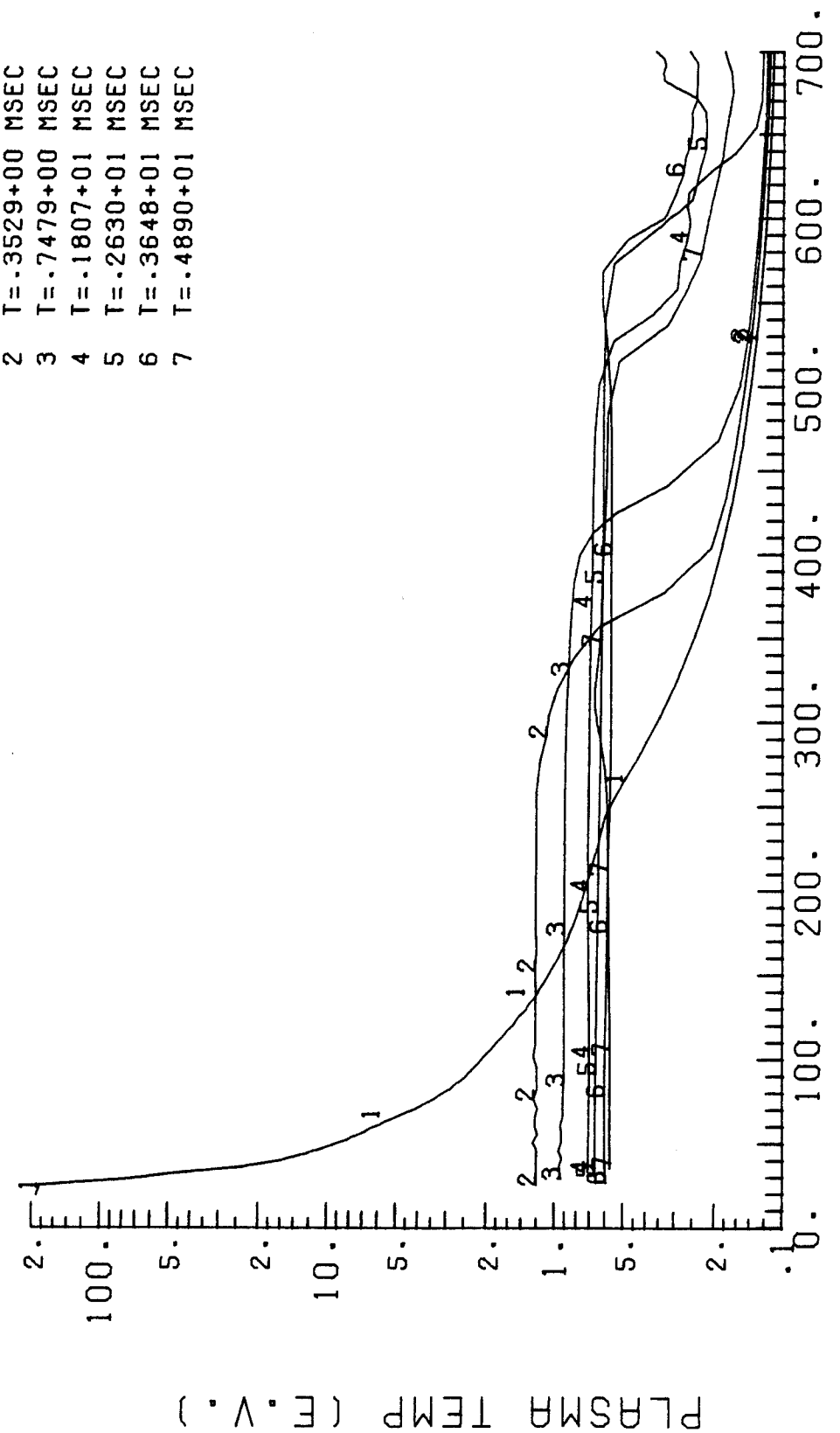

Fig. 3.4. Mass density of gas versus radius at various times for LIBRA target explosion with 7 meter radius wall.

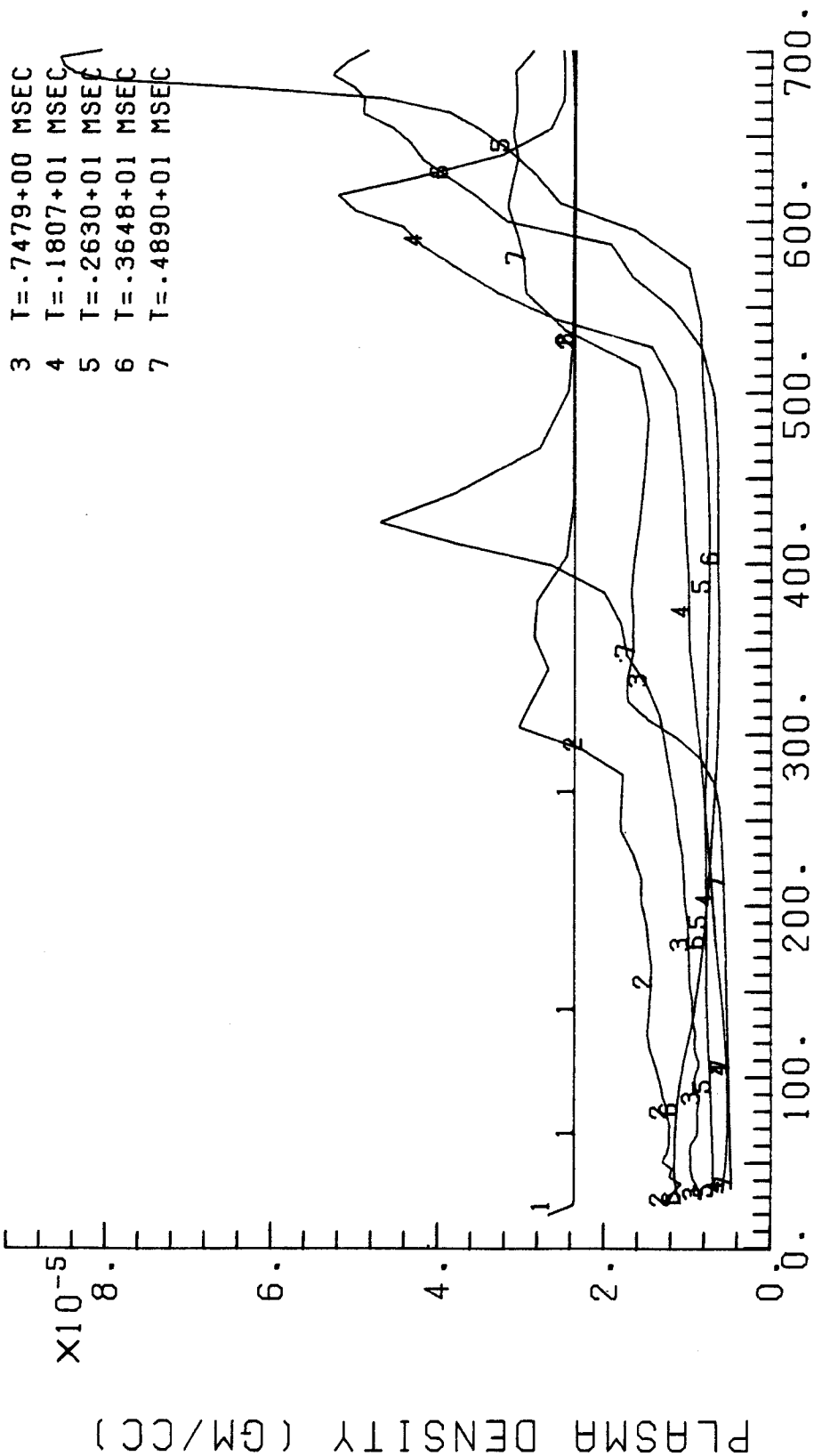

The results of these one-dimensional simulations are summarized in Table 3.1. Because flow through the tubes is an important two-dimensional effect, the MFFIRE code cannot tell the whole story. The work presented in some of the later parts of this chapter attempts to handle flow through tubes more accurately. Other two-dimensional effects result from the non-spherical shape of the target chamber. Scientists at KfK have used two-dimensional pure hydrodynamic simulations to model these effects where they have attempted to correct for the radiative heat transfer by benchmarking with FIRE results.

Table 3.1. One-Dimensional Fireball Simulations

Cavity gas	10 "Torr" Ar + 0.2% Li	10 "Torr" Ar + 0.2% Li
Wall radius (m)	5	7
Target yield (MJ)	320	320
Total target x-ray energy (MJ)	86.1	86.1
Initial fireball energy (MJ)	83.5	84.6
Maximum pressure on wall (MPa)	0.186	0.076
Energy radiated to wall (MJ) in [ ] msec	64.0 [5.0]	54.2 [5.0]
Energy density radiated to wall (J/cm^2)	20.4	8.8

3.3 Heat and Mass Transfer in INPORT Tubes

The current LIBRA design has a target yield of 320 MJ per event. Figure 3.5 shows the various dominant heat transfer mechanisms and their relative fraction of the total target yield. One will note that neutron heating is the largest of the three. Fortunately, modeling this portion is rather easy using simple volumetric absorption and heating in the LiPb coolant. The cavity gas is essentially transparent to this mechanism, therefore results from the HIBALL study[1] can be used in the current investigation. A volumetric heat flux of 5.28 W/cm^3 due to neutron heating will be experienced at the first tube row (at 5 m radius).

The remaining 27% of the target energy involves surface heat transfer to the tube surfaces: both thermal radiation and forced convection. The various energy exchange mechanisms and current modeling strategies are the subjects of this section. Figure 3.6 illustrates the relative energy partitioning as functions of time. From these figures, it is apparent that although the "hot gas" portion of the energy "pie" represents a relatively small portion of the total yield, it controls the overall time constant of the removal process. The end time is currently defined as when the cavity gas stagnation temperature has been reduced to 800°K.

Heat transfer at the tube surfaces occurs in three distinct phases; each dominated by different mechanisms and requiring separate modeling techniques. These phases are:

Phase I -- The cavity "fireball" radiates to the first surfaces. This phase is characterized by rapid energy deposition (1.5 msec) and must consider transpiration cooling due to evaporation of the liquid metal film.

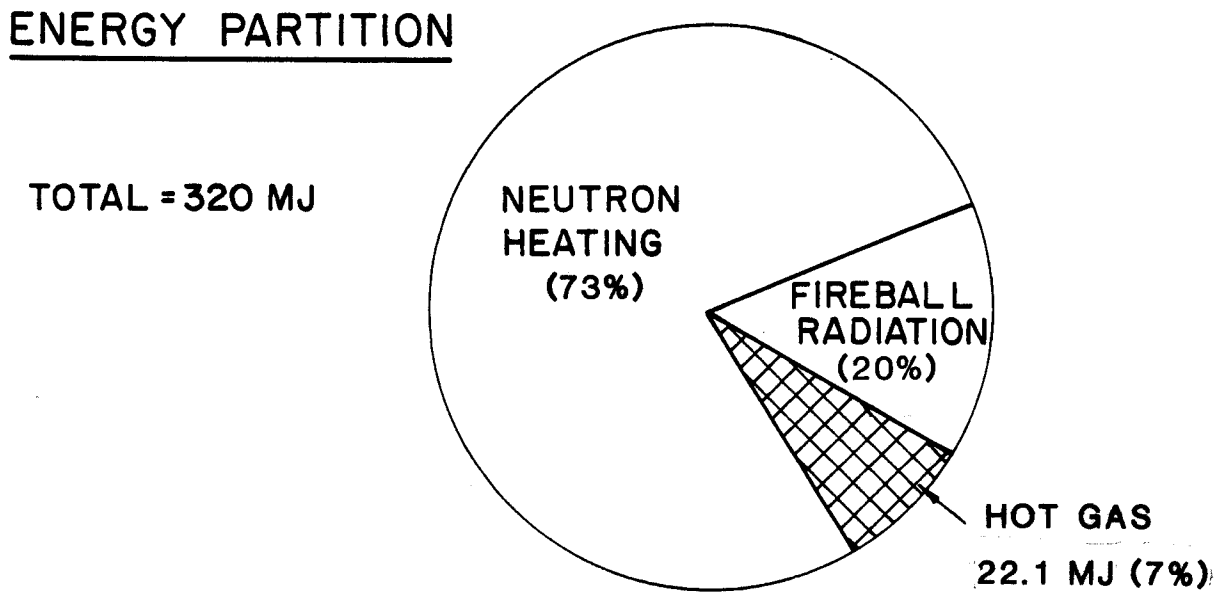

Fig. 3.5. Partitioning of LIBRA target yield energy.

TIME SCALE

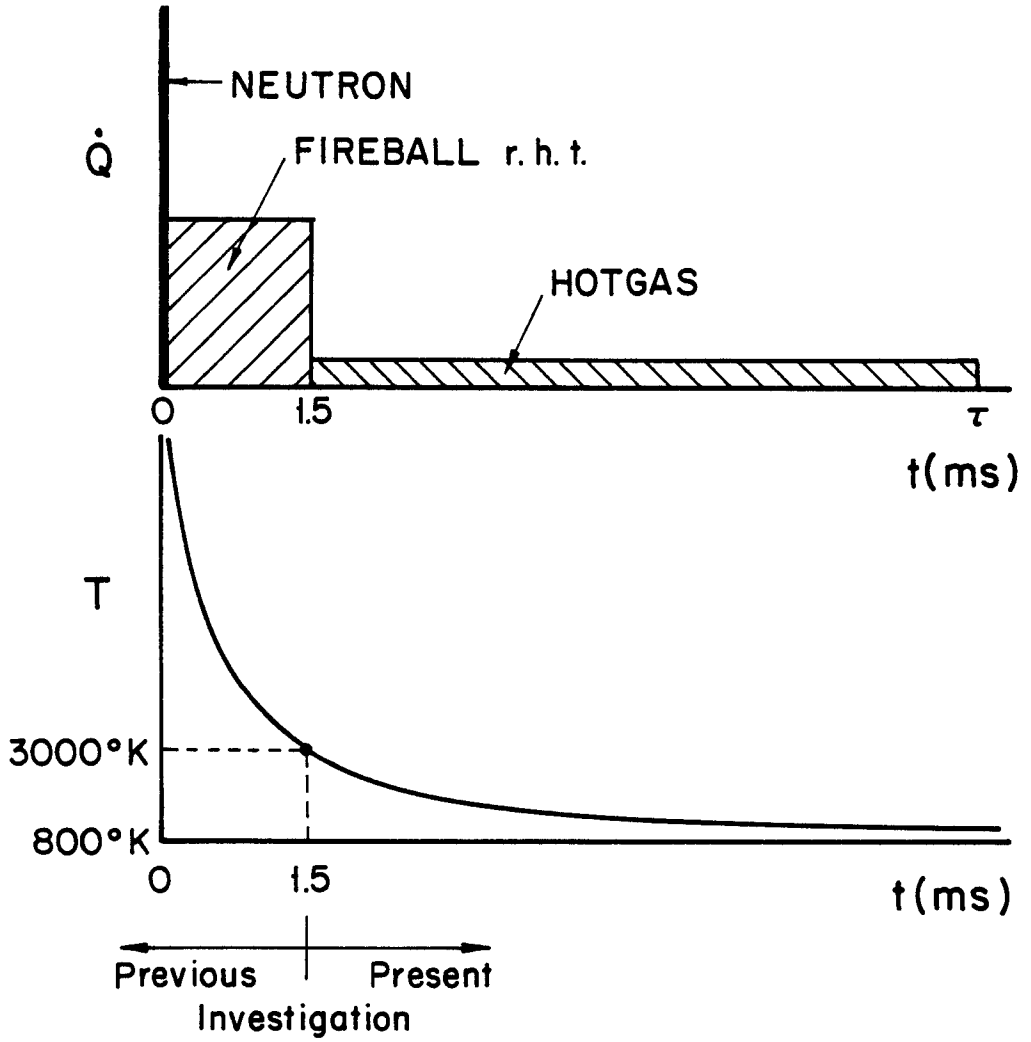

Fig. 3.6. Relative partitioning of LIBRA target yield versus time.

Phase II -- The central cavity gas, cooled to an average temperature of 3000°K, now propagates through the tubes. This pulse is initially supersonic (M = 2.5) and therefore compressible gas dynamics, radiation heat transfer, and entrainment of the liquid film are all important mechanisms which must be considered.

Phase III -- The hot gas has now been essentially thermalized due to wake effects in the tube bank and reflection from the back wall of the vessel. Simple isothermal gas radiation to the tubes is the dominant heat transfer mechanism.

3.3.1 Phase I

This phase is restricted to high temperature (plasma) radiation from the ionized cavity gas to the first ("line-of-sight") surfaces. Figure 3.1 presents results from the MFFIRE[2] code at a radius of 5 m. One can see that a very high, but short duration, heat flux pulse is experienced at the tube surface. This heat flux represents the re-radiated energy from the cavity gas; a delta-like pulse representing the unattenuated x-rays (2.6 MJ) occured earlier than this pulse, but is not shown in the figure.

The current LIBRA design has a liquid film external to the tubes to protect them from this rapid energy deposition: a transpiration cooling effect. However, the present MFFIRE code is unable to calculate this effect. Therefore, a simple one-dimensional conduction code which models the evaporation of the liquid film was written. This calculation presents an upper bound for the amount of ablated material since the two codes are decoupled; any radiation shielding effects from the ablated material are not considered. The results from these calculations are presented in Table 3.2. The surface of the film was modeled with 0.5 micron Eulerian zones. One will note that only about

Table 3.2

Material	Film Thickness	T_{boil} (°K)	Ablated Thickness (microns)	Q''_{out}/Q''_{in}
$Li_{17}Pb_{83}$	1.0	1800	1.0	0.26
	0.1	1800	---	---
	0.1	1700	0.5	0.13
	1.0	1700	1.5	0.39
Li	1.0	1673	---	---
	0.1	1673	---	---

1 to 1.5 microns of material are ablated from the tube surface. This is due to two factors: the high thermal conductivity of the material and the time-broadening of the incident energy by the absorption and subsequent re-radiation in the cavity gas. The heat flux ratio indicates the proportion of incident energy which the ablated material has gained by both sensible and latent means; this represents a transport of energy back to the gas. Calculations were also made for Li films. These calculations indicated no material was ablated. A model limitation required complete mesh ablation; this has been subsequently modified with a partial mesh ablation model. Results are also presented for varying boiling temperatures for the LiPb and for two film thicknesses. The calculation modeled the multi-regions from the surface to the tube centerline using a fully implicit numerical scheme, due to time step accuracy requirements of a Crank-Nicholson technique. Table 3.3 contains the thermodynamic property values which were used in the calculations.

Table 3.3

	$Li_{17}Pb_{83}$	Li
k (MW/m°K)	3.5×10^{-5}	5×10^{-5}
ρC_p (MJ/m^2-°K)	1.703	2.11
ρ_{ifg} (MJ/m^3)	4.35×10^4	1.07×10^4
T_{boil} (°K)	1700-1800	1673

3.3.2 Phase II

This phase considers the propagation of the pulse through the tube bank until it thermalizes due to wake interactions. The hydrodynamics of supersonic flow over multi-bluff bodies coupled to the combined radiation and forced convection heat transfer results is a rather forbidding problem. The present work will detail the problem initial conditions and will discuss approximations made to obtain the current model.

3.3.2.1 Pulse Shape. Figure 3.4 shows a plot of the plasma mass density from the MFFIRE code as the pulse propagates outward and is reflected at 7 m. At the 5 m radius (the location of the first tube bank), the pulse width is essentially 100 cm. For the purpose of the present modeling effort, a representative square wave pulse with parameters given in Table 3.4 was created. In the table, γ is the ratio of specific heats and T_0 is the stagnation temperature (the temperature the fluid would have if it isentropically slowed to zero velocity). The partitioning of the energy between sensible and kinetic components is also given; 88% of the energy is kinetic. The Reynolds

Table 3.4. Gas Pulse Initial Conditions

T (°K)		3000
P (N/cm^2)		2.23
ρ (g/cm^3)		3.6×10^{-5}
u (cm/s)		2.5×10^5
M_∞		2.5
T_o (°K)		8975
Re_d		2.1×10^4
Pulse width (cm)		100
γ		1.667
C_p (J/g-°K)		0.523
Gas Energy	sensible	2.6
	kinetic	19.5

number (Re_d) is based on the diameter of the first tube (taken to be 3 cm). A simple power fit of the viscosity[3] and thermal conductivity[4] data for the temperature range of interest was used in the present model. The gas was assumed to be argon only.

3.3.2.2 Fluid Characteristics. As indicated in Table 3.4, the gas pulse has very high kinetic and sensible energies; the question of whether continuum fluid mechanics or rarefied gas modeling is to be used to model the pulse must be addressed. Two Knudsen numbers (λ/L), ratio of the mean free path in the fluid to a characteristic length, were calculated. The mfp was calculated

from $\lambda = \frac{\mu}{\rho}\left(\frac{\pi}{2RT}\right)^{1/2}$, assuming thermal equilibrium.[5] The first Kn was simply determined using the tube diameter as the characteristic length: $Kn_d = 1.8 \times 10^{-4}$. The second was determined using the bow shock standoff distance as the characteristic length (from Refs. 5 and 6). This Kn was 2.5×10^{-4} (the steady-state standoff distance was 0.55 cm). Both of these Knudsen numbers justify the use of continuum mechanics. This result was corroborated in Ref. 7.

3.3.2.3 Pulse-Body Interaction. The problem of supersonic pulse impingement on a bluff body (multi-bodies) has not been extensively researched; little practical applications outside of weapons blast effects exist. Glenn[8] used a one-dimensional wave code to model flow in a variable cross-section duct; he essentially used an inviscid flow model. The effects of choking due to combined viscous, heat transfer, and area changes could not be adequately modeled. This requires a fully time dependent two-dimensional Navier-Stokes computer code capable of handling shocks and both convective and radiative heat transfer to multi-surfaces.

A simplification to the problem is to consider it to be an impulse flow situation. That is, the fluid is assumed to instantaneously interact with the entire body at time 0+. This does not account for the initial developing boundary layer as the pulse propagates around the body. If we define a nondimensional time $t^* = t(u/a)$ where u is the free stream velocity and a is the body radius, then White[10] predicts a steady state boundary layer region to exist at $t^* = 1.6$. Deffenbaugh[9] predicts this value to be approximately 5. A steady state was assumed when the separation point has reached its equilibrium position. The modeled pulse of width 100 cm takes a nondimensional

time of 66 to propagate past the tube. Therefore, the boundary layer can be assumed to be fully developed and the skin friction a constant.

The Reynolds number of the pulse is such that a von Karman vortex wake would be expected;[11] the wake region starts to shed vortices at $t^* = 15$.[9] Thus, the flow field about the tube will be fully developed for approximately 75% of the pulse propagation time. Unfortunately, all the published data and numerical investigations have been for subsonic flow; the effects of the supersonic flow are not known. Also, the analysis to date has been for a single tube and not a tube bank where the shedding vortices from the upstream bodies create a real modeling mess.

3.3.2.4 Stagnation Heat Flux. The heat transfer rate at the stagnation point is the highest the body will experience. We now consider the first tube row, with diameter taken to be 3 cm. The stagnation flux has two components: a convection component due to the high speed flow and a radiation component. The stagnation temperature (8975°K) was used for radiation heat transfer. The convective flux was determined to be 1.11 kW/cm^2 and the radiative one to be 6.3 kW/cm^2 for a total heat load of 7.41 kW/cm^2. This compares to the fireball flux of greater than 140 kW/cm^2 (for a very short period). This heat load represents the flux to the surface of the film. Any ablation of the film will tend to reduce the radiative component.

3.3.2.5 Interference. As stated earlier, a wake region will quickly form and be convected downstream. This presents a problem of flow interference between the bodies. Extensive literature exists for the subsonic case,[12] but no one appears to design supersonic cross-flow heat exchangers. Using this subsonic data as a guide, a pitch to diameter ratio of 3 for the first two tube rows would allow them to behave almost independently for the tube impulse calcu-

lations. However, it must be stressed that the interference between bow shocks from neighboring tubes has not been considered. This effect would reduce the impulse experienced at the second tube row since the bow shocks increase the effective diameter of the body for drag calculations. Therefore, more energy of the pulse will be extracted at the first tube row.

3.3.2.6 Model. The current modeling approach uses a control volume analysis since detailed fluid mechanics would require an inordinate amount of computer resources, even if available.[13] Eleven volumes were used; the first represents the initial small tube rows (3 cm diameter) and the remaining represents a 10 cm diameter tube row (radial orientation). Standard conservation of mass, momentum, and energy equations were used to advance the pulse from one volume to the next. The equations allowed for compressibility effects; the flow was allowed to shock and choke down to satisfy the Second Law of Thermodynamics. An ideal gas equation of state was used for the gas. A modified Hottel long furnace approximation[14] for the gas radiation heat transfer allowed the problem to be cast as a simple marching formulation, i.e., the radiation heat transfer in one volume is not influenced by the adjacent volumes. This is similar to the parabolic formulation of the boundary layer equations in fluid mechanics.

The energy exchange between the gas and surface has two components: a nonlinear radiation term and a quasi-linear convection term. The forced convection heat transfer coefficient, obtained from Ref. 15, is given as:

$$h = C_1 \, Re^{0.556} \, Pr^{0.333} \, (k/d) \; .$$

C_1 is a function of the number of tube rows from the initial pulse contact. Essentially, this is the wake influence on the heat transfer.

There are two problem areas for the radiation heat transfer term: the effective gas emissivity and the gas temperature. The gas emissivity depends on the degree of ionization and amount of material ablated or entrained from the film. The present calculation used 1.0 and 0.01. Howell[16] suggests that the gas will be very transparent for radiation exchange and a value of 0.01 would be more appropriate. The second question concerns the appropriate gas temperature to use. A large temperature gradient exists from the tube surface to the freestream; the temperature is close to its stagnation value in the boundary layer but decreases as the velocity increases. Only extremely simple situations lend themselves to analytic solutions.[17] In lieu of numerically solving the integro-differential equations for this problem, it is hoped that the low gas emissivity will reduce the effect of using a single gas temperature value, the Eckert reference temperature.

The fluid drag was represented by a drag coefficient accounting for both skin friction and form drag. Steady state correlations were used (recall the earlier discussion on characteristic times). The following piecewise correlation was used:

$M < 0.4$	$C_d = 1 + 10/Re^{0.666}$	(Ref. 10)
$0.4 < M < 2$	$C_d = 0.1875\ M + 0.925$	(Ref. 18)
$M > 2$	$C_d = 1.5$	

In summary, the current model assumes local (intra-volume) steady state, but determines the time varying combined fluid dynamic and heat transfer interactions as the pulse propagates through the tube bundle.

3.3.2.7 Model Results. Three calculations using this model are presented. The first, case A, assumes a HIBALL tube geometry and gas emissivity of 1.0. Case B uses a theoretical tube spacing such that the flow will not choke as it propagates through the tube bank. The last calculation represents case A conditions but with a gas emissivity of 0.01. All of these calculations use a surface emissivity of 0.15.[20] Figure 3.7 compares local temperature and stagnation temperatures for the calculations. Figure 3.7a indicates that the local temperature is quite different for the two calculations. The flow in case A shocked down and choked due to the area change and dominance of drag over heat transfer.[19] However, it is interesting to note that the temperatures converge at higher mesh numbers. The initial increase in the temperature in case B is due to the change of the characteristic tube in the mesh from 3 cm to 10 cm. Figure 3.7b shows the preferred plot variable, the stagnation temperature. Here we see that increasing the tube spacing reduces the gas transit time and results in a higher outlet temperature. Therefore, choking is preferred to lower the gas temperature. The final plot, Fig. 3.7c, illustrates the effect of gas emissivity. The radiation heat transfer component is reduced for the 0.01 case. The gas energy was reduced to 55% of its initial value for the first pass through the tube bank. The transit time was about 1 msec; therefore, plenty of time is available for further heat transfer to reduce the gas temperature (Phase III).

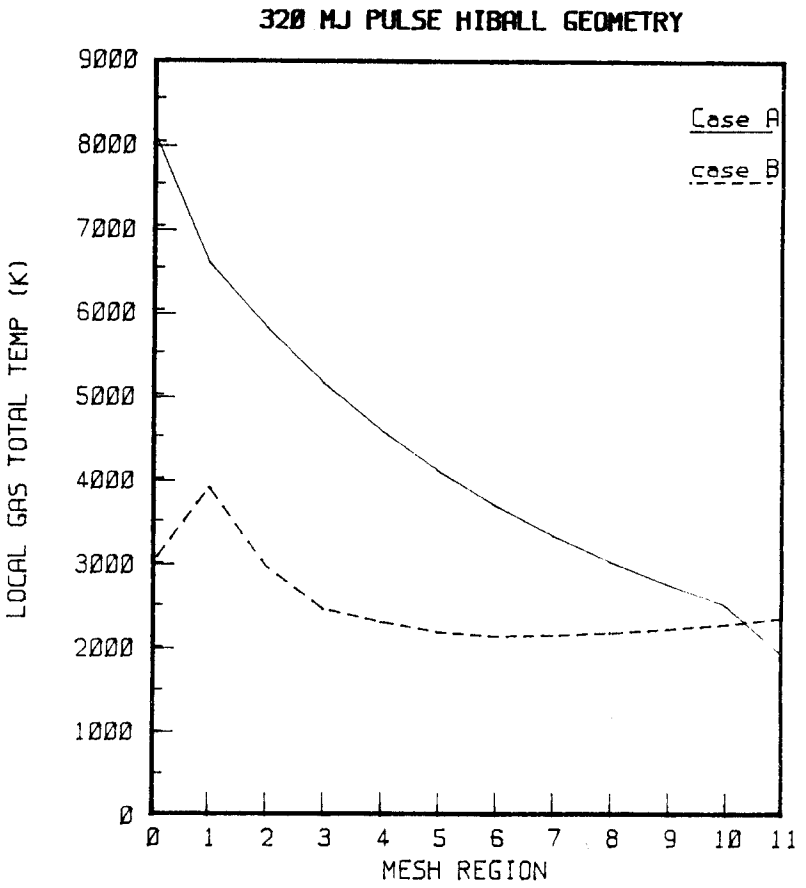

Fig. 3.7a. Gas temperature in array of tubes.

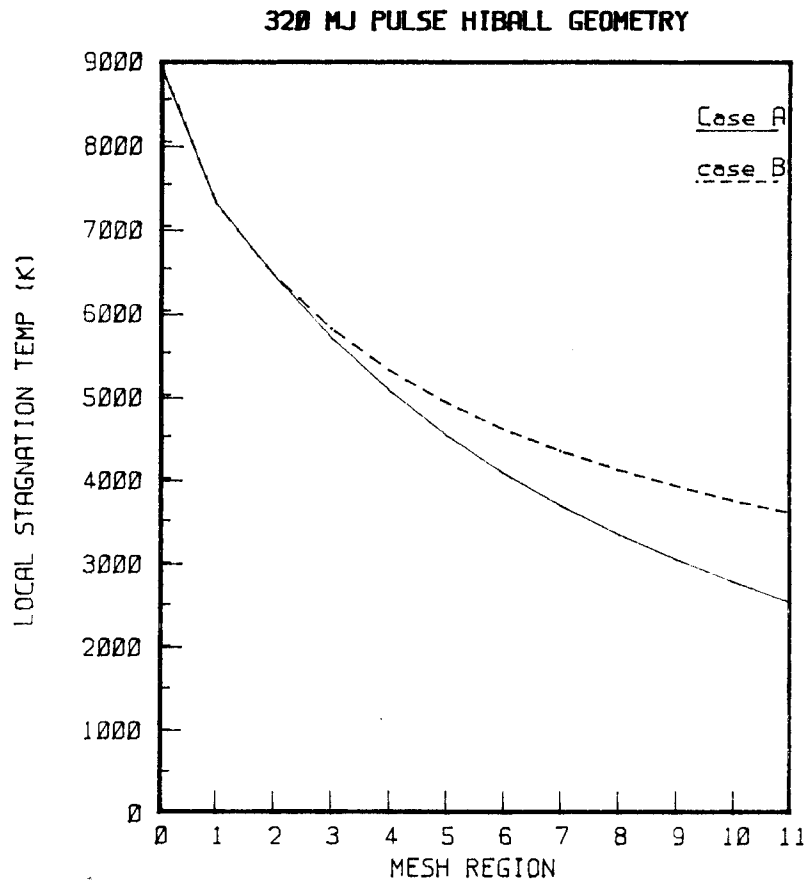

Fig. 3.7b. Stagnation temperature in array of tubes.

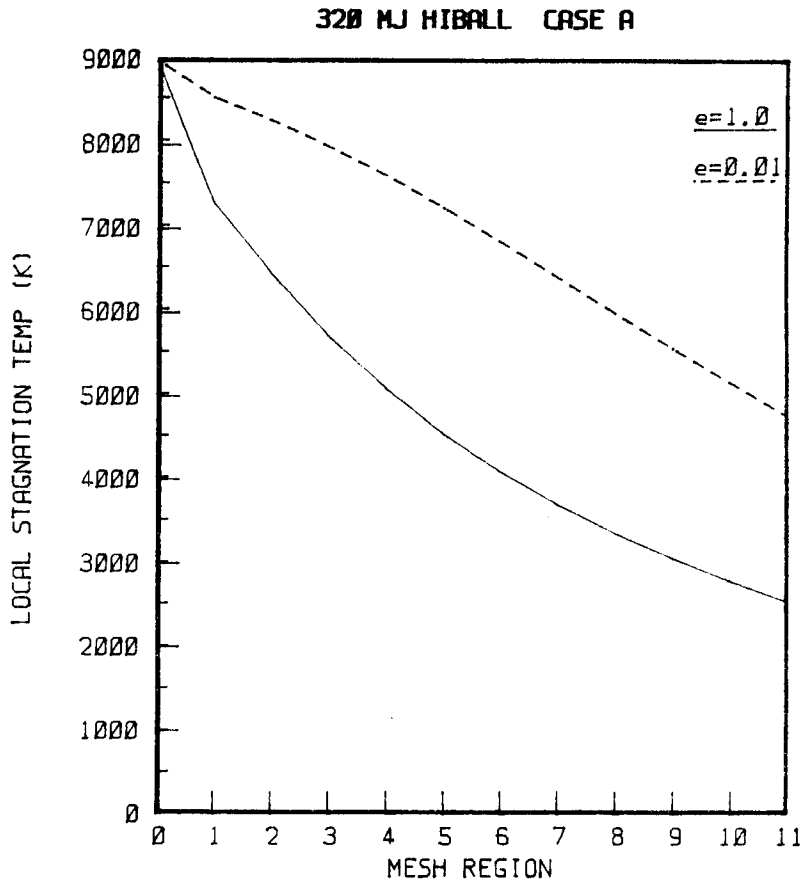

Fig. 3.7c. Stagnation temperature in array of tubes for emissivities of 1.0 and 0.01.

3.3.3 Phase III

This phase considers only radiation heat transfer between the thermalized gas and the tube surfaces. The very large tube surface area (15100 m^2) compensates for the reduced gas emissivity. A simple volumetric rate equation equating the change in gas internal energy to the radiation heat transfer was used to estimate the time required to reduce the gas temperature to a stagnation temperature of 800°K. This can be expressed simply as:

$$mC_v \frac{dT}{dt} = FA\varepsilon\sigma(T^4 - T_{surf}^4) .$$

If a shape factor of 0.8 is assumed and an emissivity of 1.0 used, it takes 0.026 seconds to reduce the temperature from 9000 to 800°K. However, we note that the emissivity will be lower, but the initial temperature will also be lower. Also, the calculation does not include the areas of the end of the reactor cavity or the effects of film vaporization.

3.3.4 Future Work

(1) The one-dimensional conduction model with ablation will be coupled to the gas model at each mesh to obtain a better surface temperature calculation (and any ablation).

(2) Radiation exchange between volumes will be allowed -- thus coupling the calculation procedure.

(3) The reflection of the pulse back into the tube bundle will be determined.

(4) A 2-D wave code (CSQ from Sandia) will be used to obtain approximate impingement loads on the first row of tubes.

3.4 Coupled Fireball - INPORT Tube Code Development

The behavior of the explosion induced fireball and the heat transfer and vaporization are discussed earlier in this report, where the fireball has been assumed to be unaffected by the vaporization of liquid metal from the tubes. This is not always a good approximation. The addition of vapor to the gas may drastically change the radiative properties of the gas near the vaporizing surface by changing the density, temperature and species mix of the gas. This may form a vapor shield which can reduce the heat flux to the film and reduce the vaporization. Because of this coupled nature of the radiation transport and the vaporization and because recondensation may play a role, a self-consistent treatment of the two processes is needed.

The code CONRAD[21] has been improved to do this self-consistent modeling. The same method that was used to obtain the results in Section 3.4 has been used in CONRAD. The radiation transport hydrodynamics code MFFIRE has been modified to perform a simulation of the fireball phenomena. Both of these parts of CONRAD have been tested independently, though the assembled code has not yet been fully tested. Testing of the code is currently underway.

This new version of CONRAD has several advantages over the old version,[21] which also treated the film and the gas self-consistently. CONRAD now has multigroup radiation transport; it did not before. The model for the heat transport and vaporization in the tubes is much more general and better treats the physics of non-equilibrium vaporization, which is the situation in many cases of interest. Also, the hydrodynamics section of CONRAD can now rezone itself during a calculation. This last feature is important when mass transfer between the gas and the film on the tubes becomes large

because the hydrodynamics uses a Lagrangian finite differencing method. Such methods work best when adjacent zones have roughly equal masses. The rezoning scheme used in CONRAD preserves the ratios between masses of adjacent zones.

These improvements make CONRAD a more versatile code and make it more accurate. The improved methods of radiative heat transfer and heat transfer and vaporization on the tubes are most significant and should help alleviate the energy conservation problems found in the older version of CONRAD. The rezoning feature improves the calculation for cases with large mass transfer.

References for Chapter 3

1. B. Badger et al., "HIBALL - A Conceptual Heavy Ion Beam Driven Fusion Reactor Study," Kernforschungszentrum Karlsruhe Report KfK-3202, Volume 2, Chapter VI (1981).

2. G.A. Moses, T.J. McCarville and R.R. Peterson, "Documentation for MFFIRE, A Multifrequency Radiative Transfer Version of FIRE," University of Wisconsin Fusion Engineering Program Report UWFDM-458 (March 1982).

3. W. Ibele, "Thermophysical Properties," in Handbook of Heat Transfer, Rohsenow and Harnett (eds.), (1973).

4. Thermophysical Properties of High Temperature Solid Materials, Y.S. Touloukian, editor, Thermophysical Properties Research Center, Purdue University.

5. W.H. Giedt and D.R. Willis, "Rarefied Gases," in Handbook of Heat Transfer, Rohsenow and Harnett (eds.), (1973).

6. "Equations, Tables and Charts for Compressible Flow," NACA-1135.

7. S.F. Hoerner, Fluid-Dynamic Drag, (1958).

8. L.A. Glenn, "Divergent Impulsive Crossflow Over Packed Columnar Arrays," preprint UCRL-83051, July 1979.

9. F.D. Deffenbaugh and F.J. Marshall, "Time Development of the Flow About an Impulsively Started Cylinder," AIAA Journal 14 (No. 7), 908-913 (1976).

10. F.W. White, Viscous Fluid Flow, McGraw-Hill (1974).

11. L.E. Ericsson and J.P. Reding, "Criterion for Vortex Periodicity in Cylinder Wakes," AIAA Journal Technical Note 17 (No. 9) 1012-1013.

12. M.M. Zdravkovich, "Review of Flow Interference Between Two Circular Cylinders in Various Arrangements," ASME Journal of Fluids Engineering, 618-633 (Dec. 1977).

13. D.R. Chapman, "Computational Aerodynamics Development and Outlook," AIAA Journal 17 (No. 12) (Dec. 1979).

14. H.C. Hottel and A.F. Sarafim, Radiative Transfer (1967).

15. J.P. Holman, Heat Transfer, (1972).

16. John R. Howell, private communication.

17. R. Siegel and J.R. Howell, Thermal Radiation Heat Transfer, McGraw-Hill (1972).

18. J.A. Roberson and C.T. Crowe, Engineering Fluid Mechanics.

19. A.H. Shapiro, The Dynamics and Thermodynamics of Compressible Fluid Flow, John Wiley and Sons (1953).

20. M.L. Corradini, private communication.

21. B. Badger et al., "Annual Report of Research Performed on the HIBALL Project Between 1 January and 31 December 1982 by Fusion Power Associates," FPA-82-6.

4. PLASMA CHANNEL MHD CODE DEVELOPMENT

An important facet of the problem of ion propagation in preformed channels is the initial formation of a high quality channel. The channel is formed in two stages: (1) a laser beam is focussed into the cavity gas, exciting seed atoms to higher energy states, and (2) a capacitor is discharged along this path of excited atoms causing a breakdown with the subsequent current forming a Z-pinch plasma configuration. These processes will determine, in part, the characteristics of the cavity gas such as density and temperature. In 1982, it was proposed that the Z-pinch channel formation be studied with a modified version of the radiation hydrodynamics code, MF-FIRE. The modification would include magnetic field and external circuit equations. The task of modifying MF-FIRE was split into two parts: develop a code that solves the magnetic field and external circuit equations, then couple that code into MF-FIRE. The first part of the task has been accomplished. The result, a code called MAGDIF, solves a one-dimensional magnetic diffusion equation self-consistently with a circuit equation. The MAGDIF code has been verified for a number of problems with known solutions. The coupling of MAGDIF to MF-FIRE is currently underway.

4.1 FIRE and MAGDIF: Design Philosophy

MF-FIRE is a one-dimensional Lagrangian hydrodynamics code that uses a one-fluid plasma model.[1] The plasma is coupled to the radiation field which is treated with either single group or multigroup diffusion theory. The magnetic diffusion model chosen for the magnetic field calculation provides both physical and computational consistency with the models used in MF-FIRE. The validity of the magnetic diffusion model rests upon the assumption that the displacement current in Ampere's Law is small in comparison to the current

density. The validity of the diffusion equations used in MF-FIRE rests upon assumptions of the same nature - thermodynamic equilibrium is not too far away and the spatial and temporal variation of the medium is relatively gentle. From the computational viewpoint, the magnetic diffusion equation differs little from the diffusion equations solved in MF-FIRE. The numerical treatment of each of these equations is practically identical.

MF-FIRE was written according to the principles of structured programming and design. These same principles were followed closely in MAGDIF. These principles insure that the code is easy to debug and modify, particularly for users who were not involved in the development of the code. Ease of modification is important since during the lifetime of the code, it is likely that certain physical models may be found to be inappropriate. Two specific examples of this are important in MAGDIF: the electrical resistivity and the form of Ohm's Law. Presently, the electrical resistivity is calculated from the classical transport result

$$\eta(r,t) = \frac{4\sqrt{2\pi}}{3} \frac{Z^2 e^2 \sqrt{m_e}\, n}{T^{3/2}} \log \Lambda \qquad (4.1)$$

and the form of Ohm's Law used is

$$\eta \vec{J} = \vec{E} + \frac{1}{c} \vec{u} \times \vec{B} \,, \qquad (4.2)$$

where $\vec{u}$ is the fluid flow velocity. Since anomalous transport is often an important effect, it may be necessary to change the electrical resistivity calculation: structured design insures that this modification will be relatively easy to make and will require that only that portion of the code

directly related to the resistivity calculation be altered. The form of Ohm's Law used here is relatively simple. It may be found that such things as the thermoelectric effect are important. Since the form of the magnetic diffusion equation depends on the form of Ohm's Law, as will be seen later, a modification in the latter could require extensive changes in the code. However, adherence to structured design principles insures that modifications will be isolated to, say, a single subroutine.

4.2 Description of MAGDIF

4.2.1 Formulation of the Problem

The MAGDIF code closely follows the description of the MAGPIE code[2] developed by R. Kidder many years ago. The magnetic diffusion equation used in MAGDIF is a combination of Ampere's Law,

$$\vec{\nabla} \times \vec{B} = \frac{4\pi}{c} \vec{J} + \frac{1}{c} \frac{\partial \vec{E}}{\partial t} \tag{4.3}$$

with the displacement current set to zero; Ohm's Law

$$\eta \vec{J} = \vec{E} + \frac{1}{c} \vec{u} \times \vec{B} \; ; \tag{4.4}$$

and Faraday's Law

$$\vec{\nabla} \times \vec{E} = - \frac{1}{c} \frac{\partial \vec{B}}{\partial t} \; . \tag{4.5}$$

One eliminates $\vec{J}$ from Eq. (4.4) using (4.3), takes the curl of the resulting equation, then eliminates $\vec{\nabla} \times \vec{E}$ from that equation using (4.5). The result is

$$\frac{1}{c} \frac{\partial \vec{B}}{\partial t} + \vec{\nabla} \times \left(\frac{\eta c}{4\pi}\right) \vec{\nabla} \times \vec{B} = \vec{\nabla} \times \frac{\vec{u}}{c} \times \vec{B} \; . \tag{4.6}$$

Assuming that $\vec{B}(r,\theta,Z) = \hat{\theta}\, B(r)$ and $\vec{u}(r,\theta,Z) = \hat{r}\, u(r)$, this equation becomes

$$\frac{\partial B}{\partial t} - \frac{\partial}{\partial r}\frac{1}{r}\left(\frac{\eta(r)c^2}{4\pi}\right)\frac{\partial}{\partial r} rB = -\frac{\partial}{\partial r} u\, B. \qquad (4.7a)$$

The initial condition is arbitrary (user-specified),

$$B(r,0) = B_0(r), \qquad (4.7b)$$

while the boundary conditions are obtained from the integral form of Ampere's Law:

$$B(0,t) = 0,$$
$$B(a,t) = \frac{2\, I(t)}{ac}, \qquad (4.7c)$$

where a is the channel radius and I is the current flowing in the channel. Until coupled into MF-FIRE, the fluid flow velocity $\vec{u}$ set to zero. Thus, MAGDIF solves for the magnetic field profile in cylindrical geometry under the assumptions of azimuthal and axial symmetry in a rigid medium characterized by a radially varying electrical resistivity. The field profile depends on the current which may be either a user-specified function of time or driven by a user-specified external circuit. In the latter option, the current is calculated in an approximately self-consistent way to be described below.

4.2.2 Solution of the Problem

The performance of MAGDIF in solving the problem may be evaluated in a number of ways. Three conservation relations -- conservation of current, mag-

netic flux, and energy -- must be satisfied before the results of the code may be accepted. These conservation relations are independent of whether the current is user-specified or is driven by an external circuit. MAGDIF's performance relative to these conservation relations will be discussed below. When certain restrictions are placed on the problem, it is possible to obtain an analytic solution to the magnetic diffusion equation with which numerical results may be compared.

4.2.2.1 Comparison with an Analytic Solution. The analytic solution to Eq. (4.7a) for a rigid medium has been obtained. For this solution, it was assumed that the electrical resistivity was of the form

$$\eta(r,t) = \eta_0 \left(\frac{r}{a}\right)^n , \tag{4.8}$$

where n was allowed to lie in the range $-\infty < n < 1$. n could not be allowed to equal or exceed 1 since then the current density,

$$J = E/\eta$$

would not be integrable at r = 0, which is a nonphysical result and would require a different boundary condition on the axis than is given by Eq. (4.7c). The solution was found by assuming that for constant current, the solution had the form

$$B(r,t) = \phi(r) + \psi(r,t) . \tag{4.9}$$

Using the solution to the constant current problem along with Duhamel's superposition principle, the solution to the problem with time-dependent boundary data,

$$B(a,t) = \frac{2}{ac} I(t) ,$$

was obtained. This solution is

$$B(r,t) = \int_0^t d\tau \left[\frac{2I(\tau)}{ac}\right]\left[2\left(\frac{r}{a}\right)^{-n/2} \sum_{m=1}^{\infty} J_m^n \left(\frac{r}{a}\right) \mu_{m,n}^2 e^{-\mu_{m,n}^2 (t-\tau)}\right] , \quad (4.10a)$$

where $$J_m^n(x) \equiv J_1\left(\nu_m x^{(2-n)/2}\right) / \nu_m J_2(\nu_m) , \quad (4.10b)$$

and $$\mu_{m,n}^2 \equiv \left[\left(\frac{2-n}{2}\right)\nu_m\right]^2 \frac{\eta_o c^2}{4\pi a^2} .$$

ν_m is the m^{th} root of J_1, the Bessel function of the first kind of order 1. J_2 is the Bessel function of the first kind of order 2.

Despite the complicated form of the solution, it is readily seen that it does give the expected behavior for several simple examples. First, note that it indicates that the field scales with the current. Second, for constant current, the solution evolves to the steady state magnetic field profile

$$B(r,t=\infty) = \left(\frac{2I}{ac}\right)\left[2\left(\frac{r}{a}\right)^{-n/2} \sum_{m=1}^{\infty} J_m^n\left(\frac{r}{a}\right)\right] \quad (4.11a)$$

$$= \left(\frac{2I}{ac}\right)\left(\frac{r}{a}\right)^{1-n} . \quad (4.11b)$$

For extremely resistive media, $\eta_0 \to \infty$, Eq. (4.7a) indicates that the time rate of change of the field will be very large. Taking $\eta_0 \to \infty$ in (4.10a) causes the exponentials to have very short e-folding periods -- the B-field changes rapidly with time. For extremely conductive media, $\eta_0 \to 0$, (4.7a) shows that $\frac{\partial B}{\partial t}$ is very small. Taking $\eta_0 \to 0$ in (4.10a), the e-folding periods of the exponentials approach infinity so that the field profile changes very slowly in time. In this case, the field is said to be frozen into the medium.

Calculations for several different values of n and constant current were performed. Since several of the calculations of the analytic solution were performed on a small computer (Hewlett Packard HP 9845B) that did not have Bessel function software, it was necessary to find a sufficiently accurate approximation to $J_1(x)$. The approximation used was a matching of a sine wave of varying phase and amplitude to a truncated power series:

$$J_1(x) \simeq \begin{cases} A(x) \cos [\theta(x)] & x > 3 \\ \sum_{j=0}^{N} \frac{(-1)(x/2)^{2j+1}}{j!(j+1)!} & x \leq 3 \end{cases} . \qquad (4.12)$$

The appropriate amplitude and phase functions were obtained in Ref. 3. Equation (4.12) gave relative errors of less than $10^{-3}\%$ for values of x away from the roots of $J_1(x)$ and away from the transition region x = 3 for N = 4. Truncating the Fourier-Bessel series introduced another source of error in the analytic solution. However, this error could be made quite small. For example, for the parameters

n = 0 (constant resistivity)

N = 9 (ten terms in power series)

and retaining 200 terms in the Fourier-Bessel series, the relative error was under 1% for most of the range $0 < r < a$ in comparing the steady state solution in forms Eqs. (4.11a) and (4.11b). This was taken to be an acceptably small error.

Figures 4.1, 4.2 and 4.3 show a comparison between the analytic and numerical solutions for n = 0, -3, and 0.9, respectively. Each plot shows the magnetic field profiles, from right to left, at times of 10^{-2}, 10^{-1}, 1, and 10^{6} times the e-folding period of the fundamental mode of the analytic solution ($1/\mu_{1,n}^2$ from Eq. 4.10c). In each case, the channel radius was taken to be 1 cm and the electrical resistivity was taken to be 1.1111×10^{-13} s. These plots show that MAGDIF's numerical solution is in good agreement with the true solution. The most notable difference between the numerical and analytic solutions is that, in each case, the former consistently lies below the latter. The reason for this is in a trick used in the numerical solution.

The code actually solves a rearranged version of (4.7a) that is written as an equation for the variable rB(r,t). The boundary condition imposed on this new variable at the axis is a zero-gradient condition:

$$\frac{\partial}{\partial r}(rB) = 0 \text{ at } r = 0. \tag{4.13}$$

Viewed as a boundary condition on B, (4.13) is ambiguous. Unless B is forced to vanish at r = 0, the code gives the result that the B-field evolves to a 1/r profile: the code correctly solves the wrong problem. By forcing B to vanish on the axis, the desired problem is solved. It is the way in which

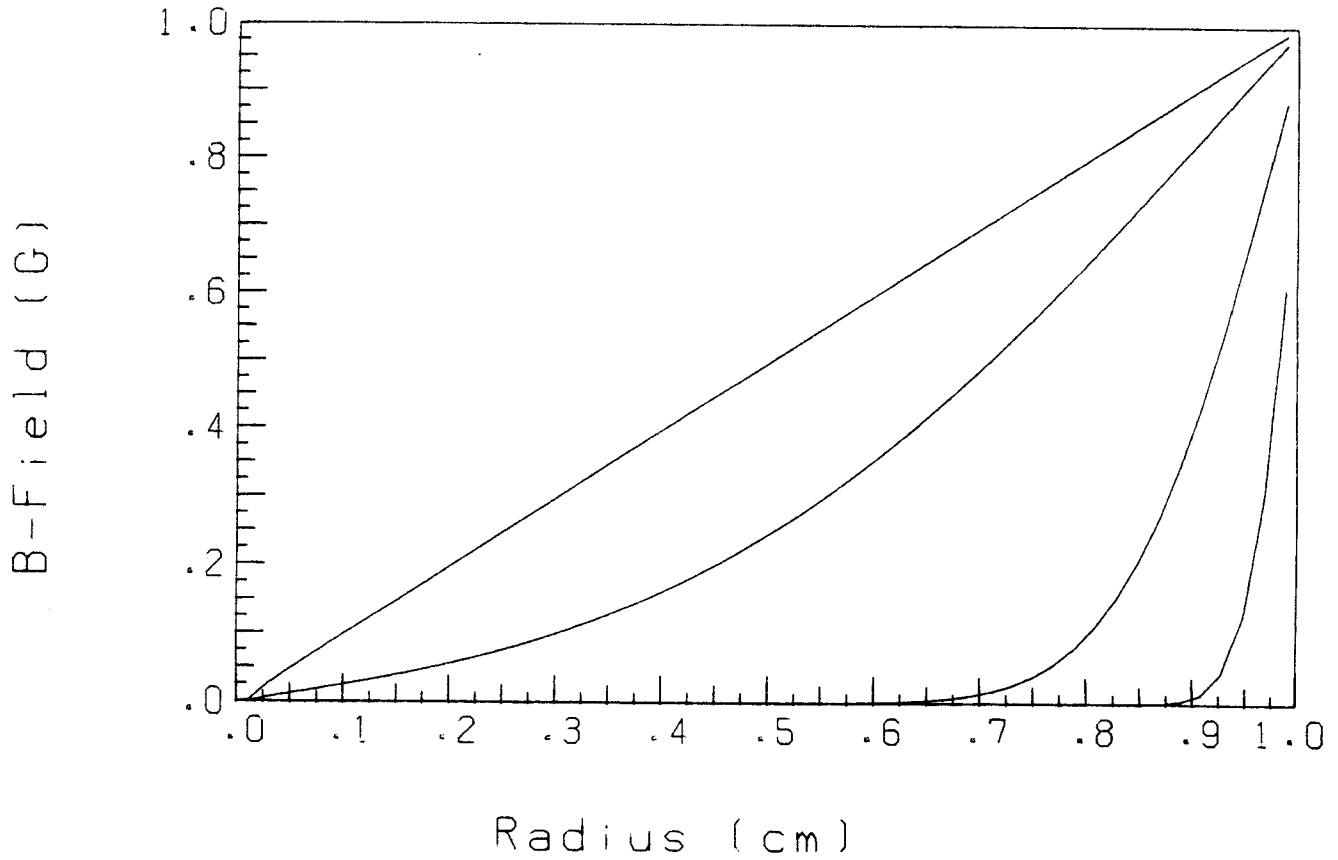

Fig. 4.1a. Magnetic diffusion: numerical solution.

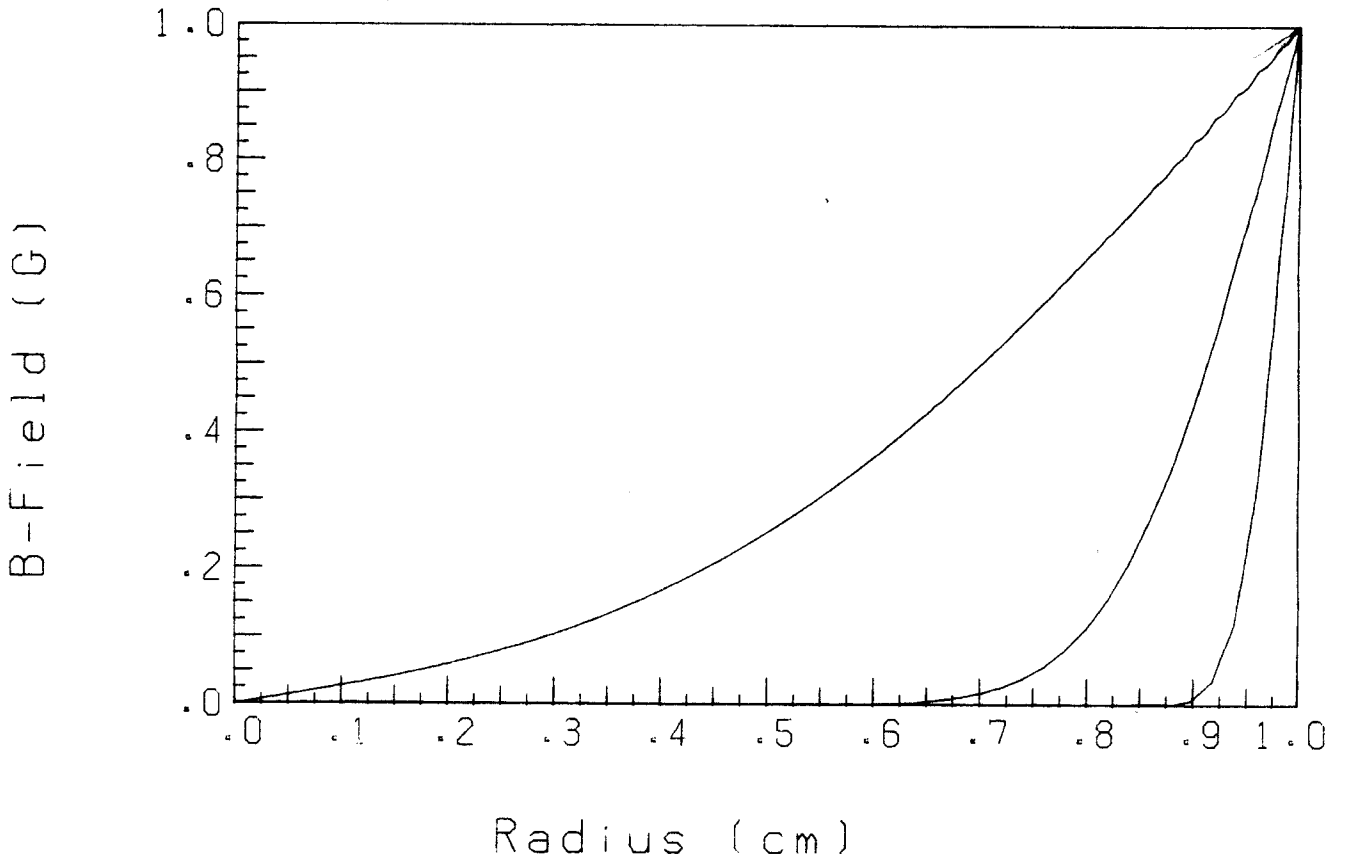

Fig. 4.1b. Magnetic diffusion: analytic solution.

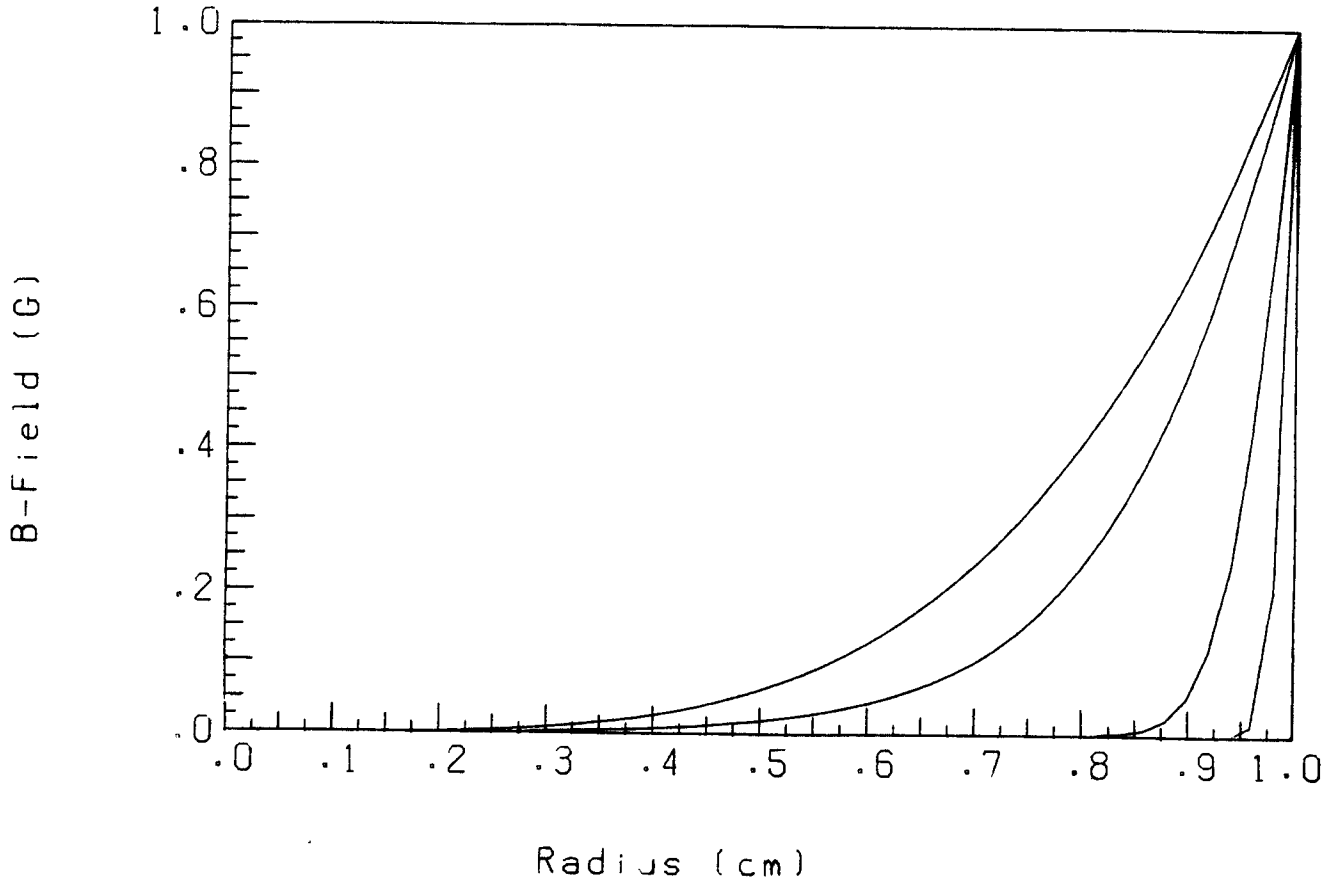

Fig. 4.2a. Magnetic diffusion: analytic solution for $D = r^{-3}$.

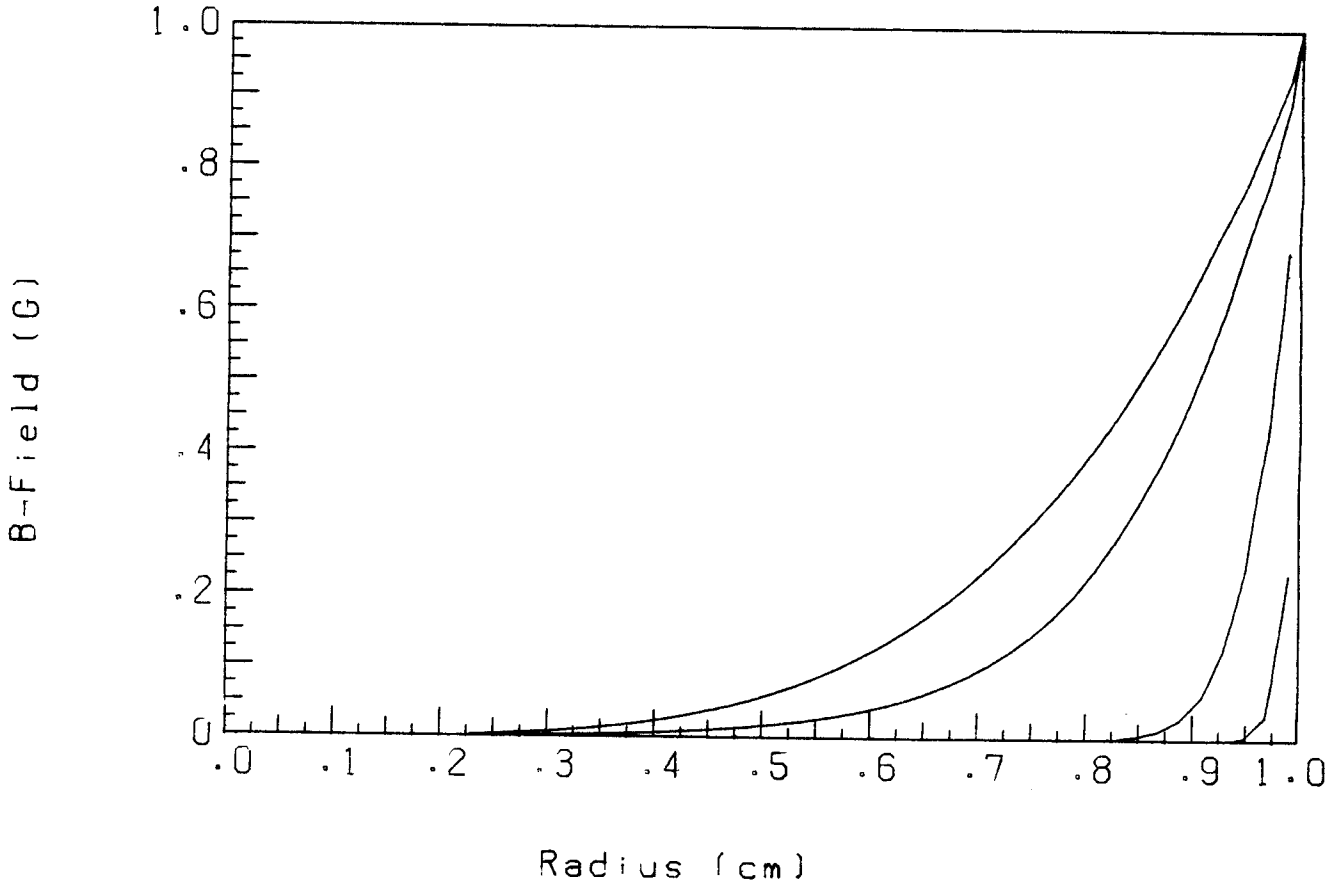

Fig. 4.2b. Magnetic diffusion: numerical solution for $D = r^{-3}$.

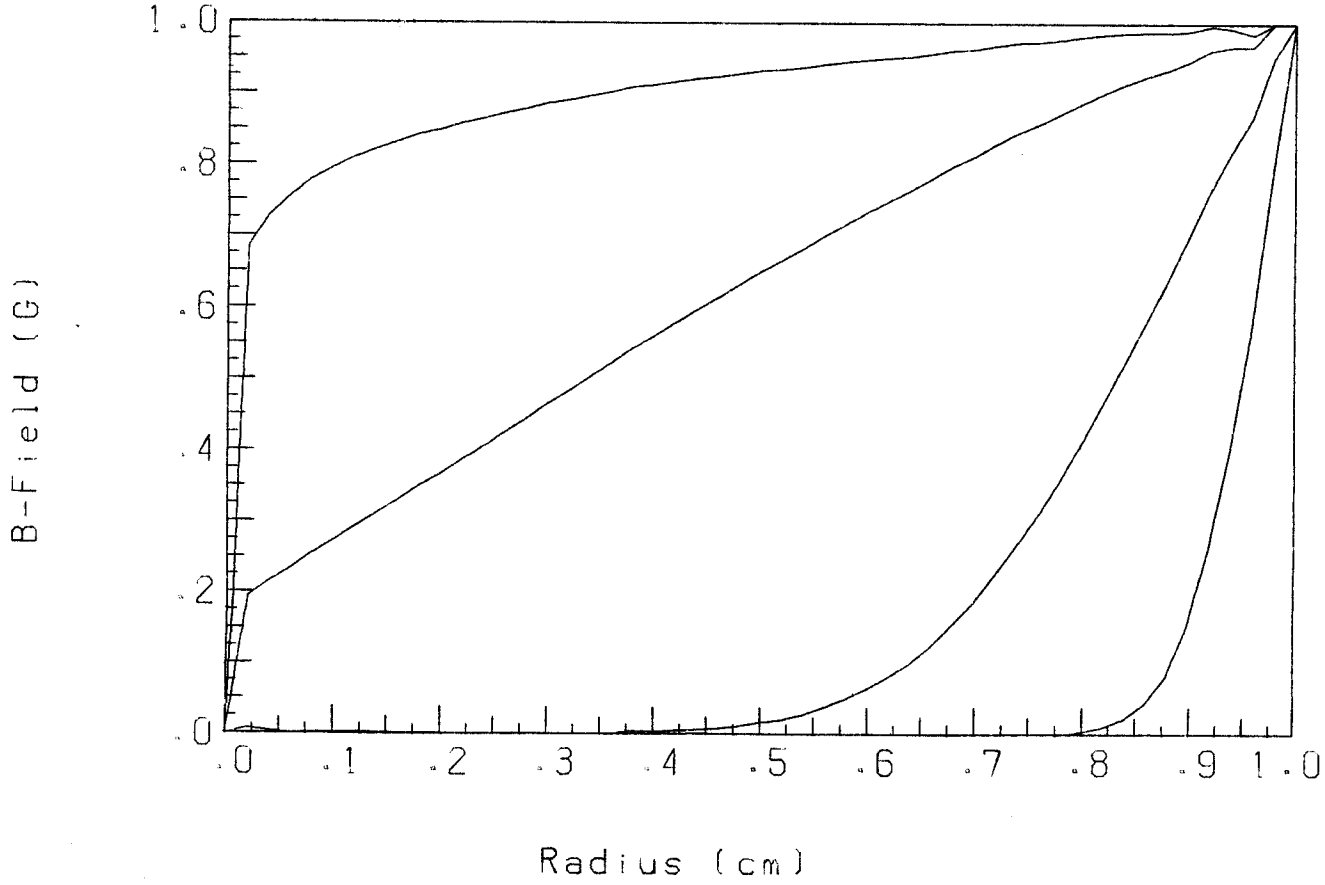

Fig. 4.3a. Magnetic diffusion: analytic solution for $D = r^{0.9}$.

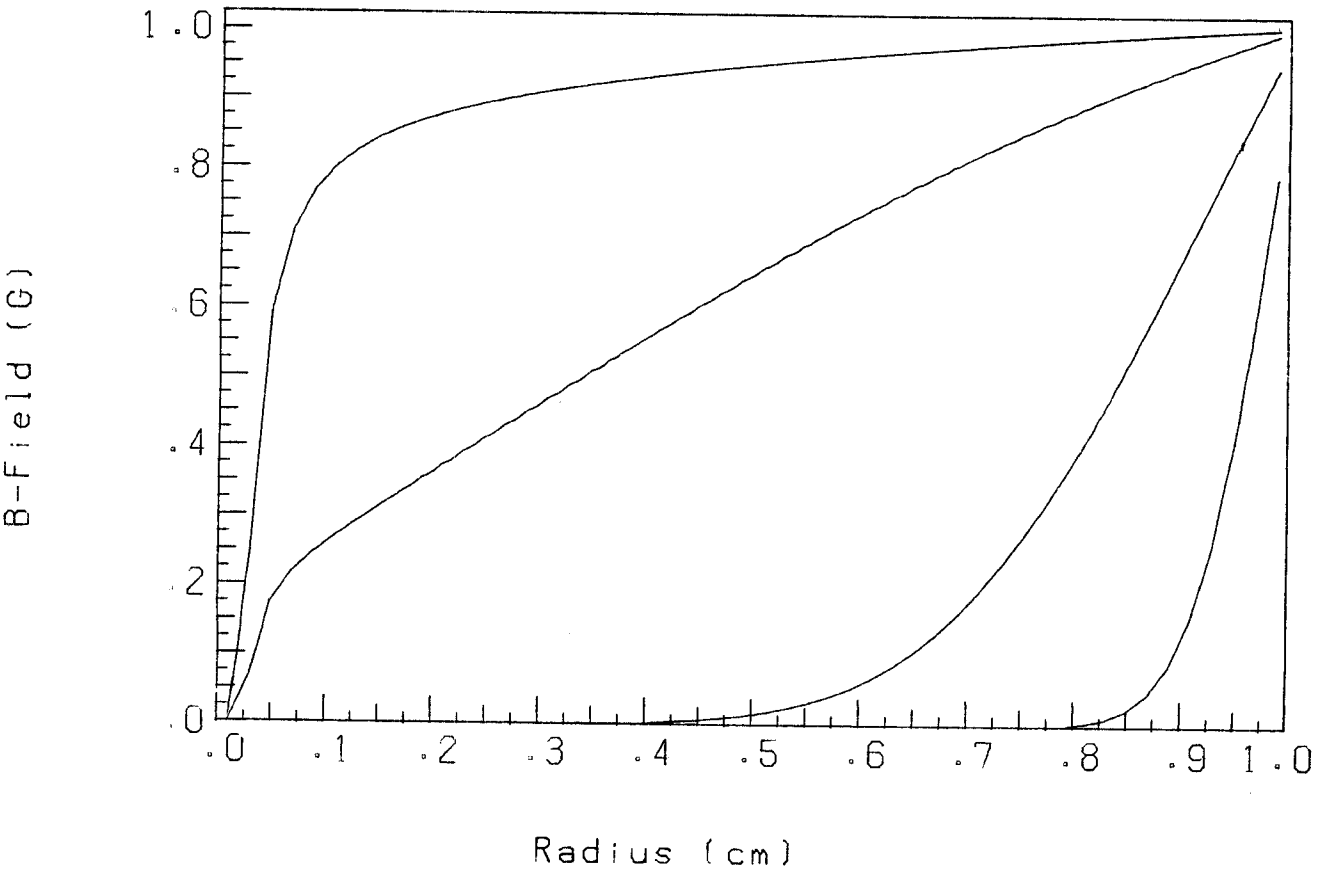

Fig. 4.3b. Magnetic diffusion: numerical solution for $D = r^{0.9}$.

this is done that causes the numerical solution to sag slightly but consistently below the true solution. In the code, the magnetic field is known only at the centers of the zones. The best that can be done in setting B to zero on the axis is to force B = 0 at r = $r_{1/2}$, where $r_{1/2}$ is the position of the center of the innermost zone. The effect of doing this is readily apparent in Figs. 4.1b and 4.3b. The algorithm sacrifices the innermost zone to resolve the ambiguity in the boundary condition (4.13).

The effect of this sacrifice is most apparent when comparing Figs. 4.3a and 4.3b. Here, the steady state field profile should vary as $r^{0.1}$. The code used 50 zones to solve the problem so that the field was forced to zero at r/a = 0.01. At this point, $(r/a)^{0.1} \cong 0.631$. The sacrifice of the inner zone causes the numerical solution to underestimate grossly the field near the axis. This error can be reduced in two ways: push the $r_{1/2}$ point as close as possible to the axis or use a larger number of zones. The second way is more economical than the first since, for the hydrodynamics calculations, the Courant criterion in the innermost zone often sets the most restrictive limit on the timestep. Decreasing the width of the inner zone could force the timestep to be unacceptably small.

Comparison of the three cases, n = -3, 0 and 0.9, shows that the error made in sacrificing the inner zone is most significant for channels with low resistivity on the axis. This could be of some importance in actual channel calculations. Real channels are likely to have a high temperature on the axis. Since classical resistivity varies as $T^{-3/2}$, the resistivity is likely to be low on the axis. This will be aggravated by the likelihood of the expansion of the innermost zone (zoning is Lagrangian) that would result in the $r_{1/2}$ point being pushed away from the axis. Thus, in realistic channel

problems, the code is likely to underestimate the magnetic field on the axis. This probably will not be a fatal flaw since the effect of the field in the center of the channel is not of great importance.

The results of a fourth calculation are shown in Fig. 4.4. This is the problem of a field decaying away from its steady state solution (constant resistivity) when the current is set to zero. The times of the plots are, from top to bottom, 10^{-3}, 10^{-2}, 10^{-1}, and 1 times the e-folding period of the fundamental mode past the time that the current is set to zero. Again, one may see that the numerical solution is quite close to the analytic solution, except near the axis. The field decays away to its fundamental mode: $B(r) \sim J_1(r/a)$.

4.2.2.2 The Current Equation. In deriving an equation governing the behavior of the current, the general procedure is to appeal to Kirchhoff's Law: the sum of voltage drops and sources around the circuit is zero. Each of the voltage drops and sources is then expressed as a function of time and current. For example, the voltage drop in the circuit for the case of the channel being driven by an RLC circuit with a voltage source is

$$0 = v_{ext} + v_{channel}$$

$$v_{ext} = v_o(t) - \frac{1}{C}\left[\int_o^t I(t)d\tau + Q_o\right] - IR - \dot{I}L \qquad (4.14)$$

where $v_o(t)$ = voltage source

C = capacitance in RLC driver

R = resistance in RLC driver

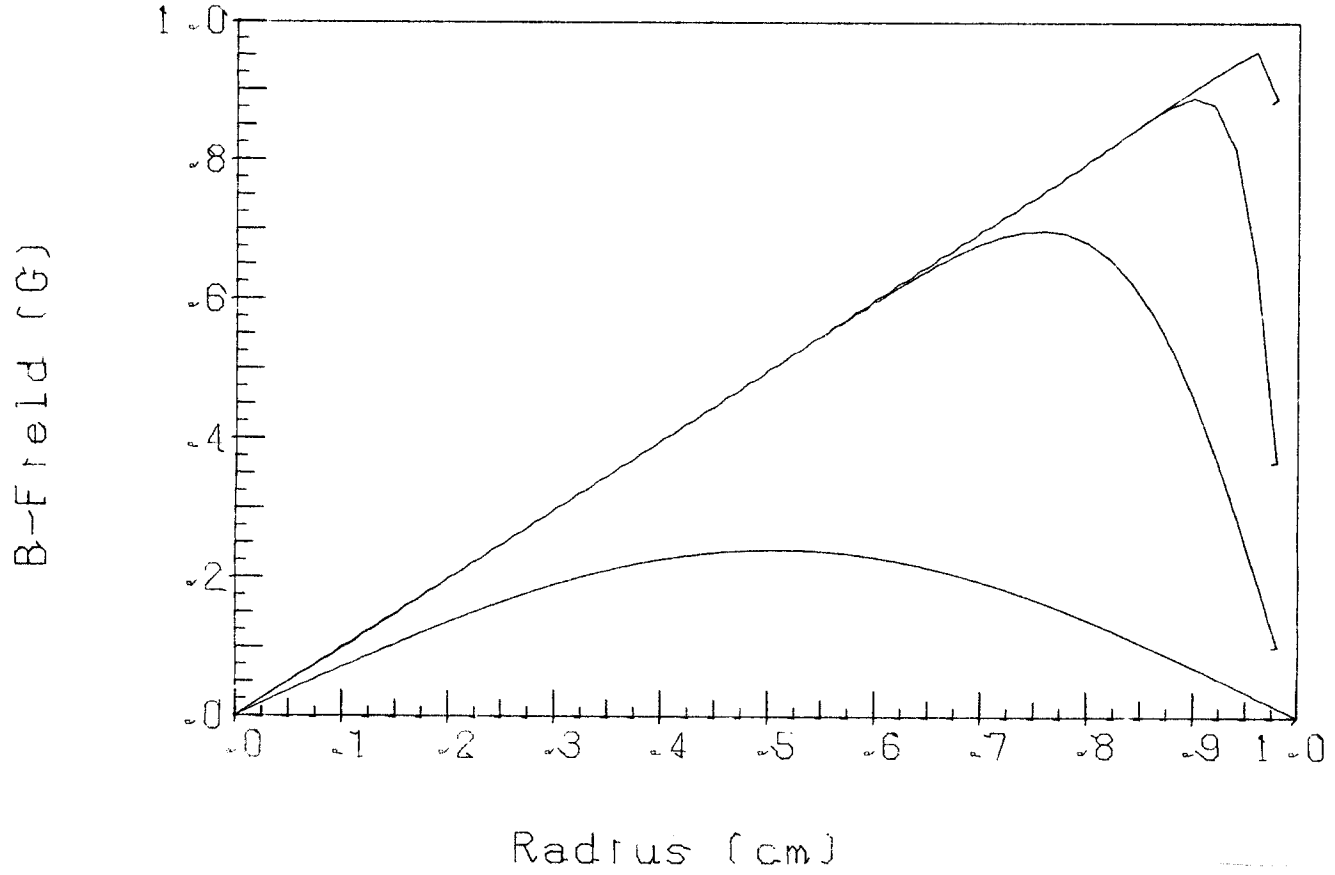

Fig. 4.4a. Magnetic diffusion: decaying field for D = 1 (anal;

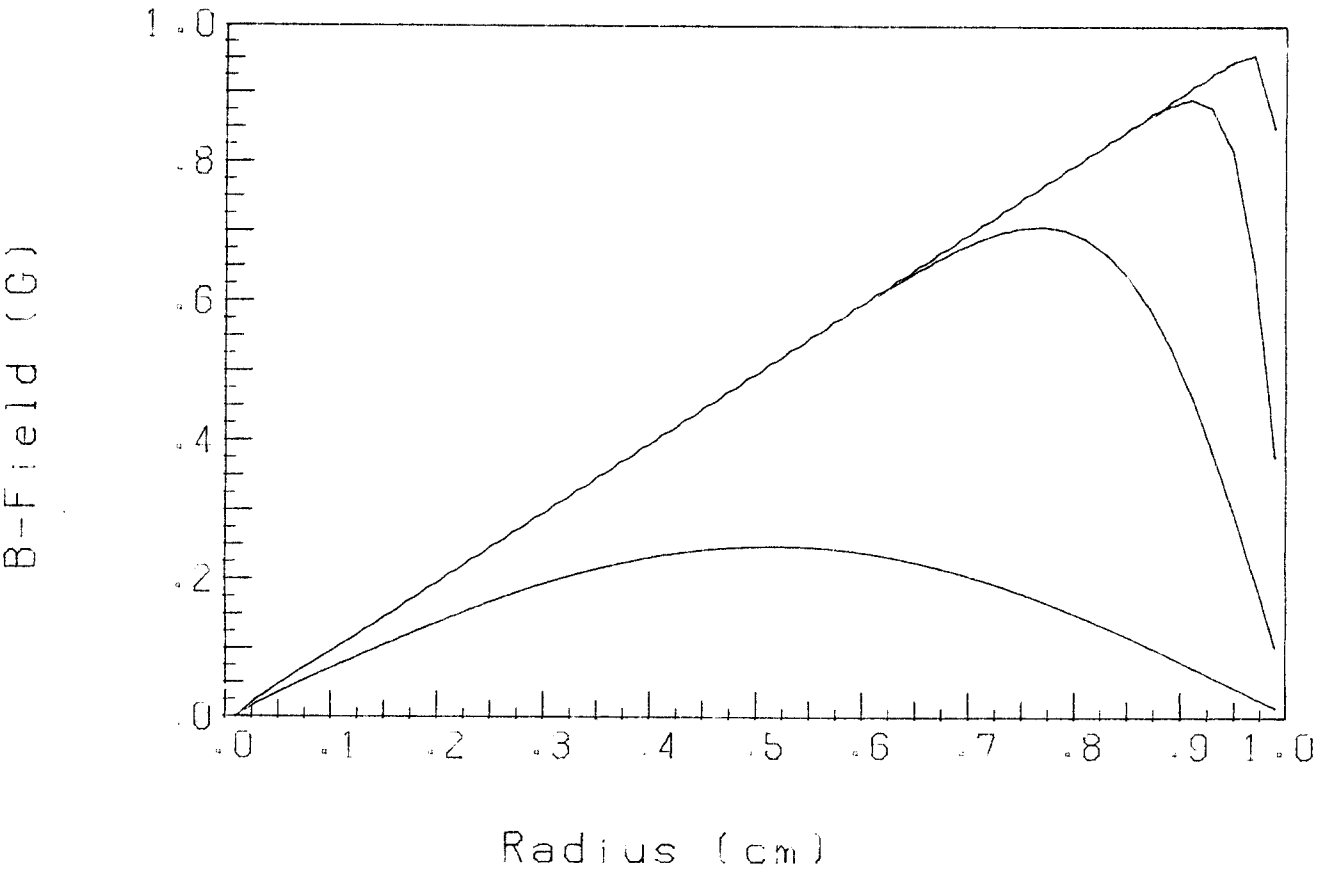

Fig. 4.4b. Magnetic diffusion: decaying field for D = 1 (numerical).

L = inductance in RLC driver

Q_0 = initial charge on capacitor.

The problem is then to find an expression analogous to (4.14) for the voltage drop in the channel, v_{ch}. It is quite tempting to assume that this voltage may be decomposed into a resistance and an inductance:

$$v_{ch} = IR_{ch} + \dot{I}L_{ch} \tag{4.15}$$

as has often been done (cf. Refs. 4 and 5). However, it has been shown that such a decomposition cannot be performed.[6,7]

The proper treatment of the channel is as a distributed circuit element. One integrates Faraday's Law on some surface, uses Stoke's Law to change the integral of $\vec{\nabla} \times \vec{E}$ to a contour integral, then identifies part of that contour integral with v_{ch}. The remainder of the contour integral is reduced to an expression involving the magnetic field and current density by means of Ohm's Law. The result is that the voltage drop per unit length in the channel is

$$v_{ch} = \eta(0,t)\ J(0,t) + \frac{1}{c} \int_0^a \frac{\partial B}{\partial t}(r,t)\ dr\ . \tag{4.16}$$

Using this result in Kirchhoff's Law, the equation for the current becomes

$$L\dot{I} + RI + \frac{1}{C}\left[\int_0^t I(\tau)\ d\tau + Q_0\right] = v_0(t) - \left[\eta(0,t)\ J(0,t) + \frac{1}{c}\frac{\partial}{\partial t}\int_0^a B(r,t)\ dr\right]\ . \tag{4.17}$$

Taking the time-derivative of (4.17) and dividing through by L, this equation becomes

$$\ddot{I} + \left(\frac{R + \dot{L}}{L}\right) \dot{I} + \left(\frac{\dot{R} + 1/C}{L}\right) I = \frac{1}{L} \frac{dv_o}{dt}(t) - \frac{1}{L} \frac{\partial}{\partial t} \left[\eta(0,t)\, J(0,t) + \frac{1}{c} \frac{\partial}{\partial t} \int_0^a B(r,t)\, dr\right] . \tag{4.18}$$

Before discussing the treatment of this equation, it is interesting to compare Eqs. (4.15) and (4.16). Suppose B(r,t) could be expressed in the form

$$B(r,t) = I(t)\, f(r) . \tag{4.19}$$

Then, from Ampere's Law,

$$J(r,t) = \frac{c}{4\pi} \frac{I(t)}{r} \frac{\partial}{\partial r} r\, f(r) \equiv I(t)\, g(r) .$$

Using these, (4.16) may be put into the form

$$v_{ch} = [\eta(0,t)\, g(0)]\, I(t) + \left[\frac{1}{c} \int_0^a f(r)\, dr\right] \dot{I}(t) . \tag{4.20}$$

Comparison of this with (4.15) shows

$$R_{ch} = \eta(0,t)\, g(0)$$

and

$$L_{ch} = \frac{1}{c} \int_0^a f(r)\, dr .$$

However, the analytic solution, Eq. (4.10a), shows that the magnetic field cannot be expressed as a simple product, as in (4.19), but is a convolution of the current with some function of space and time. The essence of this solution cannot be expected to change for the more complicated problem of a non-rigid channel. Thus, one cannot expect that the voltage drop in the channel could be decomposed into a resistance term and an inductance term.

The current equation may be written in the more generic form

$$\ddot{I}(t) + a_1(t)\,\dot{I}(t) + a_2(t)\,I(t) = b(t) + K(I(t)) \,. \tag{4.21}$$

K is an integral operator:

$$K(I(t)) = \int_0^t k(I(\tau),\tau,t)\,d\tau \,. \tag{4.22}$$

If the electrical resistivity is taken as a known function of time and position and the channel is rigid, as in MAGDIF, then K is linear. If, on the other hand, η is calculated from (4.1) and the channel is allowed to undergo hydrodynamic motion, K will be a nonlinear operator. The nonlinearity arises from the current-dependence of the temperature through Joule heating and of the hydrodynamic response through the $J \times B$ force.

Since, at the beginning of a timestep, neither I nor B is known, the numerical solution to Eqs. (4.21) and (4.7a) requires an iterative method. One would use a guess for B(r) to solve (4.21), use that result to generate a new B(r) by solving (4.7a), then repeat that procedure until the solution had converged satisfactorily. However, the method of solution of the hydrodynamics equations in MF-FIRE makes this iterative procedure unnecessary. In MF-FIRE,

the hydro equations and the equation of state are solved sequentially just once per timestep - there is no iteration or updating between the equations. The accuracy gained by iterating between (4.21) and (4.7a) would be lost in the inaccuracies accepted in the solution of the hydrodynamics equations.

The method of solution that has been adopted for Eq. (4.21) is an approximate method. The exact solution of this equation would require its treatment as a nonlinear integro-differential equation. It has been shown that (4.21) may be cast into the form of a Volterra integral equation:

$$I(t) = \int_0^t G(t,\tau)\ [b(\tau) + K(I(\tau))]d\tau\ , \qquad (4.23)$$

where $G(t,\tau)$ is the Green's function for the differential part of the operator in (4.21). Proper treatment of the current would then require that (4.23) be solved with an appropriate numerical method. This course of action may be returned to in the future, but for now, a simpler treatment has been adopted. In the course of analysis of Eq. (4.21), an observation was made that motivated this simpler treatment. This observation was that in all calculations performed with MAGDIF thus far, the last term on the right hand side of (4.21) is small in comparison to the other terms, usually by several orders of magnitude. This motivated the treatment of Eq. (4.21) as a second order inhomogenous ODE, i.e. ignore the dependence of this last term on the current and treat it as a function of time only. This can be viewed as the first step in the iterative procedure described above. It is akin to the Born approximation used in quantum mechanics. As long as the rate of change of the channel voltage drop is not too large and the external inductance is not too small, this approximation should be fairly accurate. The code uses a 4th order Runge-

Kutta algorithm to solve (4.21). This algorithm has been provided with its own timing mechanism so that its timestep constraints will not affect the timestep in the hydrodynamics calculation.

4.2.2.3 The Conservation Relations. As mentioned above, the numerical solution to the equations governing the field and the current cannot be considered acceptable until certain conservation relations are satisfied. These relations also help to point out and track down errors in both coding and modeling. Three conservation relations are used in MAGDIF: conservation of current, magnetic flux, and energy. The first two involve little more than integrating the equations solved in the code. The relation between the energy balance and the magnetic diffusion equation is not so transparent. It provides an independent check on the solution.

The current conservation relation compares the current in the channel to the integrated current density. It should be that

$$I = 2\pi \int_0^a J(r)\, r\, dr \ . \tag{4.24}$$

The current density is obtained from the magnetic field through Ampere's Law. It has been found that there is litle trouble in satisfying (4.24). The errors are generally below 5% and can be reduced by increasing the number of zones or by using a more sophisticated quadrature scheme for integrating the current density. For the case of constant resistivity, it was found that the relative error between the actual current and the integrated current density using a simple trapezoidal integrator was

$$\varepsilon(\%) = 100\left[\frac{1}{N(1 + 4N)}\right] , \tag{4.25}$$

where N was the number of zones.

The magnetic flux conservation relation is a check on how well Faraday's Law is satisfied. One integrates Faraday's Law in space and in time from timestep to timestep. The electric field is calculated from the magnetic field by using Ampere's and Ohm's Laws. For the case of constant resistivity, the flux conservation relation is satisfied to within an extremely small error -- something less than 10^{-2}%. However, for the case of spatially varying resistivity, things do not work out so well. The trouble is due to the sacrifice made in the inner zone for the magnetic field calculation. From Faraday's Law, one can see readily that in the steady state, the electric field is constant over the radius of the channel. However, because of the error made by forcing the magnetic field to zero at $r = r_{1/2}$, the steady state electric field varies rapidly with the radius near the axis. The error between the code's steady state electric field and the true steady state electric field is very small away from the axis, but rises to around 40% near the axis. The sign of the error depends on the curvature of the magnetic field. If the magnetic field is concave upward near the axis, the steady state electric field is too small near the axis, and vice versa. These observations hold true qualitatively for non-steady electric fields. This will be important to keep in mind in doing real channel calculations. In realistic channels, the magnetic field is expected to be concave upward near the axis. The electric field will then be underestimated on the axis, which will affect the Joule heat term. However, since the magnetic field is also underestimated near the axis, the decrease in hydrodynamic expansion due to underestimated Joule heating may be balanced by an increased expansion due to the underestimate in the pinch or magnetic pressure effect.

In hydrodynamics calculations, energy conservation relations usually are integrated forms of the temperature equation. In MF-FIRE, for example, the energy check is just the space and time integral of the plasma and radiation temperature equations. This is just due to the fact that the temperature equations are simply energy balances in differential form -- they express how energy flows from one point to another. This is not true for the magnetic diffusion equation: the energy density associated with a magnetic field is quadratic in the field strength, but the diffusion equation is an equation for B, not B^2. Integrating (4.7a) over space and time does not give an energy balance. The diffusion equation is not used directly as the basis for the energy check. Rather, the dot product between the magnetic field and Faraday's Law is formed. Using Ampere's Law without the displacement current then gives the energy conservation equation

$$\frac{\partial}{\partial t}\frac{B^2}{8\pi} = - I v_{ch} - \vec{J} \cdot \vec{E} . \qquad (4.26)$$

This equation is then integrated over space and time. It has been found that in all problems attacked so far -- which includes, among others, the problems discussed in Section 4.2.2.1 -- this relation is satisfied to less than one or two percent error. This level of accuracy is sufficient to indicate that the code solves the given problems to an acceptable level of accuracy.

4.3 Summary

The first part of the task of MHD code development has been accomplished. The result is an intermediate "stand alone" code, MAGDIF, that solves the magnetic diffusion equation and current equation in an approximately self-consistent manner. The code has passed certain tests -- conservation relations and comparisons with known solutions -- and is considered acceptable for the next phase. This phase, the coupling of MAGDIF to MF-FIRE, is currently underway.

References for Section 4

1. G.A. Moses, T.J. McCarville, and R.R. Peterson, "Documentation for MF-FIRE, A Multifrequency Radiative Transfer Version of FIRE", University of Wisconsin Fusion Engineering Program Report UWFDM-458 (March 1982).

2. R.E. Kidder, D. Steinberg, A.B. Cecil, "A One-Dimensional Magnetohydrodynamics Code", Lawrence Livermore National Laboratory Report UCRL-14931, (June 1966).

3. M. Abramowitz and I.A. Stegun, eds., Handbook of Mathemetical Functions, U.S. National Bureau of Standards, (1964), Dover, New York.

4. S. Kawata, K. Niu, and H. Murakami, "Formation of Z-Discharged Plasma Channel in LIB-Fusion Device", IPPJ-601.

5. J.L. Neuringer, L. Kraus, and H. Malamud, "Electromagnetic Diffusion into a Cylindrical Plasma Column During the Early Stages of Pinch Formation," Phys. Fluids, Vol. 4, No. 8, August 1961, p. 105.

6. W. Manheimer, "Energy Input into a Gas-Enclosed Z-Pinch," Phys. Fluids, Vol. 17, No. 9, Sept. 1974, p. 1767.

7. D.G. Colombant and M. Lampe, WHYRAC: A New Modular One-Dimensional Exploding Wire Code, NRL Mem. Rep. 3726, Feb. 1978.

5. ION PROPAGATION THEORY

5.1 Introduction

The propagation of ion beams in preformed plasma channels from ion diodes to the target is crucial to the LIBRA concept. The results of study of several critical issues dealing with ion beam propagation are presented in this section.

Any discussion of ion beam propagation should begin with a consideration of the ion beam requirements for inertial confinement fusion. One needs to know the requirements for ICF on the ion beam and pulse power systems before investigating beam stability, beam slowing and diode designs. This is done for LIBRA relevant parameters in Section 5.2.

In order to learn the constraints on the propagation of ion beams in plasma channels, the nature of plasma instabilities must be understood. This has been done by studying the existing theoretical literature. This and some related original work on the nature of the relevant plasma instabilities is described in Section 5.3. This information allows the design of beam propagation systems. A computer code, called WINDOW, is described in Section 5.4, which uses the information in Section 5.3 to find the allowable operating ranges of the ion beam-channel system.

Another important theoretical issue is the macroscopic behavior of the ion beam while it is in the channel. The beam current and charge densities are very closely coupled to electric and magnetic fields in the channel: they greatly affect the fields and they are affected by them. In fact, energy loss by beam ions may be due in great part to these fields. The nature of these fields has been studied and is discussed in Section 5.5.

There has been very little work to date on the type of rep rateable ion diode that would be needed for LIBRA. Sandia National Laboratory has just recently begun experimental lithium diode work and these diodes are of lower anode-cathode potential drops than LIBRA needs and are not repetitive. A new concept for a repetitive lithium diode with a 30 MV potential drop is discussed in Section 5.6.

5.2 Particle-Beam and Pulsed-Power Requirements

Scaling laws and operating parameter requirements for pulsed-power modules and particle-beam transport in LIBRA have been developed. Target parameters are E_T (MJ), P_T (TW/cm^2), ε_i (MeV), A_T (cm^2). Ion energy ε_i is a target parameter since ε_i and Z_i determine the specific range (mg/cm^2) in the target. The beam pulse length at the target is

$$I_b^T = E_T/P_T A_T.$$

Requisite power-density P_T and energy E_T are achieved by overlap of N_b beamlets. Target parameters P_T, E_T are linked by the overlap gain fraction g_o, which characterizes beam-target coupling, to the beam parameters P_b^T, E_b^T at the target, by

$$P_b^T/E_b = P_T/E_T/g_o.$$

Overlap gain fraction is the fraction of N_b which contributes at a given area element on the target. A theoretical maximum is $g_o = 1/4$. Axial compression gain g_c is the factor by which the beams compress due to a programmed

diode voltage. The ideal voltage waveform is $V(t) = V_o(1 - t/t_a)^{-2}$ where $0 \leq t \leq t_b \leq t_a$, t_b is the pulse length, and t_a the time of arrival of the pulse at the target.

Beam parameters at the injection plane are:

$P_b^I(TW/cm^2) = P_T(TW/cm^2)/g_o/g_c/N_b$	injected power density
$\tau_b(ns) = 100\ g_a E_T(MJ)/P_T(TW)$	pulse length

From these the remaining parameters of interest are gotten:

$I_b^I(MA) = 10\ P_b^I(TW)/\phi(MV)$	beam current at injection
$\phi(MV) = \varepsilon_i(MV)/Z_i$	diode voltage
$n_b = E_b(MJ)/e\varepsilon_i(MeV)$	number of ions per beam
$J_T(MA/cm^2) = 10\ P_T(TW/cm^2)\ \phi(MV)$	current density on target surface
$V_i^I(cm/ns) = 30[2\ \varepsilon_i(MeV)/m_i]^{1/2}$	ion velocity at injection
$\ell_b^I(cm) = 3000\ g_c E_T(MJ)/P_T(TW) \cdot V_i^I(cm/ns)$	pulse length at injection

Target parameters relevant to LIBRA are:

$$(Li\text{-}7)^{+3}$$

$$\varepsilon_i = 30\ MeV$$

$$E_T = 5\ MJ$$

$$P_T = 100\ TW/cm^2$$

$$A_T = 1\ cm^2.$$

If the system is designed so that the beam target coupling parameters are:

$$g_c = 5$$

$$g_o = 0.25$$

$$N_b = 20$$

$$A_b = 0.785 \text{ cm}^2,$$

the operating parameters which result are:

$$E_b = 0.25 \text{ MJ}$$

$$P_b^I = 4 \text{ TW/cm}^2$$

$$P_b^I = 3.14 \text{ TW}$$

$$\tau_b^I = 25 \text{ ns}$$

$$I_b^I = 1.57 \text{ MA}$$

$$n_b = 7.8 \times 10^{16}$$

$$V_i = 3 \text{ cm/ns}, \ell_b^I = 72 \text{ cm}.$$

The pulsed power modules are each called upon to supply 1.57 MA at a power level of 3.14 TW, at the injection plane.

Pulsed power is focused into the injection plane focus by the ion diode. Ion diode brightness is

$$B_d(\text{TW/cm}^2\text{/ster}) = 10^3 \, V_d(\text{MV}) \, J_d(\text{kA/cm}^2)/\theta_m^2(\text{mrad}).$$

A spherical sector subtending a solid angle of 0.01 steradians with a focal length of 50 cm has an anode area of 314 cm^2 and a required brightness B_d = 100 $\text{TW/cm}^2\text{/ster}$. Brightness levels such as this are an order of magnitude above those presently attainable.

To summarize, each pulsed power module in a LIBRA fusion reactor system must operate with high efficiency ($\gtrsim$ 25%), at a repetition rate ($\sim$ 1 Hz), for a great number of shots ($\gtrsim 10^9$), with reasonably high reliability and a realistic capital cost. Required operating parameters are a short pulse (25 ns), at a high brightness ($\gtrsim$ 100 TW/cm^2/ster), high power (1-5 TW), high current (1-5 MA), and high energy per pulse (0.25-1 MJ), focused onto a 0.5 cm radius spot size. Assuming these requirements have been achieved, the next problem is the efficient transport of the high intensity ion beam over several meters to the fusion target.

The source focal length is limited by the intrinsic source divergence angle, and by the desired focal spot size, which is essentially the diameter of the target, about 0.5 cm radius. It cannot be realistically anticipated that the divergence angle will ever be much less than 0.5 degrees, hence the focal length is limited to 50-100 cm. This is not adequate "stand-off" from the target explosion. For this reason it is necessary to propagate a focused beam over a distance of several meters to the target. Transport must take place through the buffer gas which fills the reactor cavity. Intense light ion beams produced by ion diodes or linear accelerators may be focused and propagated to a fusion target in essentially two different ways: the beam may be transported in a pre-existing, hydrodynamically stable Z-pinch plasma channel; or it may be injected directly into a neutral gas environment. The latter mode is called the self-pinched, or self-formed plasma channel mode of propagation.

Z-pinch beam transport channels are initiated by low energy lasers (2 J) which, through a number of possible mechanisms, create preferred directions for breakdown of the buffer gas. External capacitor banks are discharged

through the thin ionization paths on a short enough rise-time to result in radially traveling shock waves which sweep much of the buffer gas out, providing a rarefied plasma channel surrounded by dense, cold, neutral gas. The high density cold gas helps to provide hydrodynamic stability of the plasma channels. Azimuthal magnetic fields within the plasma channel confine the injected beam as it propagates to the target.

Plasma channels provide a background of mobile charge, which is available to neutralize the electrostatic repulsions within the beam. In cold gas on the other hand, self-pinched beam transport is possible since the ions strip rapidly, and as such, are effective in ionizing the background gas. Collisional ionization and electric field breakdown processes at the head of the beam result in rapid gas ionization so that the remainder of the beam pulse propagates in a hot plasma environment, and is effectively charge neutralized in this manner.

Z-pinch plasma channels require many modules since the transport channel diameter is quite small, comparable to the target diameter. Self-pinched beams on the other hand may be several times greater in diameter than the target. The result is an easing of MHD stability requirements, consequently, greater beam power per channel may be realized in the self-pinched mode. However, this requires a magnetic final focusing element at the target, a concept which is problematical as yet.

Successful transport is critically dependent upon questions of stability of the combined beam-plasma system. Operation parameters must be such that no harmful MHD instabilities can disrupt the transport. Current and space-charge neutralization will fail in the event that electrostatic or electromagnetic microinstabilities are driven by the passage of the beam. If these modes grow

on time scales shorter than the beam pulse duration, the resulting anomalous resistivity can inhibit the induced return currents, destroying the beam. High power beams are subject to a great variety of disruptive macro and micro-instabilities, including two stream, filamentation, kink, hose, Weibel, etc.

Assuming successful transport the next problem is to overlap the beams on the target. Even preformed channels cannot be designed to provide confining fields up to the target surface. The beams will have to propagate through a small gas volume surrounding the target, merging with their nearest neighbors, in a region of great complexity as far as the net field structure is concerned. Analysis of the overlap problem has been carried out and a theoretical maximum limit of overlap gain $g_0 = 1/4$ has been predicted. There is, however, much room for further research dealing with the overlap problem.

5.3 Beam-Plasma Theory

Effects of scattering upon LIBRA ion beams have been investigated. For paraxial beams the transverse and longitudinal phase spaces decouple. However, for long times there will be a secular heating of the transverse degrees of freedom at the expense of the longitudinal degrees of freedom. Assuming paraxial ordering of fields and currents the kinetic equation for the transverse distribution is:

$$\left(\frac{\partial}{\partial t} + \frac{\vec{p}_\perp}{\gamma m} \cdot \frac{\partial}{\partial \vec{r}_\perp} + q\left[\vec{E}_\perp + \frac{\vec{p}_\perp}{\gamma m c} \times \vec{B}_\perp\right] \cdot \frac{\partial}{\partial \vec{p}_\perp}\right) f_\perp = \frac{1}{2} \gamma m \dot{\varepsilon}_t \frac{\partial^2 f_\perp}{\partial p_\perp^2} .$$

The diffusion term represents a heating rate per particle of the transverse phase space. The model developed for $\dot{\varepsilon}_t$ is

$$\dot{\varepsilon}_t \left(\frac{eV}{ns}\right) = 3.8 \frac{z^2}{\beta mc^2} \frac{n_e Z}{10^{18}} \log\left[743 \frac{\beta mc^2}{\ell} \left(\frac{T_e}{n_e}\right)^{1/2}\right]$$

$$\ell = \max\left[10^{-13} \frac{zZ}{\beta} , 10^{-10}\right] .$$

For parameters, given in the previous section and a sample plasma temperature T_e = 25 eV and an effective channel ion charge state Z = 1, electron density $n_e = 10^{18}$ cm^{-3}, the transverse volumetric heating rate is 10^{10} MeV/cm^3/ns whereas the beam energy density is 10^{17} MeV/cm^3. The fractional heating rate is 10^{-8}/ns. Energy loss is negligible as far as the longitudinal energy is concerned. For a beam which propagates on the order of several meters transverse pressure due to heating causes beam expansion.

LIBRA beams will not have any net fluid rotation, but particles will have angular momentum. The distribution is independent of direction in the cotangent spaces at all points (r,θ):

$$f_\perp(r_\perp, \hat{r}_\perp, P_\perp, t) .$$

The collision operator conserves angular momentum density so that this property of $f_\perp$ will be time invariant.

In the zero angular momentum density or $\vec{p}$-isotropic case the lowest moments of the kinetic equation yield

$$\frac{\partial n_\perp}{\partial t} = 0$$

$$\frac{\partial \varepsilon_\perp}{\partial r_\perp} - \frac{1}{2} F n_\perp = 0$$

$$\frac{\partial \varepsilon_\perp}{\partial t} + \varepsilon_\perp \frac{\dot{\gamma}}{\gamma} = n_\perp \dot{\varepsilon}_t \ .$$

It turns out that $f_\perp$ is axisymmetric in this case. In Section 5.5, a field solver is described. This code computes induced densities and fields in the channel, given the beam current and charge densities. The code can be applied either to a beam slice or a full axial profile. Given the time dependence of $\gamma(t)$ the $\vec{p}$-isotropic fluid equations are solved for the beam profile $n_\perp(r,t)$. A flip-flop calculation then allows numerical simulation of the propagation of a beam slice. The time dependence of the induced fields, densities, transverse phase space heating, and beam profile may be computed in the $\vec{p}$-isotropic case.

Analytical solution of the $\vec{p}$-isotropic transverse fluid equations yields the result that the energy density $\varepsilon_\perp$, the temperature $T_\perp$, and the Lorentz force F grow self-similarly with time, due to the secular slowing down of the beam. Scattering destroys this self-similar behavior, except in the case of the temperature.

A model for collisional slowing down of LIBRA beams has been developed. For parameters given previously the volumetric loss rate of the beam, which is the plasma heating rate, is 10^{13} MeV/cm^3/ns. Heating of the channel plasma causes the temperature to rise until the radiative loss balances the beam heat input. Maximum plasma temperature can be estimated by treating the channel as a blackbody radiator. The resulting maximum channel temperature is:

$$T_{max} = \left(\frac{P_H}{\sigma} \frac{V}{A}\right)^{1/4}$$

where V/A is the volume/area ratio of the channel slice. For the parameters

given $T_{max} \sim 10$ eV. After passage of the beam the channel temperature falls off as $(at + 1)^{-1/3}$.

It is of interest to estimate the relative amounts of beam heating that derive from individual and collective deposition. At 10 eV about 25% is deposited collectively. The beam-plasma consists of hot plasma ions, hot electrons with a drifting component, and a relatively diffuse cloud of beam ions which are continuously emitting excitations as they stream along, the thin turbulent streamers trailing behind each ion represent local sources of noise.

The mean separation between beam ions is $\sim 10^{-5}$ cm which is the same order of magnitude as the collective thermalization radius. Excitations emitted by neighboring beam ions will interact with one another prior to thermalization. Enhanced fluctuation levels thus generated provide the source of potential growing modes, feeding on the energy of the beam collective mode.

5.4 Plasma Stability Constraint Calculations for LIBRA

The plasma stability theoretical investigations described in the preceding section lay the groundwork for the study of the constraints on ion beam propagation in preformed plasma channels. A small computer code, based on the work of Ottinger, Goldstein and Mosher,[1] has been written to define the conditions on the propagation of a single ion beam. These conditions locate a range of beam divergence, power per beam space, where propagation is possible. This computer code is called WINDOW.

The five conditions considered in WINDOW are electrostatic stability (ES), stability against beam filamentation (BFIL), stability against channel filamentation (CFIL), low magnetohydrodynamic expansion of the channel (MHD)

and acceptable energy loss by the beam while travelling through the channel (ELOSS). The condition on ES is that the electron temperature in the channel must remain below a critical temperature which is dependent upon parameters defining the beam and channel plasmas including the emittance of the beam. Physically, when the electron temperature is below this temperature the two-stream instability, which is the most important mode, will be collisionally damped. The BFIL constraint is met if the emittance of the beam, which is defined as R/F, where R is the radius of the diode and F is its focal length, is above a value determined by the plasma parameters. If the beam current density is too high, the return current in the channel can filament the channel and CFIL will be violated. Thus, there is a critical beam current density above which the channel will filament. The MHD constraint is met by requiring that the channel does not expand by more than 25% during the transmission of the beam. $\vec{J} \times \vec{B}$ forces mainly drive the expansion so that this constraint becomes a limit on the beam current. Of the five constraints, this is the only one which is independent of the beam emittance. The self-consistent electrical fields that are described in Section 5.5 slow the beam ions which is the most important part of the ELOSS constraint, with inductive energy losses being more important than resistive. Specifically, the constraint is that the ions lose less than 25% of their energy. In WINDOW, these constraints are formulated into curves in the beam power P versus beam emittance R/F plane.

The code is very easy to use and produces a plot of the maximum beam power allowed by each of the constraints versus R/F. WINDOW is written in FORTRAN and reads a NAMELIST input file called INPUT which can contain values

for any of the variables given in Table 5.1. If INPUT contains no value for a variable, the default value is used. From these plots (an example is shown in Fig. 5.1), one can find the operational window where all five constraints are met.

One shortcoming of WINDOW is that it is presently only usable for channels in deuterium gas. This is so because the MHD constraint is very difficult to determine for non-hydrogenic atoms where the non-ideal equation of state and the details of ionization and radiative properties of the channel must be considered. As the work described in Chapter 4 progresses, increased knowledge about these processes will lead to the generalization of WINDOW to other channel species.

The example results shown in Fig. 5.1 is for what might be a first guess at the LIBRA base case. The beam energy is 30 MeV, the beam species is $^{7}Li^{+3}$, the mass density of the channel is the optimum and the channel radius is 0.75 cm. ES, CFIL and ELOSS are the important constraints in this case while BFIL and MHD play no role. An operating point might be R/F = 0.1 radians and P = 10 TW. For TBEAM = 5 x 10^{-8} s, 5 MJ of input energy would require a total power of 100 TW, so LIBRA would require 10 such beams.

Ottinger, Goldstein and Mosher[1] have proposed using the largest reasonable channels because the power allowed per beam is roughly proportional to the cross sectional area of the channel. A series of WINDOW calculations for several different channel radii also shows this. The maximum allowable power per channel is plotted against channel radius in Fig. 5.2. At a channel radius of 1.25 cm, only three beams would be required but there is the difficult question of how to focus a beam from a large channel to a smaller target.

Table 5.1. Input Variables for WINDOW

Variable Name	Unit	Default Value	Definition
RFMIN	Radians	1×10^{-3}	Minimum value of R/F
RFMAX	Radians	0.2	Maximum value of R/F
X	unitless	1	Mass density of channel/mass density for minimum energy loss
RBEAM	cm	0.5	Channel radius
ABEAM	amu	7	Atomic mass # of beam ions
ZBEAM	e	3	Charge state of beam ions
TBEAM	s	5×10^{-8}	Duration of beam pulse
EBAR	MeV	30	Average energy of beam ions
NUM	unitless	200	# of points on each curve ($\leq$ 200)
PMAX	TW	2	Maximum power on plot

In summary, theoretical studies of the physics of plasma channels have led to the creation of the WINDOW code. This code can be used to find an operational window for ion beam propagation and will be very useful as a design tool for light ion beam reactor studies.

References for Section 5.4

1. P.F. Ottinger, Shyke A. Goldstein and D. Mosher, "Constraints on Transportable Ion Beam Power," NRL Memorandum Report 4948 (November 1982).

Fig. 5.1

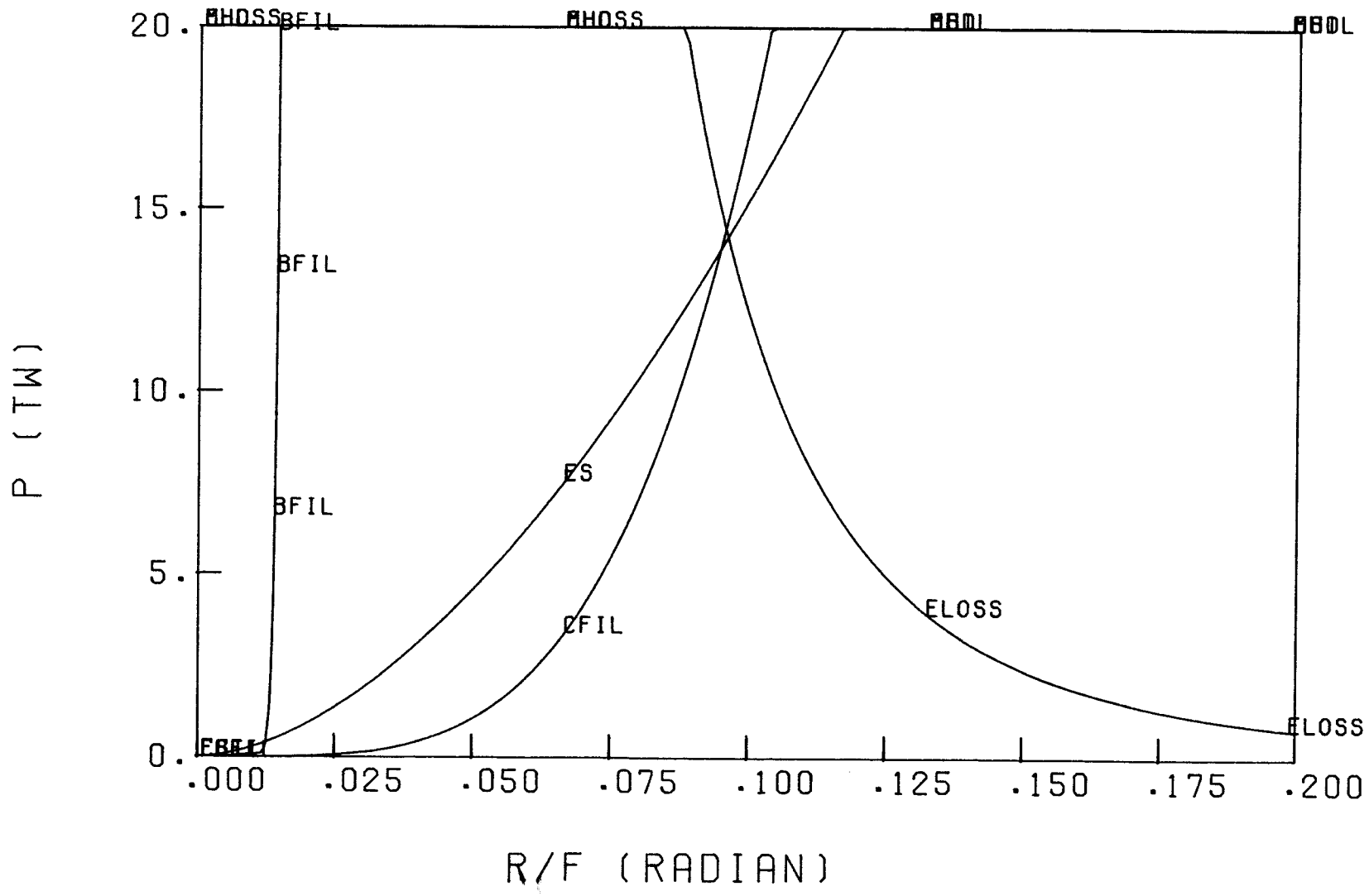

ABEAM=7.0 AMU ZBEAM=3.0 E RBEAM= .8 CM TBEAM=.5000-07 S X=1.0 EBAR=30.0 MEV

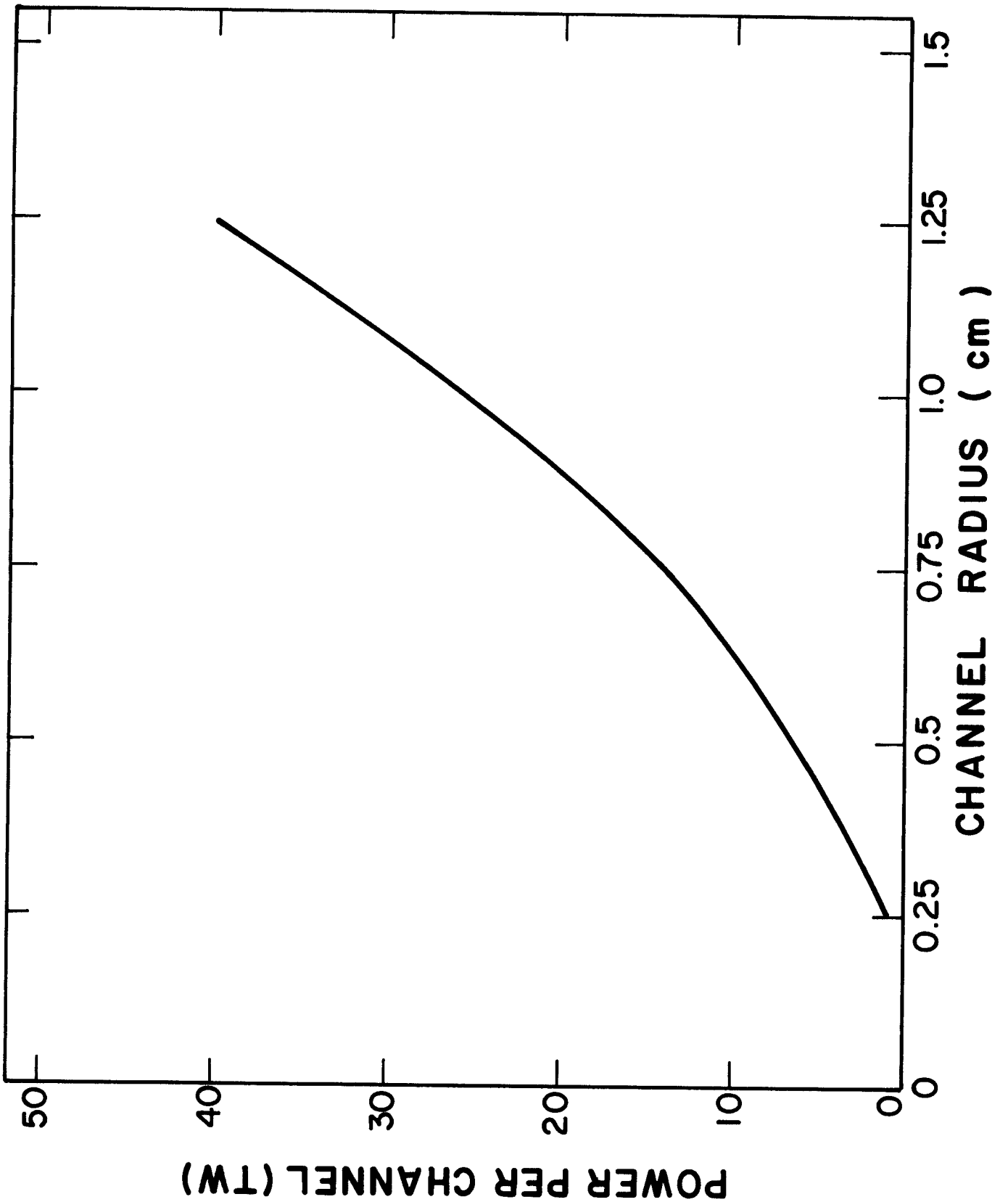
POWER PER CHANNEL (TW)
0
10
20
30
40
50
CHANNEL RADIUS (cm)
0
0.25
0.5
0.75
1.0
1.25
1.5

Fig. 5.2

5.5 Ion Beam Propagation

The problem of modeling intense light ion beam propagation in the LIBRA reactor is being approached in three phases. The first phase is to model the z-pinch plasma channel as a perfectly space and current neutralizing medium and to calculate the ion trajectories in the azimuthal magnetic field created by externally driving a current in the channel. Examples of these simple calculations were presented in the last LIBRA progress report. This trajectory model of Ottinger, Goldstein and Mosher has been further extended to include the effects of nonperfect space and current neutralization through the inclusion of two factors, f_e and f_m, such that the net fields within the ion beam are given by

$$E_r(r) \approx 2\pi q n_0 r(1 - f_e)$$

$$B_\theta(r) \approx 2\pi q n_0 \beta r(1 - f_m) \ .$$

Starting from the equations of motion of the ions, the following equation for radial motion of a beam ion is obtained,

$$\ddot{r} + \alpha r - e\dot{r} = \delta r^{-3} + \sum_{n=2}^{N} B_n r^n$$

where dots refer to derivatives with respect to the axial coordinate z, and the following definitions have been made,

$$\varepsilon = - \frac{\beta\dot{\beta}}{\beta_0 c}$$

$$\alpha = \frac{qB_1}{\beta_o mc^2} - \frac{2\pi q^2 n_o}{\beta_o mc^2}\left[1 - f_e - \beta_o^2(1 - f_m)\right]$$

$$\delta = \left(\frac{P_\theta}{m\beta_o c}\right)^2$$

$$\beta\dot{\beta} = (\beta\dot{\beta})_{\text{collision}} + (\beta\dot{\beta})_{\text{axial field}} \cdot$$

The last term in the trajectory equation refers to a simple model for the magnetic field that takes account of different profiles. Ions near the leading edge see a magnetic field quite different than ions at the trailing edge where the fields have been swept outward by the heated and expanding plasma.

Leading edge ions see:

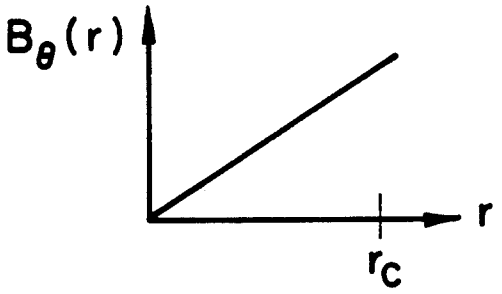

Trailing edge ions see:

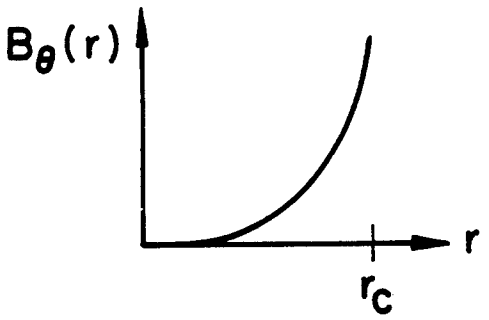

Applying a simple Liapunov stability analysis to the radial equation, which describes a nonlinear autonomous oscillator, in the case of a leading edge ion, one finds the equilibrium points

$$(\dot{r},\ddot{r}) = \left(\frac{\delta}{2}\right)^{1/4} (\pm 1, 0)$$

corresponding to the system

$$\dot{r} = \dot{x}_1 = x_2$$

$$\ddot{r} = \dot{x}_2 = -\alpha x_1 + \varepsilon x_2 + \delta x_1^{-3} .$$

Linearizing the system about this point and computing the eigenvalues results in:

$$\lambda = \frac{1}{2}\,\varepsilon \pm \sqrt{\varepsilon^2 - 4\alpha} .$$

The angular momentum has no effect upon the stability of the orbit, except to influence the position of the nodes, as one realizes by noting that δ has dropped out of the eigenvalues.

The key to applying this simple extension of the orbit analysis is to compute f_e and f_m. To do this we must model the response of the background plasma to the passage of the ion beam. This has been done by solving the equations

$$\frac{4\pi}{\omega_p^2}\frac{\partial \vec{J}}{\partial t} + \frac{1}{\sigma}\vec{J} = \vec{E}$$

$$\vec{J}_b(r,u) = q_b v_n f(u) n(r) \tilde{v}$$

$$n_b(r,u) = q_b f(u) n(r)$$

where $u = z - v_b t$ is the wavefront variable. To these we add Maxwell's equations

$$\nabla \times \vec{B} - \frac{1}{c}\frac{\partial \vec{E}}{\partial t} = \frac{4\pi}{c}\vec{J}$$

$$\nabla \times \vec{E} + \frac{1}{c}\frac{\partial \vec{B}}{\partial t} = 0$$

$$\nabla \cdot \vec{B} = 0$$

and maintain charge neutrality by using

$$\left(\frac{\partial \rho}{\partial t} + \nabla \cdot \vec{J}\right)_b = \left(\frac{\partial \rho}{\partial t} + \rho \cdot \vec{J}\right)_p = 0$$

in place of Poisson's equation. These equations are solved using Fourier transform techniques that will not be reproduced here in detail.

Examples of the calculations that have been done to date are given in the following figures. In Fig. 5.3 we show the ion beam charge distribution, Gaussian along the z axis and a Bennet profile in the radial direction. Plots of the radial and axial electric field components and the azimuthal magnetic field component are shown in Figs. 5.4 to 5.6. In these figures the beam envelope extends in the radial direction from $r = 0$ to $r = 1$ and the channel boundary is at $r = 2$. The conductivity of the channel ($r < 2$) is small but finite and the conductivity outside of the channel is zero. The axial and radial electric fields serve to pull electrons into the beam to neutralize it and to expel electrons once the beam has passed. These plasma response calcu-

Fig. 5.3

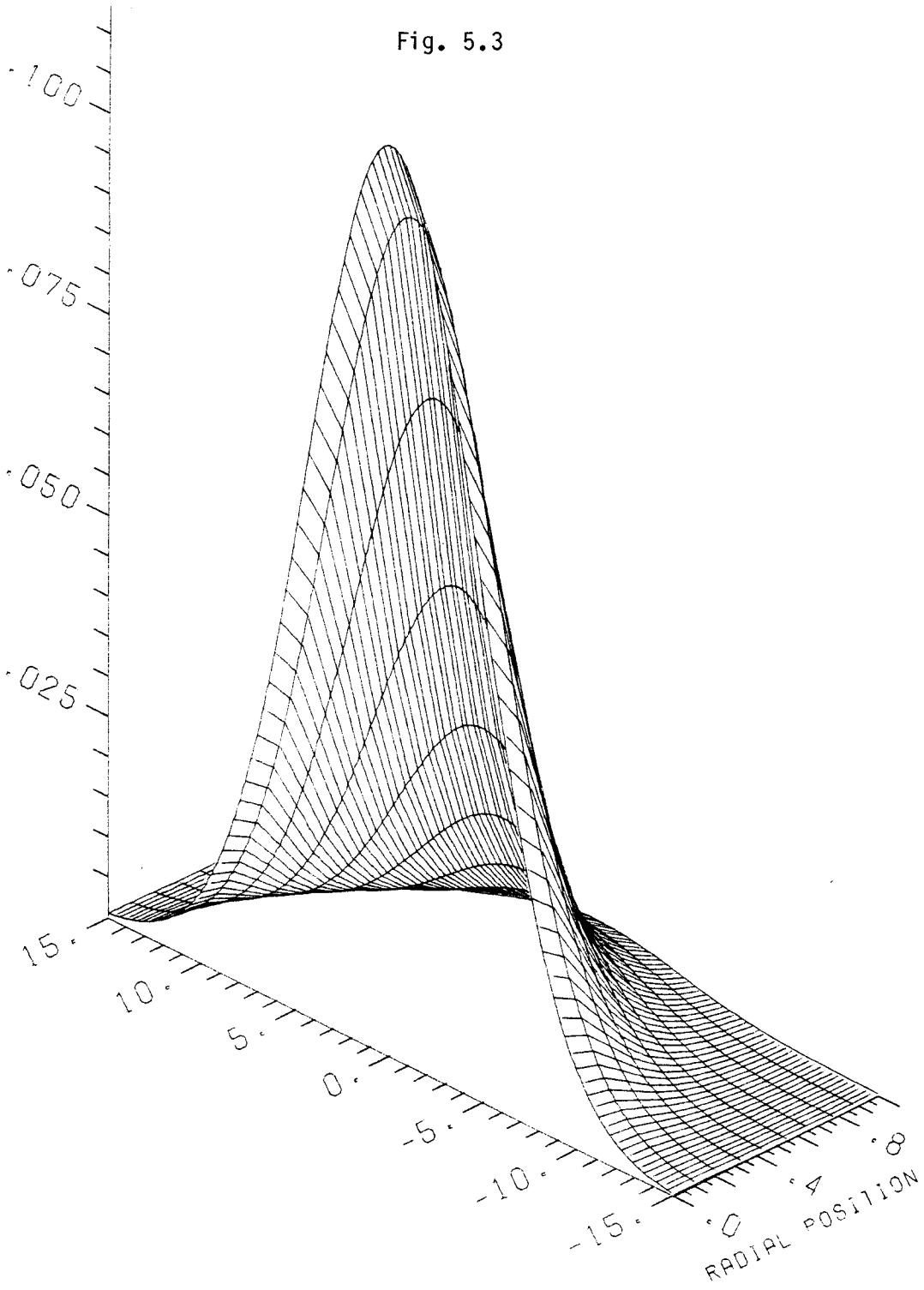

ION BEAM CHARGE DENSITY

Fig. 5.4

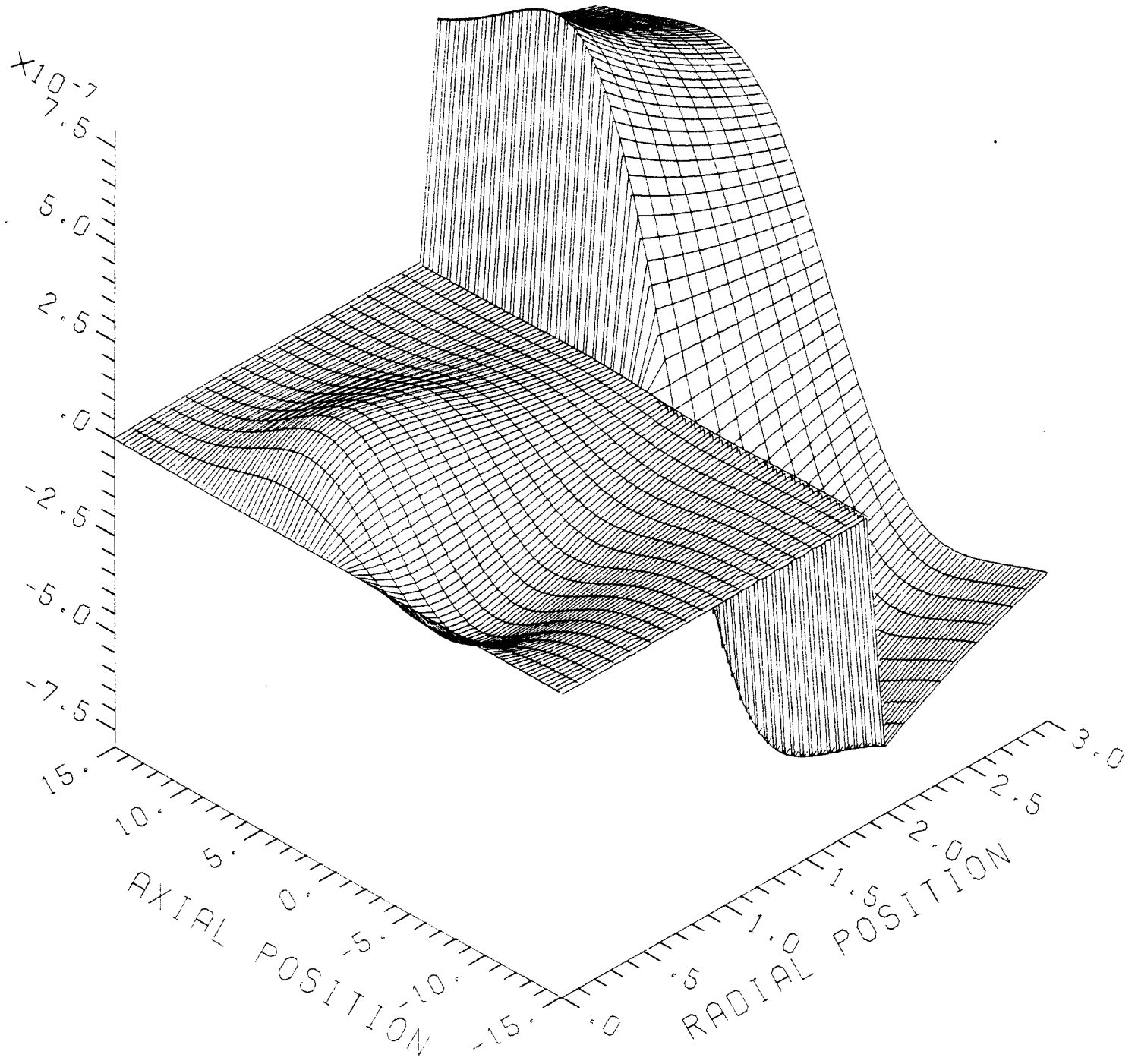

RADIAL ELECTRIC FIELD

Fig. 5.5

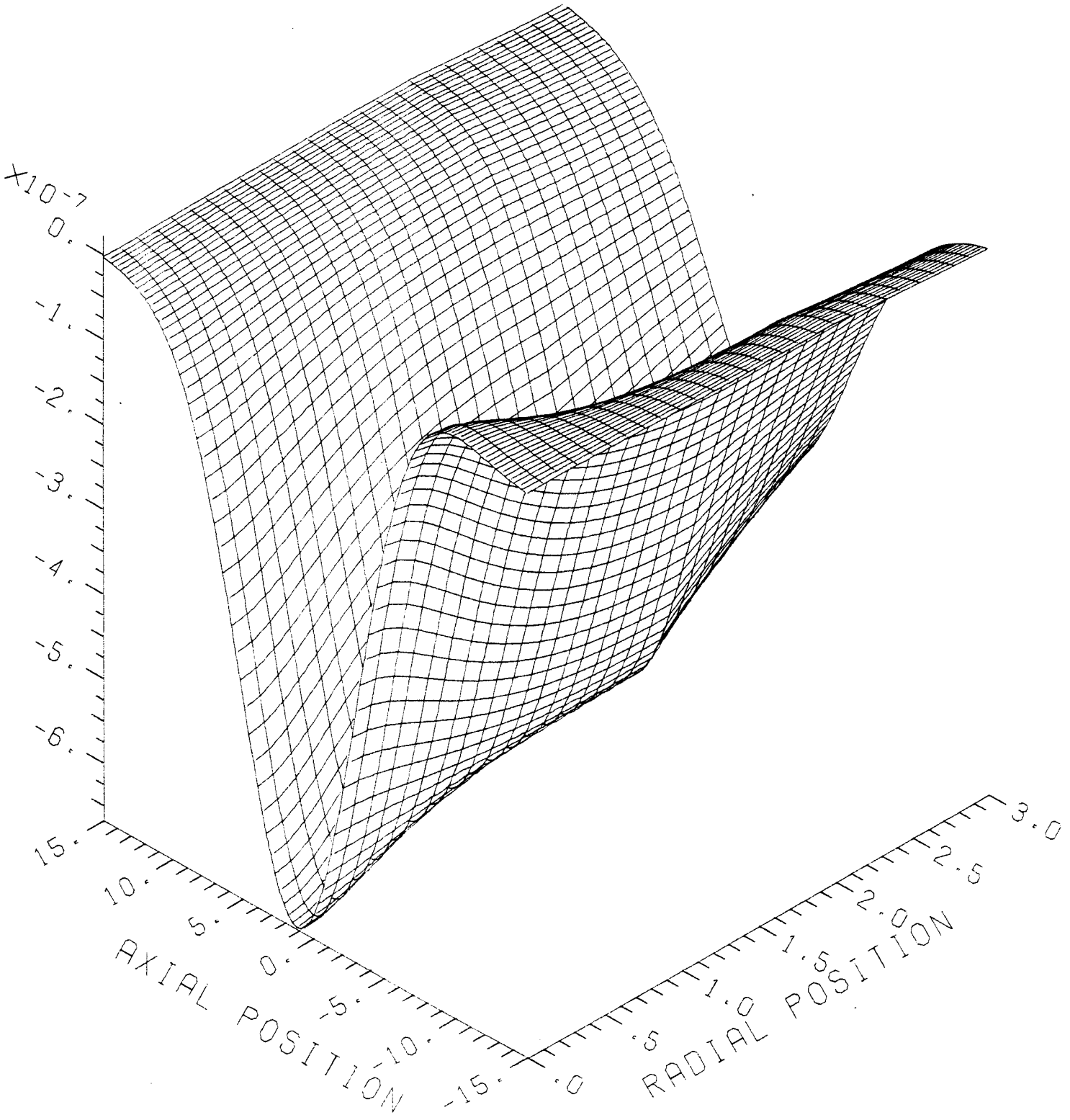

AXIAL ELECTRIC FIELD

Fig. 5.6

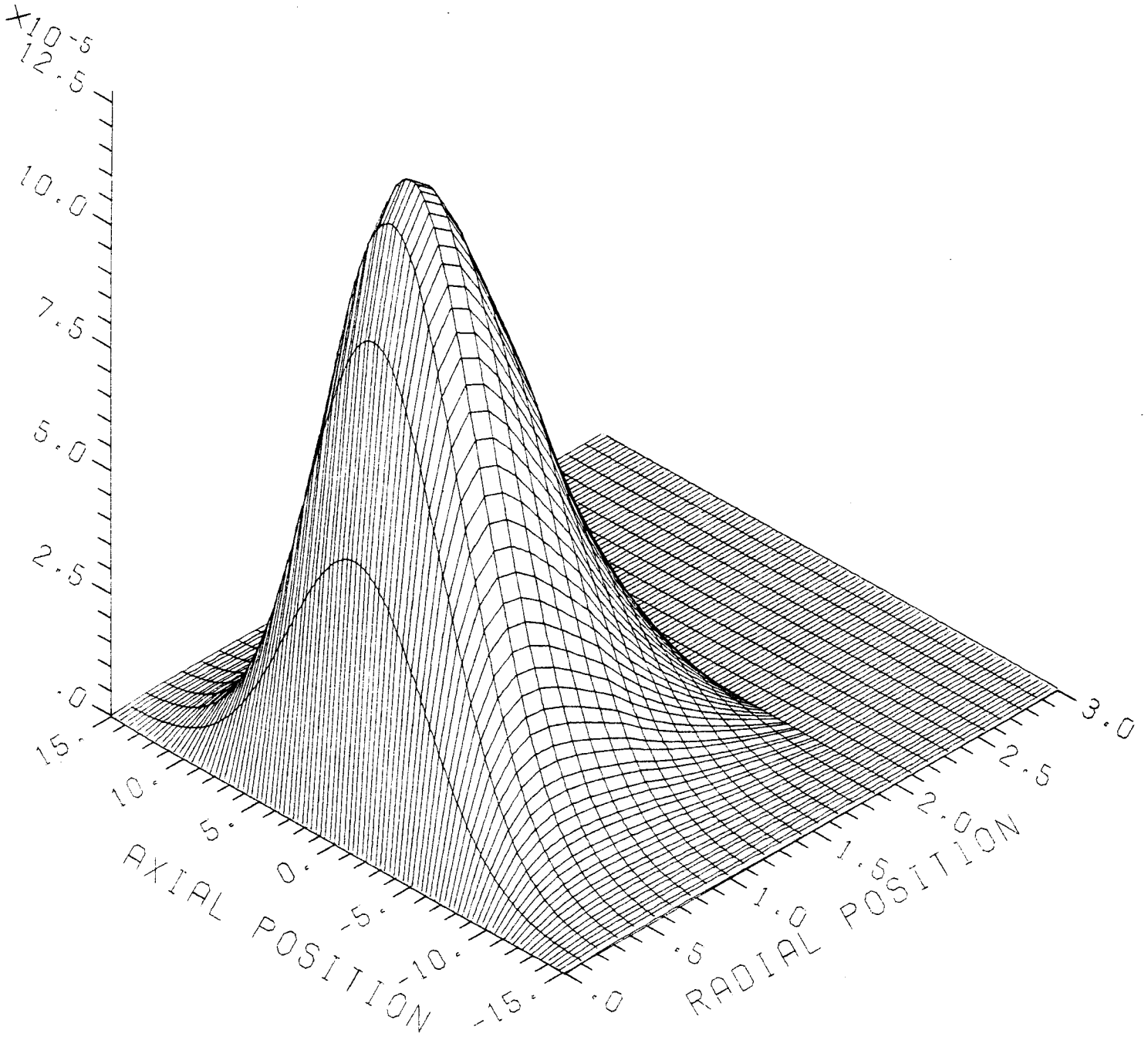

AZIMUTHAL MAGNETIC FIELD

lations will allow us to calculate f_e and f_m. These calculations represent the second phase of modeling.

The third phase of modeling will be to attempt a kinetic treatment of the beam-plasma channel system. Work on the problem is just starting.

5.6 Repetitive Ion Diode for LIBRA

Within the context of the LIBRA design study a proposal for a lithium extraction diode which employs a novel active anode plasma injection scheme has been developed. This diode, called the Ring-Gun Center-Feed diode, is designed to operate in a repetitive mode, and could perhaps meet the objective, articulated by J.P. Van Devender at the Beams 83 Conference, for a "uniform, well-defined, pure anode-plasma."

Center feed diodes were first studied by J. Poukey et al.[1] and subsequent work, refining the ideas, was carried out by Van Devender et al.[2] The ring gun diode is a variation upon these ideas.

Verification of the operation of this diode, theoretically, involves use of 2-dimensional, time-dependent, electromagnetic particle simulation codes, which self-consistently push particles and update fields with field solvers. There has not been time, nor resources, within the context of LIBRA, to develop such codes.

The operating principles of the ring gun diode will be described, to the extent that this is possible in the absence of full simulations.

The essential ideas involved in the ring gun diode are the use of a plasma ring gun to inject the anode plasma, the use of a toroidal virtual cathode consisting of electrons tied to the field lines of the MITL, and the creation of a converging cone of ions, resulting in an annular beam, prior to

mixing in the neutralizing gas fill. The diode is a center feed diode since the inner coax of the MITL provides the negative electrode whereas the anode is outside and concentric with the cathode.

Depicted in Fig. 5.7 is a schematic of the ring gun diode.

At time equal to zero a charged capacitor discharges when the gun circuit is closed. The ring gun accelerates an annular plasma ring which floats at the anode potential when it contacts the anode mesh. A 25 ns, 30 MV pulse travels down the MITL. Upon reaching the open circuit the magnetically insulated electrons burst off the wineglass shaped cathode, emission being caused by Whisker explosion and field emission. The electron flow is trapped in a toroidal configuration by the very strong azimuthal magnetic field, providing magnetic insulation. The circuit is completed by an intense conical flow of ions from the anode plasma. The ion flow passes through neutralizing lithium gas. Upon ionization the plasma space-charge neutralizes the beam.

The intrinsic rms half-angle divergence of the ring gun anode will be related to the temperature of the transverse phase space degrees of freedom. Figure 5.8 shows a schematic of how the diode would fit into a PBFA-I "type" pulsed-power module. The scale is such that the diode chamber and its contents appear to be much larger with respect to the module than it would be in reality. Figure 5.9 shows schematically how the diode chambers might fit into a reactor.

References for Section 5.6

1. J. Poukey et al., Phys. Rev. Lett. 35, 1806 (1975).

2. J. Van Devender et al., J. Appl. Phys. 52, 4 (1980).

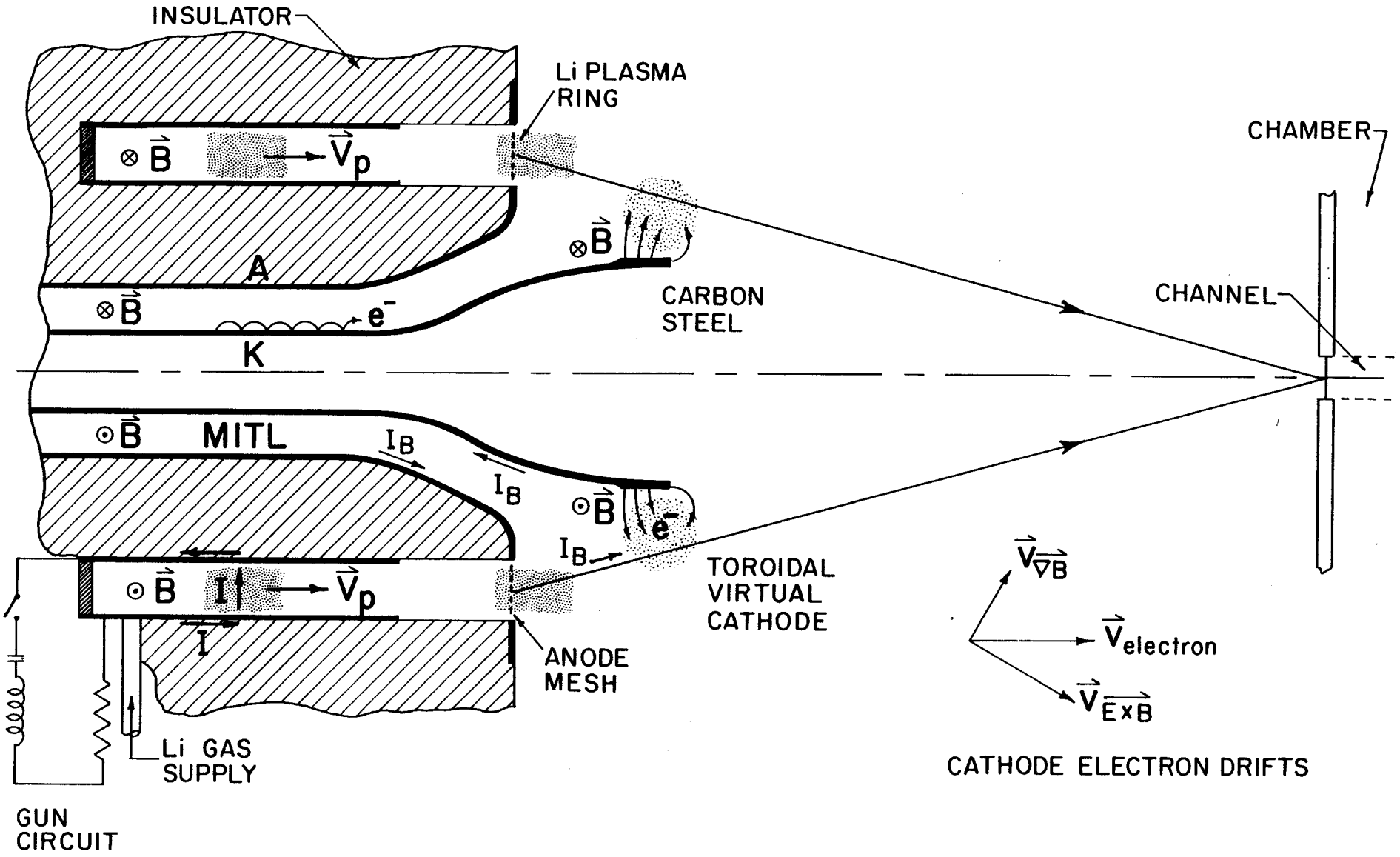

RING GUN CENTER FEED DIODE

Fig. 5.7

Kevin O'Brien
10/6/83

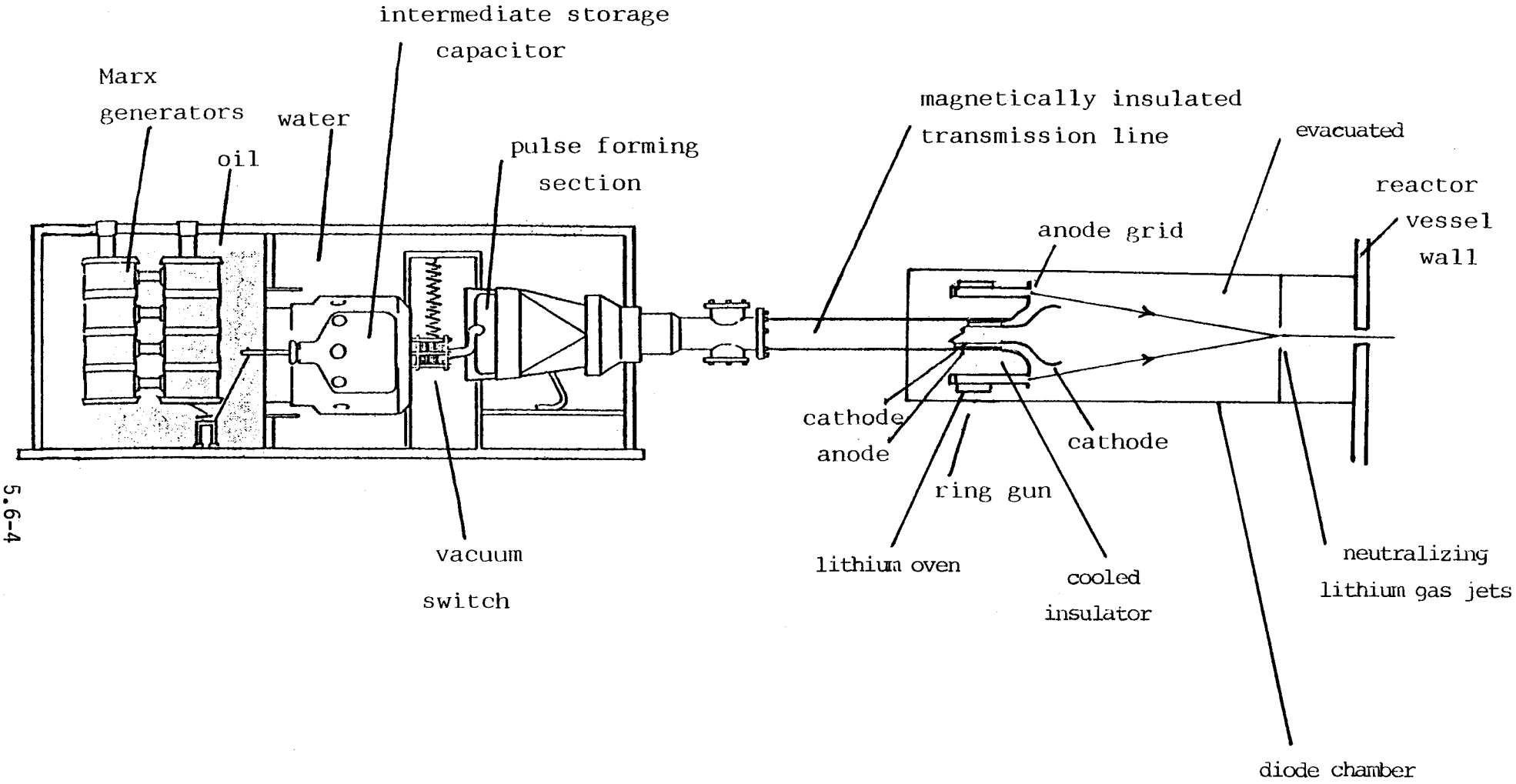
intermediate storage
capacitor
Marx
generators
water
oil
pulse forming
section
magnetically insulated
transmission line
evacuated
reactor
vessel
wall
anode grid
cathode
anode
cathode
ring gun
lithium oven
cooled
insulator
neutralizing
lithium gas jets
vacuum
switch
diode chamber

Fig. 5.8

Fig. 5.9

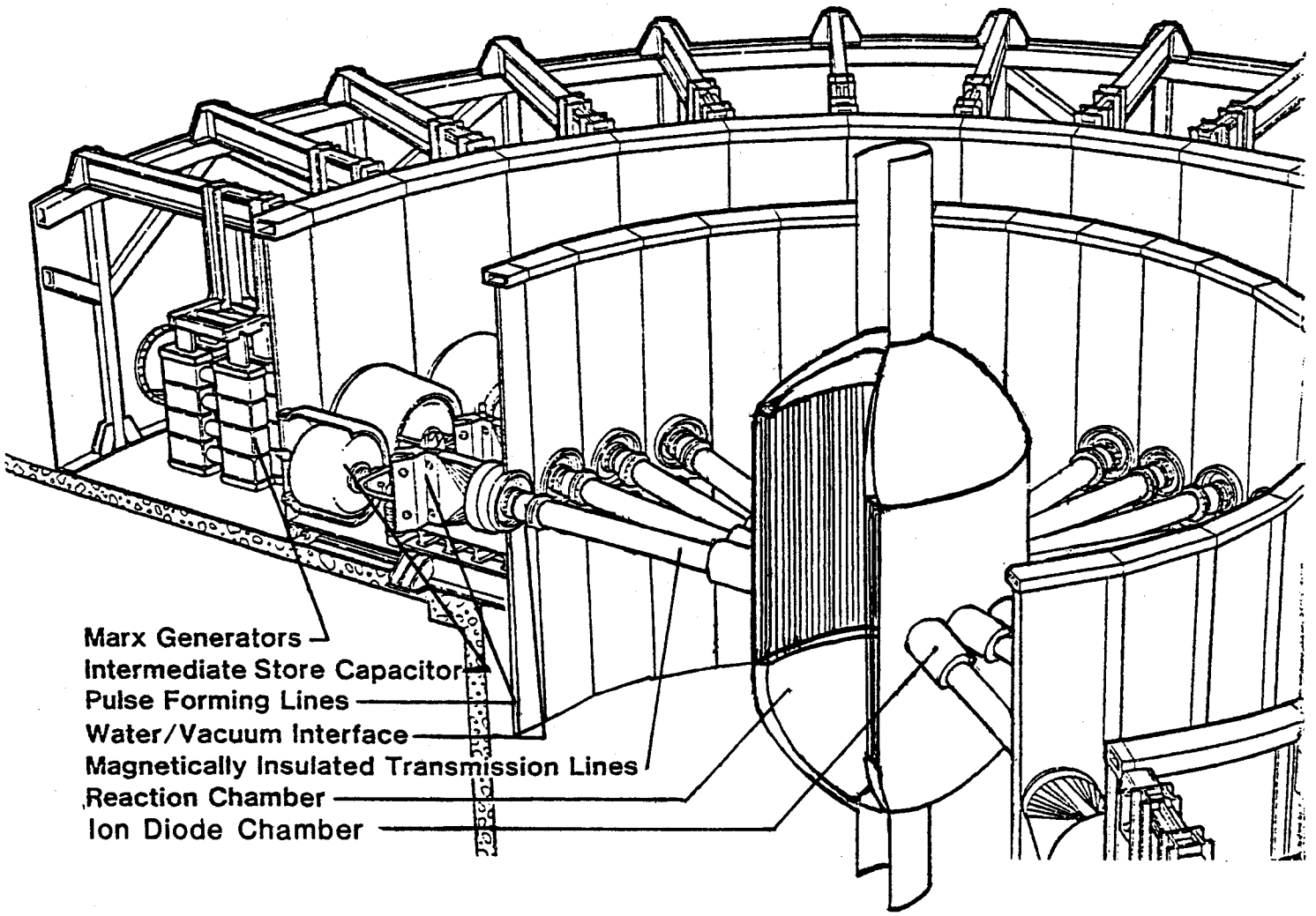
Marx Generators
Intermediate Store Capacitor
Pulse Forming Lines
Water/Vacuum Interface
Magnetically Insulated Transmission Lines
Reaction Chamber
Ion Diode Chamber

6. SUMMARY AND CONCLUSIONS

Progress on the LIBRA design for this year has come in two general areas: cavity response physics and analysis and ion propagation physics and analysis.

(1) A small experimental effort in testing SiC fibers has led to fruitful results. In combination with analytic studies of INPORT unit response to blast waves, we believe that we have confirmed the validity of using INPORT units in the LIBRA design.

(2) Heat transfer calculations for hot gas passing through the array of INPORT tubes have confirmed that the tubes cool the gas sufficiently to allow a 1.5 Hz repetition rate. This was at the upper range of repetition rates originally specified for LIBRA. We cannot rule out the possibility that the repetition rate could be even higher.

(3) Steady progress has been made on the development of a one-dimensional MHD code to model channel formation dynamics.

(4) The state of the art beam plasma instability analysis has been implemented in a small computer code, WINDOW, to predict the regions of beam stability. This code can be used to guide the choice of beam parameters for LIBRA.

(5) A continuing effort to advance the understanding of beam plasma instabilities has made steady progress.

(6) A design for a rep rateable diode has been proposed and awaits additional analysis.